UNIVERSIDAD DE CHILE
FACULTAD DE CIENCIAS FÍSICAS Y MATEMÁTICAS
ESCUELA DE POSTGRADO

HEMODYNAMIC ANALYSIS BASED ON BIOFLUID MODELS AND MRI VELOCITY MEASUREMENTS

TESIS PARA OPTAR AL GRADO DE
DOCTOR EN CIENCIAS DE LA INGENIERÍA, MENCIÓN FLUIDODINÁMICA
EN COTUTELA CON LA UNIVERSIDAD DE GRONINGEN

DAVID JULIAN NOLTE

PROFESOR GUÍA:
AXEL ESTEBAN OSSES ALVARADO

PROFESOR GUÍA 2:
ROEL WILHELMUS CAROLUS PETRUS VERSTAPPEN

MIEMBROS DE LA COMISIÓN:
MIGUEL ÁNGEL FERNÁNDEZ
VOLKER JOHN
PATRICK RAYMOND ONCK
ÁLVARO ALEJANDRO VALENCIA MUSALEM

SANTIAGO DE CHILE
2019

RESUMEN DE LA MEMORIA PARA OPTAR
AL TÍTULO DE DOCTOR EN CIENCIAS DE LA INGENIERÍA, MENCIÓN FLUIDODINÁMICA
POR: DAVID JULIAN NOLTE
FECHA: 2019
PROF. GUÍA: AXEL ESTEBAN OSSES ALVARADO, ROEL WILHELMUS CAROLUS PETRUS VERSTAPPEN

HEMODYNAMIC ANALYSIS BASED ON BIOFLUID MODELS AND MRI VELOCITY MEASUREMENTS

For the diagnosis, treatment planning and post-surgical monitoring of cardiovascular disease (CVD), hemodynamic markers have proven to be of great utility. However, non-invasive assessment of the hemodynamics of a patient is still a challenge. Phase-contrast magnetic resonance imaging (PC-MRI) can measure the distribution of blood velocity along two-dimensional planes or in three-dimensional volumes and is limited in accuracy mainly by the image resolution and noise. The local variation in the blood pressure cannot be measured non-invasively, but is required in the clinical practice to evaluate CVD. Other hemodynamic quantities, such as the arterial wall stiffness or wall shear stress can also be relevant as diagnostic quantities and for understanding the onset of CVD, but are not observable with imaging techniques.

This thesis approaches the topic of patient-specific hemodynamics on three different paths.

In Chapter 2 of this thesis a method was presented to improve the accuracy of hemodynamic data recovery from partial 2D PC-MRI measurements by means of solving an inverse problem of the Navier–Stokes equations of fluid flow. Vessel geometries extracted from MRI or CT images are affected by errors due to noise, artifacts and limited image resolution. Small errors in the geometry propagate into the recovered data and lead to large errors in the solution when standard no-slip boundary conditions are used on inaccurately positioned walls. The core idea of this work was replacing no-slip boundary conditions at the arterial walls by slip/transpiration conditions with parameters which were estimated from velocity measurements. Numerical results of synthetic test cases showed an important improvement in accuracy of the estimated pressure differences and the reconstructed velocity fields.

In Chapter 3 a comparison study of different direct pressure gradient estimation techniques was presented. These methods compute relative pressure fields directly from 3D PC-MRI data. The new Stokes estimation method (STE) by Švihlová et al. [Švi+16] was applied for the first time to real phantom and patient data. In comparison to the classical Poisson pressure estimation method (PPE), the STE method proved more accurate and more robust to noise and the image segmentation in most cases.

Chapter 4 was dedicated to a numerical validation of the new MAPDD model [Ber+19] for a domain decomposition reduction of vascular networks. This approach considers the vessels as a network of thin pipes in which the flow has the shape of a Womersley flow, connected by arbitrary 3D junction domains where the flow is governed by the Navier–Stokes equations. In the MAPDD model, the thin pipes are replaced by coupling conditions on the junction domains. A strategy to easily implement the MAPDD model with the finite element method was presented and the theoretical results of Bertoglio et al. [Ber+19] were reproduced with numerical simulations in a simple test case. The method was shown to deliver accurate results even for moderately large Reynolds numbers, far from the regime where the theory is valid.

RESUMEN DE LA MEMORIA PARA OPTAR
AL TÍTULO DE DOCTOR EN CIENCIAS DE LA INGENIERÍA, MENCIÓN FLUIDODINÁMICA
POR: DAVID JULIAN NOLTE
FECHA: 2019
PROF. GUÍA: AXEL ESTEBAN OSSES ALVARADO, ROEL WILHELMUS CAROLUS PETRUS VERSTAPPEN

ANÁLISIS HEMODINÁMICO BASADO EN MODELOS DE BIOFLUIDOS Y MEDIDAS MRI DE VELOCIDAD

Los indicadores hemodinámicos han demostrado gran utilidad para el diagnóstico, planificación y monitoreo post-operatorio de enfermedades cardiovasculares (CVD). Sin embargo, la evaluación hemodinámica en pacientes continúa siendo un desafío. La Resonancia Magnética de Contraste de Fase (PC-MRI) es capaz de medir la distribución de la velocidad sanguínea en planos 2D o volúmenes 3D, siendo mayormente limitada por la resolución de la imágen y el ruido. Por otro lado, las variaciónes locales en la presión sanguínea sólo pueden ser medidas invasivamente, siendo usualmente requeridas en clínica para la evaluación de las CVD. Otras cantidades hemodinámicas, tales como la rigidez arterial, pueden ser también relevantes para el diagnóstico y entendimiento del origen de las CVD, pero lamentablemente estas no son observables en las imágenes.
Esta tesis aborda el tema de la hemodinámica en pacientes desde tres diferentes perspectivas.

En el Capítulo 2, se presenta un método para mejorar la precisión en la reconstrucción de datos hemodinámicos, usando medidas 2D en PC-MRI. A partir de las ecuaciones de Navier-Stokes para un fluido, se plantea y resuelve un problema inverso. Además, las geometrías arteriales extraídas de imágenes MRI o CT, suelen ser afectadas por errores debidos al ruido, artefactos o propios de la limitación en la resolución espacial. Pequeños errores en la geometría son propagados en la reconstrucción, pudiendo generar mayores desviaciones en la solución, por ejemplo cuando condiciones de borde tipo no-slip son usadas en paredes mal mente posicionadas. La idea central de este trabajo es relajar las condiciones no-slip en las paredes por unas slip/transpiration, con parámetros a estimar de medidas de velocidad. Los resultados numéricos en casos sintéticos muestran mejoras en el cálculo de diferencias de presión y campo de velocidades.

En el Capítulo 3 se presenta una comparación entre diferentes técnicas de estimación de presión. Estos métodos reconstruyen campos de presión directamente de medidas 3D en PC-MRI. Por primera vez el reciente estimador de Stokes (STE) Švihlová y col. [Švi+16] es aplicado en medidas a fantomas y pacientes. A diferencia del clásico estimador de Poisson (PPE), este estimador muestra, en la mayoría de los casos, menos error en la reconstrucción y ser más robusto al ruido y a la segmentación.

El Capítulo 4 es dedicado a la validación numérica del nuevo modelo MAPDD Bertoglio y col. [Ber+19], para una descomposición reducida de redes vasculares. Este enfoque considera las venas como una red de delgadas tuberías, en donde el flujo tiene la forma de un flujo de Womersley, conectado por un dominio arbitrario 3D de uniones, en donde el flujo es gobernado por las ecuaciones de Navier-Stokes. En este modelo, las tuberías delgadas son reemplazadas acoplando distintas condiciones en el dominio de uniones. Aquí, se presenta una estrategia fácilmente de implementar usando elementos finitos. Se reproducen los resultados teóricos de Bertoglio y col. [Ber+19] además de simulaciones numéricas en un caso de prueba simple. El método muestra entregar buenos resultados incluso para números de Reynolds ligeramente grandes, excediendo los límites donde es válida la teória.

Acknowledgements

First and foremost, I would like to thank Cristóbal Bertoglio, who was my daily supervisor during the last four years. *Daily* can be taken literally: always available for discussions, always keen to help, a good idea or an encouraging word when one was needed. He went out of his way to support me in every possible way. I feel thankful for having walked this path together and for everything I learned on the way. Having been able to contribute to the beginnings of his research group was a privilege.

I am grateful to my supervisors, Axel Osses at the University of Chile and Roel Verstappen at the University of Groningen, for their help, for making everything possible, and for supporting our double degree program. Thanks to the members of the assessment committee, Miguel Fernández, Volker John, Patrick Onck and Álvaro Valencia for their thorough reading of my thesis. Furthermore, I am grateful to Volker John for inviting me to his group at WIAS Berlin and for the good and fruitful time I had there.

Without Carlos Conca at the University of Chile I would probably not have attempted a PhD in Chile. It was to him whom I owe my place in his fine institution and financing for my work. Thanks for all the support throughout the years and the faith he put in me.

Thanks to the Chilean institution CONICYT for the excellent financial support through their PhD fellowship.

This thesis would not have been possible without the support of the staff at both universities, in particular those who made possible the double degree agreement. Thanks to Lorena Fuentes, Richard Weber, Christian Ihle, Paula Castillo at the University of Chile and Elina Sietsema, Ika Neven, Annette Korringa at the University of Groningen.

My fellow PhD students and colleagues, especially Richard in Santiago and Sven, Erik, Ronald, Jeremias, Jigar, Larissa, Paolo and Fred in Groningen made this time so much more enjoyable. Thank you for your company, discussions on philosophy, politics, music or literature, for the countless hours spent drinking coffee together.

I feel immensely grateful to my great friends in Santiago, Berlin and Groningen, for making life as beautiful as it is, for being my equilibrium, for all the fun and the sincereness and the adventures.

Finally, thanks to my parents, Ulrike and Rainer, and to my sister, Saskia. With their unconditional support and love, patience and wisdom, they provide the foundation that my life—and this work—is built upon.

Contents

Chapter 1

Introduction

1.1 Clinical motivation

Cardiovascular disease (CVD) is the major cause of death globally [WHO18]. Alone in Europe, CVD causes 3.9 million deaths pear year, accounting for 45 % of deaths from all causes. The estimated overall cost of CVD for the economy of the European Union is €210 billion [Wil+17].

CVD comprises many different diseases, the most common being coronary heart disease. The risk factors of CVD are numerous, including diet, lifestyle and genetics, and are in many cases avoidable [MMG08]. A subset of CVD is congenital heart disease (CHD), i.e., anomalies of the heart or the great vessels in close proximity to the heart present at birth, the cause of approximately 303 300 deaths per year globally [GBD16].

One example of CHD is coarctation of the aorta (CoA), a complex disease of the vasculature in which a stenosis or long narrowed segment in the aorta, typically located at the *ductus arteriosus* insertion, obstructs the blood flow and imposes significant afterload on the left heart ventricle [Bau+10]. CoA accounts for 5 % to 8 % of all CHD, with a prevalence of 3 in 10 000 live births [Erb+14]. If untreated, 80 % of patients CoA die from complications associated with the disease [Hir+10].

CVDs generally affect and alter the blood circulation and the hemodynamic flow patterns in the heart or blood vessels. This can occur for instance by redirection or obstruction of the blood flow due to malformations of the heart, vessels or heart valves, or by alteration of the tissue properties (e.g., stiffness, lesions) or due to plaques. For instance, valvular stenosis and narrowing of vessels due to CoA or atherosclerosis can cause oscillatory flow disturbances and turbulence [Ku97], lead to a drop in hemodynamic pressure and thus an increased cardiac load. Disturbances in the flow patterns on the other hand can cause or contribute to the progression of CVDs [RE06; NOV11; Ku97]. Naturally, hemodynamic characteristics can act as markers for the diagnosis of a CVD, for evaluating the severity of the condition for therapeutic decision-making and treatment planning and for monitoring.

In the context of CoA, valvular stenosis or myocardial infarction, the drop in blood pressure, related to the resistance the pathology exerts on the flow and thus an increased work load for the left ventricle and/or insufficient blood transport to the organs, is already routinely used as a diagnostic indicator [Bau+09; Bau+10; JW99; Cio+11; Kil11].

The local distribution of the blood pressure can be measured by means of catheterization [Bau+10]. This technique consists in inserting a catheter equipped with a pressure transducer into the vasculature of the patient and maneuvering it, under local anesthesia and guided by fluoroscopy, to

the location of interest. Although it is the 'gold standard' for pressure quantification, the invasive nature of the method is associated with a risk of complications [Wym+88; Vit+98; Omr+03].

Considerable effort has been put into research on the non-invasive recovery of information on the hemodynamic pressure. The fundamental relationship between the pressure of a fluid and the flow velocity, described by the Navier-Stokes equations (see Section 1.3), permits estimating pressure data from velocity measurements.

Clinical blood flow measurement techniques, however, are limited. To this day, the clinically relevant measurement techniques to assess hemodynamic flow velocities are Doppler echocardiography and phase-contrast magnetic resonance imaging (PC-MRI).

Doppler echocardiography (see Nichols et al. [NOV11, chap. 8] for technical details) is capable of real-time local velocity measurements along a beam or in two-dimensional (2D) planes. It is versatile, non-invasive, free of ionising radiation and can detect relatively small structures, such as leaflets and narrow jets [Kil11]. The main limitation is the restricted access due to limited penetration depth and view angles [Kil11]. In addition, Doppler echocardiography is very user dependent [Bau+10] and measures only velocities aligned with the beam direction.

PC-MRI (see Taylor and Draney [TD04] for a compact and Brown et al. [Bro+14] for an exhaustive introduction) can measure arbitrary velocity components in freely orientable 2D planes or full volumetric flow fields in 3D volumes (also called 4D-Flow) [Mar+12] with no limits to the field of view. The technique is non-invasive and free of ionising radiation and (usually) contrast agents. It is very versatile and can be applied to a vast range of conditions [Kil11]. However, PC-MRI is mainly limited by the image resolution and slice thickness (for 2D PC-MRI), in the clinical practice usually of the order of 2 mm to 3 mm voxel edge length and 2 mm to 10 mm, respectively. The acquisition time of 3D PC-MRI is another severe limitation and has been one of the factors preventing the widespread clinical use of 3D PC-MRI until today. 2D PC-MRI however is a standard and widely available technique, often preferred to Doppler echocardiography as a means of obtaining accurate flow information [HOR08].

The most widespread technique to recover information on the pressure from Doppler echocardiography velocities is the empirical Simplified Bernoulli (SB) formula for CoA and stenosis, a simplification of the Bernoulli equation. SB relates the maximum velocity measured in a narrowing to a pressure difference over the obstruction. However, the formula does not take into account spatial or temporal patterns in the flow field, nor the geometry of the vessel or shape of the obstruction. As a consequence, the SB formula is known to overestimate the pressure drop [Bau+99; Gar+03; Don+17]. Erbel et al. [Erb+14] consider SB with Doppler velocities unsuitable for pressure drop evaluations.

The abundance of flow information contained in PC-MRI data enables different methods for pressure reconstruction which do not suffer from the limitations of the SB approach. If 3D flow measurements in a complete volume segment are available, the pressure gradient distribution in the domain can be computed 'directly' from the velocity images. In this thesis, this approach is called direct pressure estimation. Section 1.4 gives an overview of the methodology. Partial velocity measurements, for instance 2D PC-MRI or Doppler echocardiography, do not cover the complete domain of interest. However, a reconstruction of the volumetric flow field in the blood vessel—including the blood velocity and the relative pressure—can be obtained by means of solving an inverse problem involving the Navier-Stokes equations. The state of the art of this strategy is discussed in Section 1.5.

1.2 Research questions

The topics examined in this thesis are:

1. Analysis the impact of geometric errors on the inverse recovery of the hemodynamic pressure drop and velocity from 2D PC-MRI measurements and development of a model to compensate such errors (Chapter 2).
2. Analysis and validation of new direct pressure gradient estimation techniques, with real in vivo and in vitro 4D flow measurements (Chapter 3).
3. Development and efficient implementation of a reduced order multi-scale model for vascular trees (Chapter 4).

In the remainder of this introduction, the fundamentals of blood flow modelling are discussed, followed by a review of methods of direct pressure estimation and inverse problems in hemodynamics.

1.3 Blood flow modelling

Blood is a suspension of formed elements (i.e., red and white blood cells, platelets) in plasma [BM03]. In hemodynamics—the macroscopic description of the dynamics of blood flow through the vessels—, blood is considered a continuous single-phase fluid (under the continuum hypothesis, cf. Baskurt [Bas07]). Blood acts as a non-Newtonian fluid with viscoelastic behavior, originating from the deformability of the red blood cells. Its apparent viscosity depends on the viscosity of the plasma (a Newtonian fluid), the hematocrit (volume fraction of blood cells in the blood), red blood cell mechanical properties and red blood cell aggregation [BM03].

Under the continuum hypothesis, blood flow assumed to be governed by the incompressible Navier-Stokes equations,

$$\begin{aligned} \rho\frac{\partial \boldsymbol{u}}{\partial t} + \rho(\boldsymbol{u}\cdot\nabla)\boldsymbol{u} + \nabla p - \nabla\cdot\boldsymbol{\tau} &= \boldsymbol{0} \\ \nabla\cdot\boldsymbol{u} &= \boldsymbol{0} \end{aligned} \tag{1.1}$$

with the velocity vector $\boldsymbol{u} : \Omega \times T \mapsto \mathbb{R}^3$, the pressure $p : \Omega \times T \mapsto \mathbb{R}$, in a spatial domain Ω and a time interval T, and neglecting the gravitational force. $\boldsymbol{\tau}$ denotes the viscous stress tensor and is determined by a constitutive equation modeling the shear behavior of blood. Classical models accurately describing the non-Newtonian rheology of blood are the Casson and the Carreau-Yasuda models [Bir87; GvdVJ99]. At high shear rates and moderate to high Reynolds numbers blood behaves approximately as a Newtonian fluid [CK91; Joh+04]. It is often assumed that such conditions exist in the flow through large vessels, on the basis of which blood can be modelled as a Newtonian fluid [TT16]. Under the assumption of a Newtonian fluid, the viscous stress tensor becomes

$$\boldsymbol{\tau} = \mu\left(\nabla\boldsymbol{u} + (\nabla\boldsymbol{u})^\top\right)$$

with the constant dynamic viscosity, μ. When this assumption is acceptable is a question of ongoing debate and it has been shown to be inaccurate in some situations [GvdVJ99].

The arterial system takes an active part in continuously delivering blood at high pressure to the peripheral vasculature [NOV11, p. 77]. In particular, the large arteries deform elastically un-

der increasing blood pressure during systole and act as a reservoir ("Windkessel") storing blood which is ejected during diastole. Also the long muscular arteries and arterioles actively control the blood propagation to tissue and organs by different mechanisms (see Nichols et al. [NOV11, p. 77]). Hence, for an accurate description of the arterial hemodynamics, it is important to take into account the mechanical properties of the arterial wall tissue. The tissue composition is complex, and in addition to intricate mechanical behavior, involves complex biochemical processes and perfusion. These phenomena, however, are usually neglected in large-scale hemodynamic analyses. In a purely mechanistic setting, the elastic deformation, as a response to forces exerted by the blood flow on the vessel wall, can be accounted for by coupling the Navier-Stokes equations (1.1) with the partial differential equations (PDE) of elasticity with corresponding constitutive laws for the wall deformability. The reader is referred to Sugihara-Seki and Yamada [SY16] for an introduction on the solid mechanics of the arterial wall tissue.

In the practice of computational hemodynamics, computational cost restricts the analysis to small portions of the cardiovascular system, for instance, the section of the vessel containing a stenosis. At the proximal boundary, the inflow velocity profile is usually specified as a boundary condition. At the distal boundary or boundaries, the feedback of the truncated part of the vasculature can be accounted for by means of lumped network models, see, e.g., Formaggia et al. [FQV09b] for a review of models. Reduced order modelling of the vasculature and vascular trees is a topic of intensive research [PV09]. In Chapter 4 of this thesis, a new multi-scale domain decomposition approach is presented as a contribution to the field.

1.4 Direct pressure gradient estimation

PC-MRI is capable of time-resolved measurements of the 3D velocity field in a 3D volume (called '4D-Flow'), containing the vessel of interest. The vessel walls and regions of blood flow are identified by segmentation of the velocity images or from additional anatomic images in order to create a 3D domain of the studied vessel. The domain is usually assumed stationary, i.e., averaged over time, and the time series of measurements associated to the stationary domain. The temporal and spatial resolution of the measurement data allows computing approximately partial derivatives of the data with respect to space and time. By inserting the measured velocities directly into the Navier-Stokes equations (1.1), an approximation of the pressure gradient can be computed directly by evaluating the velocity terms with a suitable numerical method.

Early attempts to reconstruct the relative pressure were presented, for instance, in Urchuk and Plewes [UP94]. The authors invoked the assumption of a Womersley flow and computed the pressure gradient in flow direction from one 2D PC-MR image. Song et al. [Son+94] presented the first 3D approach using the complete Navier-Stokes equations. They recovered velocity data from the pixel intensity displacement of 3D ultra fast CT images and computed the pressure via a Poisson equation, derived by taking the divergence of the Navier-Stokes momentum balance.

This methodology was applied by Yang et al. [Yan+96] to 2D PC-MRI data, who proposed an iterative method for the pressure computation. Tyszka et al. [Tys+00] introduced some improvements to the methodology of Yang et al. [Yan+96] and presented the first relative pressure recovery algorithm applied to true 4D-Flow, which was further improved by, e.g., Ebbers et al. [Ebb+02] and Krittian et al. [Kri+12].

Since then, the only studies comparing *in vivo* in CoA patients the relative pressures computed with PPE-based methods with catheterization data were presented by Riesenkampff et al. [Rie+14] and recently, Goubergrits et al. [Gou+19]. In the former study, comparing peak systolic

PPE pressure differences with catheterization in 13 patients with moderate AoCo, a slight systematic underestimation was found in average of 1.5 mmHg with a large variability of ±4.6 mmHg (two standard deviations). The latter study found the PPE method to be sensitive to the image resolution and introduced a minimum requirement for the resolution based on their data (5 voxels/diameter). Furthermore, the PPE method was shown to be sensitive to the lumen segmentation. By eliminating the outermost layer of voxels, the authors achieved a significantly improved match of the PPE estimates with catheterization data. Possible causes are poor boundary data due to partial volume effects and high noise levels, and the artificial pressure Neumann boundary condition required by the method.

Rengier et al. [Ren+15] validated the PPE method *in vitro* using a phantom consisting of a straight elastic tube with a pulsating flow control and found a good correlation with catheterization data ($r = 0.89$, $p < 0.001$). Other studies validated the PPE using simple phantoms for which the solution is analytically known, e.g., given by a Womersley flow [Ren+14]. These simplified scenarios are a 'special case' with weak or negligible convective effects and a lack of complex 3D flow patterns which are characteristic for aortic flow, especially under stenosis, and seem to represent the main challenge for the PPE method in practice.

Several computational fluid dynamics (CFD) studies of the PPE estimator were conducted [Mei+10; Cas+16; Nas+04] for more complex situations, highlighting the shortcomings of the PPE method. The accuracy of the pressure recovery was shown to be sensitive to many factors [Nas+04; Cas+16], such as the image resolution and segmentation, the velocity encoding and turbulence.

Methodological drawbacks of the PPE are the introduction of artificial pressure boundary conditions on the vessel walls and strong regularity requirements for the pressure and the velocity. These restrictions are avoided in an alternative approach, applying a Helmholtz decomposition, rather than the divergence, to the Navier-Stokes equations. This approach leads to a Stokes problem for an auxiliary, non-physical velocity function and the hemodynamic pressure. The methodology was first presented in Cayco and Nicolaides [CN86] in a different context and adapted to relative pressure reconstruction from PC-MRI velocity data by Švihlová et al. [Švi+16]. This technique, the Stokes estimator (STE), was shown in numerical studies to deliver more accurate results than the PPE method [Švi+16; Ber+18b]. In Chapter 3 of this thesis the first comparative study of the STE and the PPE methods using real PC-MRI phantom and patient data is presented in the context of CoA.

Other approaches have been proposed for the computation of averaged pressure differences between two cross-sections of a blood vessel, namely the work-energy relative pressure (WERP) method [Don+15], and its extensions, the virtual WERP (vWERP) method [Mar+19] and the integral momentum relative pressure (IMRP) estimator [Ber+18b]. A simplification of the WERP method was presented in Donati et al. [Don+17] as a generalization of the Bernoulli approach, which allows to compute the pressure drop from 2D PC-MRI data. These methods are faster to compute than the PPE or the STE, but instead of 3D and time-resolved pressure maps, yield only averaged pressure differences between cross-sections. They are therefore suited to assess the pressure drop, e.g., over a valvular stenosis or CoA, and can be viewed as an alternative for the Doppler echocardiography–simplified Bernoulli approach. The fact that the pressure difference is averaged over the entire cross-section renders the comparison with catheter measurements difficult. The WERP method requires the vessel section of interest not to include any bifurcations (such as the supra-aortic branches), which is avoided by the vWERP and IMRP methods.

All of the methods depend on the description of the blood flow as the incompressible flow of a Newtonian fluid. The spatial and temporal resolutions at which the underlying Navier-Stokes equations are evaluated are dictated by the PC-MRI data, i.e., of the order of several millimeters

and around 40 ms. As a consequence, these methods do not include the effects of turbulence or non-Newtonian properties of the blood. Furthermore, they do not account for the elastic deformations of the vessel walls. In addition to the model dependency, direct pressure estimation methods are strongly affected by data perturbation, such as noise, image artifacts, the resolution of the data. Noise is an important issue in PC-MRI, where white noise levels of 15 % of the expected maximum velocity are common [Dyv+15], leading to low signal-to-noise ratios (SNR) outside of the peak systole and generally in regions with low flow velocities.

Other approaches estimate the turbulent kinetic energy (TKE) of the flow from the PC-MRI signals [Dyv+06] and propose pressure loss estimators based on the dissipation of the TKE [Dyv+13; Ha+19] as an alternative to the Bernoulli-based formulas. *In vitro* and *in vitro* studies have shown promising results for cases of aortic stenosis [Ha+16b; Ha+19]. The methodology is only applicable to turbulent flow. I.e., pressure drop estimation based on the TKE can be useful for valvular stenosis, where turbulence can be expected, but not for low Reynolds number flows in general, at mild conditions or during diastole.

A drawback of the discussed direct pressure reconstruction methods is the requirement of 3D PC-MRI data[1]. To this day, long acquisition times have prevented the translation of 3D PC-MRI to the clinical practice and 3D PC-MRI sequences are rarely available. In addition, in direct methods derived from the Navier-Stokes equations, e.g., Bernoulli-based, PPE, STE, at any instant of time the pressure is uniquely defined up to a constant (with respect to the spatial coordinates). Therefore, only instantaneous pressure differences between different locations can be compared at different times. Catheterization or sphygmanometer pressure measurements are taken relative to the atmospheric pressure. Hence, the pressures are calibrated with respect to a global reference and pressure values can be compared at different times. A common measure in the clinical practice are the so-called *peak-to-peak* pressure differences, which compare the difference in the pressure maxima registered at different locations during the complete cardiac cycle, thus taking into account time shifts due to the vessel elasticity. Peak-to-peak pressure differences can only be determined by means of catheterization or with the models described above when calibrated with catheterization data, which however invalidates the non-invasiveness of the estimation methods.

1.5 Patient-specific hemodynamics

Increase in computer performance, the advent of PC-MRI and ever improving image quality gave rise to the relatively new research topic of patient-specific hemodynamic simulation of large arteries, based on medical images [TS10].

Patient-specific modelling requires the topology of the patient's vessel under investigation to be reconstructed by segmentation of medical images, e.g., CT or MRI, and a numerical blood flow model to be set up within this domain. The proper inflow and outflow boundary conditions, the initial condition (often neglected) and possibly unknown model parameters have to be calibrated from measurements, for instance, 2D PC-MR images. The determination of the boundary conditions is arguably the most important issue and has received a lot of attention in the literature, which shall be reviewed below. Two different approaches can be distinguished: pre-computation of boundary data directly from PC-MRI data or estimating the required data from the measurements by means of solving an inverse problem. Both approaches are discussed in the subsequent sections.

[1] Exceptions are the Bernoulli formula, the simplified advective WERP estimator [Don+17] and early methods which are clinically irrelevant due to their oversimplifications, such as Urchuk and Plewes [UP94].

Solving the model equations, a reconstruction of the hemodynamics (e.g., velocity and pressure fields) with great detail can be obtained from a geometric reconstruction of the vessel and sparse, partial velocity measurements. Since the pressure is (usually) an internal variable of the fluid flow model, pressure drops are readily obtained.

Importantly, a complete hemodynamic characterization can be estimated from partial, 2D PC-MRI measurements. This is a big advantage over direct pressure estimation methods, which with few exceptions[2] require 3D PC-MRI data. Hence, relative pressure estimation using hemodynamic simulation calibrated with 2D PC-MRI allows to significantly reduce the MRI scan time. This comes at the cost of increased computation times required for the solution of the inverse problem (an optimization problem constrained by the Navier-Stokes equations), compared to direct pressure estimation, where, e.g., only Poisson or Stokes problems have to be solved.

1.5.1 Forward hemodynamic simulations

Inflow and outflow boundary conditions for a CFD model are often determined beforehand from 2D PC-MRI data recorded on slices along the boundaries. A common approach is calculating the mass flow rate by integrating the velocity over the measurement slice at a boundary (i.e., the component in normal direction to the boundary). By temporal interpolation between the images (the time step of the simulation is usually at least one order of magnitude smaller than the temporal resolution of the measurements), the inflow waveform can be obtained. The mass flow rate is a so-called defective boundary condition [For+02], as they do not ensure well-posedness of the flow problem [VV05]. An option is using simplified inflow velocity profiles, such as plug flow, parabolic or Womersley profiles, with time-dependent amplitudes determined by the waveform as Dirichlet boundary conditions [Cam+12].

However, it was demonstrated that helical and retrograde secondary flow patterns are inherent features of the aortic flow, due to the curvature of the aortic arch and the pulsating nature of the flow [Kil+93; Fry+12; Hop+07]. Simplified inflow profiles prevent the development of such features downstream of the boundary and can deteriorate the fidelity of the simulation [TGS17].

In order to account for these complex flow features, some authors used 2D or 3D PC-MRI data directly as Dirichlet boundary conditions by interpolating the velocity measurements onto the computational mesh and simulation time steps. Several studies compared simplified profiles with prescribed mass flow with spatially resolved velocity fields and found that flow patterns in the interior and, for instance the wall shear stress, were sensitive to the inlet boundary condition [Gou+13; Mor+13; Wak+09; Tan+12; Boz+17; Cam+12; Har+13]. However, this approach is limited by the high noise levels and low spatial and temporal resolutions (compared to the numerical discretization) typical for PC-MRI data and possible misalignment of the velocity measurements with the computational domain.

A different approach is enforcing the measured mass flow by means of Lagrange multipliers [For+02; VV05]. This results in an increased computational cost and the need for specialized numerical methods [VV05].

Different strategies exist for personalized outflow boundary conditions. Especially when multiple outflow boundaries are present, the choice of the boundary conditions is not straight forward. Velocity profiles measured with PC-MRI can be prescribed at the outlets, but difficulties arise from possible phase shifts, measurement noise, limited image resolution and the requirement of instantaneous mass conversation [Gal+12]. An alternative present simplified profiles prescribing mass

[2] see footnote 1

flow waveforms with fixed flow rate ratios between the inlets and outlets determined from PC-MRI measurements or according to cross-section areas if no measurements are available. 'Zero stress' homogeneous Neumann conditions can be combined with the former approaches. Windkessel models [For+06; WLW09] and more sophisticated lumped networks [Vig+10; GK08] model the feedback of the truncated vasculature and have been shown to be accurate in complex situations with many outlets [Kim+10; Kun+13; Bar+11; Pir+17; Mor+10]. Usually the model parameters have to be tuned to each specific patient which can be computationally expensive, see Section 1.5.2. A large number of studies uses literature values for the parameters of lumped network models, undermining to some extent the desired 'patient specificness'. Gallo et al. [Gal+12] compare different popular combinations of outlet boundary conditions for an aortic flow and, while not considering lumped networks, conclude that for accurate results, flow rate boundary conditions based on velocity measurements should be preferred over not fully personalized boundary conditions. Pirola et al. [Pir+17] carried out a similar study of a real aorta, also taking into account three-element Windkessel boundary conditions with empirical parameters. A comparison with different combinations of PC-MRI based mass flow and zero-stress boundary conditions revealed that Windkessel boundary conditions at all outlets were necessary to compute realistic velocity and pressure fields.

The computational domain is reconstructed from anatomical MRI or CT images. However, the segmentation process used to determine the vessel contours is subject to errors caused by the limited image resolution, flow artifacts and partial volume effects [Moo+99]. The impact of errors in the vessel geometry has received relatively little attention. A first recognition of the effect of geometry errors on PC-MRI based flow simulations, in particular regarding the wall shear stress, was presented by Moore et al. [Moo+99] and Moore et al. [MSE97]. Causes of geometric errors and their effects on the arterial blood flow were further investigated in Gambaruto et al. [Gam+08; Gam+11]. The authors found that small changes in geometry cause important variations in the solution. Their work was followed by Sankaran and Marsden [SM11], Sankaran et al. [SGT15b], Sankaran et al. [SGT15a], and Sankaran et al. [San+16], studying geometric uncertainties and other sources of errors in CT-based hemodynamic simulations by means of uncertainty quantification. Again, the results were found to be sensitive to geometric uncertainties. Recently, the issue of geometric errors was investigated theoretically and error bounds were presented [MR19]. All studies concluded that geometric uncertainties have a strong impact on the problem solution. In Chapter 2 of this thesis and in Nolte and Bertoglio [NB19], a method is presented to compensate geometric errors within a data assimilation framework (see the next section).

1.5.2 Inverse problems

Patient-specific model and boundary data required for patient-specific simulations can be estimated from measurements by solving an *inverse problem*. In the present context, the inverse problem takes the form of a PDE-constrained optimization problem.

In contrast to pre-computing the unknown parameters from measurements, for instance by fitting predefined velocity profiles, the optimization approach tunes the parameters such that the discrepancy between the measurements and the model solution is minimized. The parameter adjustment is non-local in the sense that they are calibrated with respect to all available measurements. In general, the measurements are not required to be located at the corresponding boundaries. The inverse approach offers much more versatility regarding the measurement data, the fluid model and estimatable parameters at the expense of higher computational cost.

Formulation and solution methods

The PDE-constrained optimization problems considered here consist of

- a hemodynamic model (the PDE constraint),
- measurements of the model state,
- an observation operator mapping the model state to the observation space,
- an objective function to be minimized, i.e., a measure of the discrepancy between the model predictions and the measurements, weighted by the respective uncertainties.

The task is to estimate uncertain model parameters or the initial condition of the model state by minimizing the objective function.

The model is a system of PDEs that describes the blood flow dynamics as discussed in Section 1.3. In contrast to the direct methods presented in the previous section, this methodology is not limited to the assumption of incompressible flow within a rigid domain. Let us introduce the following short-hand notation for the semi-discrete numerical model, representing a differential algebraic equation (DAE),

$$\dot{X} = \mathscr{A}(X, \theta), \tag{1.2}$$

where $\mathscr{A} : \mathbb{R}^n \times \mathbb{R}^p \mapsto \mathbb{R}^n$ is the model operator and $X(t) \in \mathbb{R}^n$ denotes the model state with n degrees of freedom and an initial condition $X(0)$. Physical model parameters are summarized in the parameter vector $\theta \in \mathbb{R}^p$.

Measurements, $Z(t) \in \mathbb{R}^m$, are related to the state via the observation operator, $\mathscr{H} : \mathbb{R}^n \mapsto \mathbb{R}^m$, such that

$$Z(t) = \mathscr{H}(X) + \zeta, \tag{1.3}$$

where $\zeta \in \mathbb{R}^m$ represents measurement errors, such as noise. This relationship allows *partial* measurements, or measurements of derived quantities of the state, to be used to estimate the state and/or model parameters.

Assuming the initial state X_0 and the parameters θ are sought, a functional can be defined of the form

$$J(X(0), \theta) = \int_{t_0}^{T} \|Z - \mathscr{H}(X)\|^2_{W^{-1}} \, \mathrm{d}t + \|X(0) - X_0\|^2_{C_0^{-1}} + \|\theta - \theta_0\|^2_{P_0^{-1}}, \tag{1.4}$$

with X satisfying the model DAE (1.2). X_0 and θ_0 denote *a priori* expected values for the initial condition and the parameters with their respective uncertainty covariance matrices, C_0 and P_0. W is the covariance matrix related to the measurement errors.

By minimizing J with respect to $X(0)$ and θ, an optimal trajectory of $X(t)$ can be found (for instance, velocity and pressure fields), balancing the uncertainty of the measurements with the uncertainty of the model predictions. The last two terms in Eq. (1.4) act as regularization terms. Equations (1.2)–(1.4) constitute the typical problem setting of data assimilation (DA), see, e.g., Talagrand [Tal97] and Kalnay [Kal03], and originate from the formulation of a maximum likelihood estimation problem assuming that the measurement noise and the *a priori* parameters have a Normal distribution.

Two classes of methods exist for solving the DA problem described by Eqs. (1.2)–(1.4). *Variational DA*, based on the adjoint of the problem, adjust the complete trajectory of the state $X(t)$, the unknown initial condition $X(0)$ and the unknown parameters θ to the observations given at all times (i.e., 'past' and 'future' observations). This typically requires computation of the adjoint,

repeated forward and backward solves of the problem in an optimization loop and storing the complete time history of the state. The complexity, i.e., number of iterations, is independent on the number of parameters. Applying adjoint-based methods to joint state–parameter estimation in realistic problems (i.e., 3D, time-dependent, nonlinear) is challenging due to the large requirements in computational power, but routinely done in numerical weather prediction [Kal03] using large computing clusters.

Sequential DA assimilates observations into the model state, once they are 'encountered', directly during the time integration of the forward problem. Sequential methods are recursive and optimize state and parameters at a point in time with respect to all past observations, but do not consider future observations. In advantages with respect to variational DA are that storage of the state is not required and that gradients of the functional J and adjoints are avoided ('derivative-free' optimization). On the other hand, the complexity increases with the number of parameters. Sequential DA methods are often extensions of the linear Kalman filter, such as the Ensemble Kalman Filter [Eve09] (EnKF) or the Unscented Kalman Filter [JU97] (UKF). The main challenge of the Kalman filtering approaches is that the covariance matrix of the uncertainties, a dense square matrix of the size of the dimension of the uncertain parameters and/or initial condition, has to be propagated in time with the model. Instead, an ensemble of states ('particles') can be used to approximate the error covariance matrix. This is achieved in the UKF and the EnKF, using deterministic or stochastic particles, respectively. Sequential DA methods are prohibitive for state estimation in realistic hemodynamic problems if no assumptions are made to severely reduce the problem size. The large number of particles required (for instance, 50 to 100 for the EnKF) results in a high demand in CPU time, since for each particle one independent forward problem has to be solved. These particle forward problems can be solved simultaneously on a parallel computer.

Joint state–parameter estimation in hemodynamics

In hemodynamics, Funke et al. [Fun+19] used variational DA (4D-Var) to reconstruct the flow in a patient-specific aneurysm from PC-MRI data. Using a coarse numerical mesh and large time steps, the computational time was reported to be 50 to 100 times that of the forward problem. Since even the accurate forward solution of the Navier-Stokes equations in the convection-dominated or turbulent flow regime is a challenging task, full-scale variational DA is still out of reach for state estimation in aortic flow simulations.

Both the UKF and the EnKF have been used successfully for low-order hemodynamic models. In Pant et al. [Pan+14], patient-specific hemodynamics in an aorta with CoA were computed with a multi-scale approach, where the parameters of lumped models for the boundary conditions of the full-dimensional fluid problem were estimated in a 0D surrogate model by means of the UKF. DeVault et al. [DeV+08] used the EnKF to determine the boundary conditions of a 1D representation of the blood flow through a vascular network from Doppler echocardiography velocity measurements.

Parameter estimation in hemodynamics

The data assimilation problem can be greatly simplified by neglecting the uncertainty in the initial condition of the state (number of unknowns of the order 10^5 to 10^7) and only considering uncertainties in the parameters (typically dozens or less), describing, i.e., boundary conditions and material properties.

Both variational and sequential DA methods are applicable to the resulting parameter estimation problem. For small numbers of parameters, the sequential approach offers the advantages of computational efficiency (mostly due to the recursivity) and implementational simplicity.

A reduced order version of the UKF for parameter estimation was presented in Moireau and Chapelle [MC11], referred to as the Reduced-Order Unscented Kalman Filter (ROUKF). The number of particles it employs is the number of parameters to be estimated plus one. The ROUKF has been used successfully in hemodynamic applications, namely, parameter identification in fluid–structure interaction problems [Moi+13; BMG12; Ber+14] and in reduced order models of the arterial network [Lom14; Cai+17; MCB18]. It was furthermore employed in Chapter 2 of this thesis and in Nolte and Bertoglio [NB19] for parameter estimation in a CFD study of arterial blood flow, using a geometric errors compensating wall boundary model. Lal et al. [LMN17] used the EnKF for parameter estimation in a cardiovascular network.

Sequential data assimilation is not suitable for estimating complex velocity inflow profiles because of the high number of degrees of freedom to be determined (of the order of hundreds or thousands).

Variational data assimilation was used for the boundary parameter estimation problem in, for instance, Formaggia et al. [FVV08], who extended the treatment of defective boundary conditions presented in Veneziani and Vergara [VV05]. In synthetic 2D and axisymmetric studies of blood flow, assuming a steady state–hence avoiding the issue of uncertain initial conditions—, D'Elia et al. [DPV12] estimated Neumann boundary condition data from artificial velocity measurements using variational data assimilation. The approach was extended in Tiago et al. [TGS17] to the estimation of full 3D inflow velocity profiles from partial velocity data given at slices in different locations. In contrast to the assumption of simplified velocity profiles, helical and secondary flow patterns could be recovered downstream from the inlet. Guerra et al. [Gue+18] presented a further extension to non-Newtonian blood flow. A similar procedure was presented in Koltukluoğlu and Blanco [KB18], also assuming stationary flow, for estimating the velocity inflow profile from 4D-Flow data. The methodology delivered accurate results in an experiment using real data acquired in an aortic phantom.

An adjoint-based parameter estimation method was presented in Ismail et al. [IGW12; IWG13] and applied to real patient-specific aortic flow problems, considering both a CFD setting and coupling the hemodynamics to the elastic vessel wall mechanics. Windkessel parameters were calibrated from flow rate and pressure measurements. The method proved robust and delivered realistic results.

State observers in hemodynamics

A different approach to state estimation consists in using state observers, which add a feedback term with a constant and sparse precomputed gain matrix to the model equations, involving the discrepancy between observations of the state and the measurements (see, e.g., Heys et al. [Hey+10], Funamoto et al. [Fun+08], and Bertoglio et al. [Ber+13]). This methodology is effective for estimating the state in presence of uncertainties in the initial guess but estimating model parameters is not possible.

However, sequential data assimilation methods for parameter estimation can be combined with state observers in order to enable computationally inexpensive joint state/parameter estimation. See, e.g., Moireau et al. [Moi+13] for applications in hemodynamics, where the observer was used in the context of joint estimation of the state and boundary tissue support parameters.

1.6 Thesis overview

This thesis contributes to the areas of patient-specific inverse hemodynamics, direct pressure gradient estimation and multi-scale modeling of vascular networks.

Patient-specific inverse hemodynamics: Geometric uncertainty in image-based vessel reconstructions is known to be an important issue in patient-specific simulations. Chapter 2 assesses in a synthetic test case of coarctation of the aorta the impact of geometry errors on the pressure drop obtained from velocity measurements by means of sequential data assimilation. A boundary model and a numerical method capable of compensating such errors is presented. While the issue of inflow and outflow boundary conditions has received a lot of attention, to the best of the author's knowledge, no previous studies have presented a method to reduce geometric errors in the vessel wall. However, virtually all studies based on the Navier-Stokes equations use computational domains obtained from imaging, unavoidably affected by uncertainty.

Direct pressure gradient estimation: 4D-Flow based pressure gradient estimation techniques have been widely used in proof-of-concept studies for the last two decades, however they are not routinely used in the clinical practice. Only few studies compared pressure drop estimators with catheterization. In Chapter 3, a comparison of the PPE and the STE pressure gradient estimation methods with pressure catheterization measurements is presented for aortic phantoms and CoA patients. To the best of the author's knowledge, this is the first time that the STE method is validated using real data. The impact of image resolution and lumen segmentation—strongly related to the geometric errors discussed in the previous paragraph—is investigated.

Multiscale modeling of vascular networks: The method of asymptotic partial decomposition of a domain (MAPDD), a new multiscale method, describes vascular trees as networks of full-dimensional junctions in which the flow is governed by the Navier-Stokes equations, connected by vessels in which the flow is assumed to be of Womersley type. Chapter 4 discusses a practical implementation of the MAPDD and validates the theory with numerical examples.

Chapter 2

Data assimilation: reducing geometric errors

The content of this chapter was published in D. Nolte and C. Bertoglio. "Reducing the Impact of Geometric Errors in Flow Computations Using Velocity Measurements". In: *International Journal for Numerical Methods in Biomedical Engineering* (2019), e3203. DOI: 10.1002/cnm.3203.

2.1 Introduction

In this chapter, the performance of the PDE-constrained optimization approach from 2D PC-MRI is analyzed in numerical test cases when geometric errors in the reconstructed 3D domain are present. In cardiovascular modeling, geometry errors arise unavoidably from the segmentation of anatomical medical images (i.e., CT or MRI), which are of limited resolution, contain measurement noise, include partial volume effects [MSE97; Moo+99]. Figure 2.1 illustrates this issue with white pixels denoting interior and black pixels exterior regions of a blood vessel. The separation between both is blurred due to the aforementioned imaging limitations (gray pixels). The blue lines mark possible segmentations of the vessel wall.

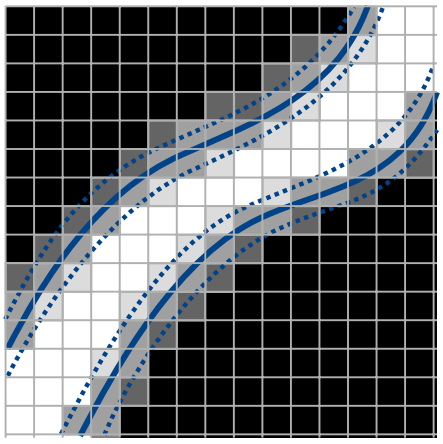

Figure 2.1: Illustration of potential segmentation errors in a medical image.

The problem of geometric errors in blood flow computations has been recognized and studied previously by Moore et al. [MSE97] and Moore et al. [Moo+99]. Uncertainty quantification studies of geometric uncertainty in CT-based hemodynamics simulations were subsequently presented in a series of papers [SGT15a; SM11; SGT15b; San+16]. Recently, theoretical error bounds

were derived for finite element discretizations of PDEs under geometric uncertainties [MR19]. To the authors' best knowledge, other than improvements to the image segmentation process, no methods have been reported to cope for these inaccuracies.

In this work we introduce a flow reconstruction methodology which considers alternative slip/transpiration boundary conditions estimated from velocity data, which are able compensate the geometric errors. The methodology is detailed in section 2.2. In section 2.3 the method is tested in numerical experiments. The results are discussed in section 2.4, followed by conclusions in section 2.5.

2.2 Methodology

2.2.1 Fluid Flow Model

Geometry definitions

Assume that an approximation of the geometry of a blood vessel is obtained by segmenting medical images. We consider both the true geometry and the segmented, approximate version. The true domain of the vessel is denoted by Ω, such that $\partial\Omega = \Gamma_w \cup \Gamma_i \cup \Gamma_o$, with Γ_w representing the true vessel wall. The segmented domain is denoted by $\widetilde{\Omega}$ and bounded by $\partial\widetilde{\Omega} = \widetilde{\Gamma}_w \cup \widetilde{\Gamma}_i \cup \widetilde{\Gamma}_o$. Both the true and the segmented domains of a sample vessel are illustrated in Figure 2.2.

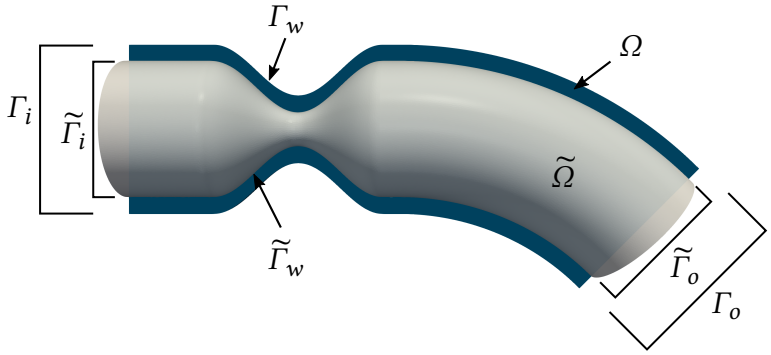

Figure 2.2: 'Approximate' segmented domain $\widetilde{\Omega}$ (gray) and cut plane of true domain Ω (blue). $\Gamma_i, \widetilde{\Gamma}_i$ are proximal to the heart, $\Gamma_o, \widetilde{\Gamma}_o$ distal. $\Gamma_w, \widetilde{\Gamma}_w$ denote the vessel wall.

The incompressible Navier-Stokes equations

Restricting the analysis to large vessels and neglecting elastic effects of the vessel walls, the unsteady Navier-Stokes equations of an incompressible, Newtonian fluid [SY16] are a suitable model

to compute the blood flow inside the vessel Ω (and therefore also valid in $\widetilde{\Omega}$),

$$\rho\frac{\partial \boldsymbol{u}}{\partial t} + \rho(\boldsymbol{u}\cdot\nabla)\boldsymbol{u} + \nabla p - \mu\Delta\boldsymbol{u} = \boldsymbol{0} \quad \text{in } \Omega \tag{2.1a}$$

$$\nabla\cdot\boldsymbol{u} = \boldsymbol{0} \quad \text{in } \Omega \tag{2.1b}$$

$$\boldsymbol{u}(0) = \boldsymbol{u}_0 \quad \text{in } \Omega \tag{2.1c}$$

$$\boldsymbol{u} = \boldsymbol{g}_d(\boldsymbol{x},t) \quad \text{on } \Gamma_i \tag{2.1d}$$

$$\boldsymbol{n}\cdot[\mu\nabla\boldsymbol{u} - \mathbb{1}p] = g_n(\boldsymbol{x},t)\boldsymbol{n} \quad \text{on } \Gamma_o \tag{2.1e}$$

with the velocity vector $\boldsymbol{u} : \Omega \longrightarrow \mathbb{R}^3$, the pressure $p : \Omega \longrightarrow \mathbb{R}$, the density ρ and dynamic viscosity μ. Γ_i denotes inflow boundaries, where the velocity profile $\boldsymbol{g}_d(\boldsymbol{x},t)$ is specified by means of a Dirichlet boundary condition. Boundary patches denoted by Γ_o are those where Neumann boundary conditions are given. As boundary conditions for the vessel walls, Γ_w and $\widetilde{\Gamma}_w$, two models will be used in this work, which are detailed in the following sections.

No-slip boundary conditions

The most used wall boundary condition is the no-slip condition, namely

$$\boldsymbol{u} = \boldsymbol{0} \quad \text{on } \Gamma_w \text{ or } \widetilde{\Gamma}_w.$$

In the remainder of this work, we will assume that this is the correct boundary condition at the true vessel wall Γ_w. We will study the errors which no-slip boundary conditions on $\widetilde{\Gamma}_w$ induce in the results computed in the approximate geometry $\widetilde{\Omega}$.

Slip/transpiration boundary conditions

If the boundaries $\widetilde{\Gamma}_w$ reside inside of the flow region, i.e., $\widetilde{\Omega} \subset \Omega$, it may be more appropriate to allow for some slip along and transpiration (leakage) across the wall. This situation is illustrated in Figure 2.3, where a virtual boundary, $\widetilde{\Gamma}_w$, is immersed in the fluid region Ω.

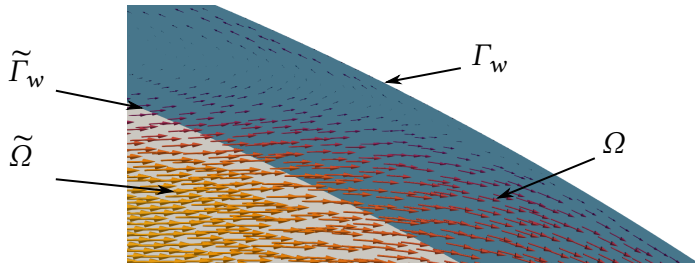

Figure 2.3: Sketch of slip and transpiration at a virtual boundary $\widetilde{\Gamma}_w$ of the domain $\widetilde{\Omega}$, embedded in a 'physical' domain Ω with the physical boundary Γ_w.

Robin-type boundary conditions on such artificial domain boundaries allow for flow in wall-normal and tangential directions, controlled by coefficients, which in the general case may vary in space and time. The coefficients can be defined in such a way that the solution is equal to the corresponding portion of the solution computed on the complete domain with no-slip conditions on the 'true' wall. These boundary conditions, which we refer to as slip/transpiration conditions, can

be written in the following form, separating the contributions in the normal and in the tangential directions:

$$\sum_{k=1}^{d-1} \boldsymbol{n} \cdot [\mu \nabla \boldsymbol{u} - \mathbb{1} p] \cdot \boldsymbol{t}_k + \gamma \boldsymbol{u} \cdot \boldsymbol{t}_k = 0 \quad \text{on } \widetilde{\Gamma}_w \tag{2.2a}$$

$$\boldsymbol{n} \cdot [\mu \nabla \boldsymbol{u} - \mathbb{1} p] \cdot \boldsymbol{n} + \beta \boldsymbol{u} \cdot \boldsymbol{n} = 0 \quad \text{on } \widetilde{\Gamma}_w. \tag{2.2b}$$

Here, $\boldsymbol{n}$ denotes the outward unit normal vector and $\boldsymbol{t}_k$, $k = 1, \dots, d-1$ are orthogonal unit tangent vectors. The number $d \in \{2; 3\}$ denotes the geometric dimension of the problem.

Equation (2.2a) is a *slip-friction* (also called Navier-slip) boundary condition, see, e.g., John and Liakos [JL06]. The coefficient γ controls the ratio the of tangential stress to the tangential velocity. For $\gamma = 0$, this boundary condition is equal to a free slip condition. In the limit $\gamma \longrightarrow \infty$, the no-slip boundary condition (for the tangential velocity component) $\sum_{k=1}^{d} \boldsymbol{u} \cdot \boldsymbol{t}_k = 0$ is recovered. The transpiration boundary condition, Equation (2.2b), allows for flow perpendicular to the wall. Transpiration has been used extensively in the context of fluid–structure interaction, see, e.g., Hall and Crawley [HC89], Mortchéléwicz [Mor00], Fernández and Le Tallec [FL03], and Figueroa et al. [Fig+06]. The amount of transpiration through the wall is controlled by the parameter β. The limit $\beta \longrightarrow \infty$ approaches no-penetration boundary conditions. In the case of $\beta = 0$, the fluid is allowed to freely pass through the wall in normal direction. Both conditions can be set independently, for instance a free-slip condition in the tangential directions and a no-penetration condition for the normal velocity component. In particular, $\gamma = \beta = 0$ characterizes a free outflow condition, whereas $\gamma, \beta \longrightarrow \infty$ asymptotically recovers no-slip boundary conditions. Hence, the combined slip/transpiration boundary conditions are able to represent very different types of boundary conditions, depending only on the coefficients β and γ. A theoretical analysis of slip/transpiration boundary conditions in the context of the finite element method was presented in John [Joh02].

For cases where an analytical solution to the Navier-Stokes equations is known, the parameters can be determined exactly. In Appendix 2.A the slip model is applied to a Poiseuille flow and the slip parameter computed. Note that in the general case, the values of these coefficients are unknown. Estimating β and γ from velocity measurements is the subject of section 2.2.2.

Note that while our physical justification of the slip/transpiration boundary conditions is based on the assumption $\widetilde{\Omega} \subset \Omega$, the model can also be applied to cases where the assumption is violated. However, large improvements in accuracy over no-slip boundary conditions cannot be reasonably expected. Here, we limit our study to cases where the assumption is valid.

Fractional step scheme

For the sake of computational efficiency, in particular since solving the inverse problem requires flow computations for several parameter combinations, we employ a fractional step scheme, splitting the original coupled system (2.1a)–(2.2b) into a sequence of decoupled, easier to solve PDEs. In particular we use a version of the classical Chorin-Temam non-incremental pressure correction scheme [GMS06].

The method is given in linearized, time-semidiscretized form in algorithm 1, for the case where slip/transpiration boundary conditions are applied on the boundary patch $\widetilde{\Gamma}_w$. Note that the algorithm is stated for the segmented domain, $\widetilde{\Omega}$ with $\partial\widetilde{\Omega} = \widetilde{\Gamma}_w \cup \widetilde{\Gamma}_i \cup \widetilde{\Gamma}_o$. For the reference domain, simply replace $\widetilde{\Omega}$ by Ω and the boundaries $\widetilde{\Gamma}_*$ by Γ_*. No-slip boundary conditions can be defined on $\widetilde{\Gamma}_w$ (or Γ_w) by replacing Eqs. (2.5d)-(2.5e) by the condition $\tilde{\boldsymbol{u}}^{k+1} = \boldsymbol{0}$ on $\widetilde{\Gamma}_w$ (or Γ_w).

Algorithm 1 Restarting fractional step algorithm using slip/transpiration boundary conditions.

Given an initial field $\tilde{\boldsymbol{u}}^0$, compute for $k = 0, \dots, N$:

1. Projection step:

$$\nabla^2 p^k = \frac{\rho}{\Delta t} \nabla \cdot \tilde{\boldsymbol{u}}^k \quad \text{in } \widetilde{\Omega} \tag{2.3a}$$

$$\boldsymbol{n} \cdot \nabla p^k = 0 \quad \text{on } \widetilde{\Gamma}_i \tag{2.3b}$$

$$p^k = g_n^k \quad \text{on } \widetilde{\Gamma}_o \tag{2.3c}$$

$$\boldsymbol{n} \cdot \nabla p^k + \frac{\rho}{\Delta t} \beta^{-1} p^k = \frac{\rho}{\Delta t} \tilde{\boldsymbol{u}}^k \cdot \boldsymbol{n} \quad \text{on } \widetilde{\Gamma}_w \tag{2.3d}$$

2. Velocity correction step:

$$\boldsymbol{u}^k = \tilde{\boldsymbol{u}}^k - \frac{\Delta t}{\rho} \nabla p^k \quad \text{in } \widetilde{\Omega} \tag{2.4}$$

3. Tentative velocity step:

$$\frac{\rho}{\Delta t}(\tilde{\boldsymbol{u}}^{k+1} - \boldsymbol{u}^k) + \rho(\boldsymbol{u}^k \cdot \nabla)\tilde{\boldsymbol{u}}^{k+1} + \frac{\rho}{2}(\nabla \cdot \boldsymbol{u}^k)\tilde{\boldsymbol{u}}^{k+1} - \nabla \cdot (\mu \nabla \tilde{\boldsymbol{u}}^{k+1}) = \boldsymbol{0} \quad \text{in } \widetilde{\Omega} \tag{2.5a}$$

$$\tilde{\boldsymbol{u}}^{k+1} = \boldsymbol{g}_d^{k+1} \quad \text{on } \widetilde{\Gamma}_i \tag{2.5b}$$

$$\mu \boldsymbol{n} \cdot \nabla \tilde{\boldsymbol{u}}^{k+1} = \boldsymbol{0} \quad \text{on } \widetilde{\Gamma}_o \tag{2.5c}$$

$$\sum_{k=1}^{d-1} \boldsymbol{n} \cdot \left[\mu \nabla \tilde{\boldsymbol{u}}^{k+1} - \mathbb{1} p^k\right] \cdot \boldsymbol{t}_k + \gamma \tilde{\boldsymbol{u}}^{k+1} \cdot \boldsymbol{t}_k = 0 \quad \text{on } \widetilde{\Gamma}_w \tag{2.5d}$$

$$\boldsymbol{n} \cdot \left[\mu \nabla \tilde{\boldsymbol{u}}^{k+1} - \mathbb{1} p^k\right] \cdot \boldsymbol{n} + \beta \tilde{\boldsymbol{u}}^{k+1} \cdot \boldsymbol{n} = 0 \quad \text{on } \widetilde{\Gamma}_w. \tag{2.5e}$$

Note further that the algorithm starts with the projection and velocity correction steps instead of the tentative velocity step due to the fact that the pressure is required by the slip/transpiration conditions in the tentative velocity step. The given formulation is also convenient with regard to the optimization problem introduced in the subsequent section, since an iteration of the algorithm depends only on the previously computed tentative velocity, representing the *state variable* of the system. Optionally, steps 1 and 2 (computationally inexpensive compared to step 3) of the algorithm can be repeated at the end of each iteration to obtain p^{k+1} and $\boldsymbol{u}^{k+1}$ for post-processing purposes.

The slip/transpiration boundary conditions appear in both the tentative velocity step, Eqs. (2.5d) and (2.5e), and in the pressure projection step, Equation (2.3d). In the tentative velocity step, the slip/transpiration conditions are treated semi-implicitly with implicit velocity and explicit pressure from the previous time step. In the pressure projection step, while the slip part does not contribute, the transpiration boundary condition can be expressed via a Robin condition for the pressure with implicit treatment of the velocity and the pressure. This Robin condition, Equation (2.3d), is derived by considering the normal projection of the velocity correction equation (2.4)

and rearranging,

$$\boldsymbol{n} \cdot \nabla p^k = \frac{\rho}{\Delta t}(\tilde{\boldsymbol{u}}^k - \boldsymbol{u}^k) \cdot \boldsymbol{n} \quad \text{on} \quad \widetilde{\Gamma}_w. \tag{2.6}$$

Assuming that the corrected velocity $\boldsymbol{u}^k$ and the unknown pressure p^k satisfy the transpiration boundary condition,

$$\boldsymbol{n} \cdot \left[\mu \nabla \boldsymbol{u}^k - \mathbb{1} p^k\right] \cdot \boldsymbol{n} + \beta \boldsymbol{u}^k \cdot \boldsymbol{n} = 0 \quad \text{on} \quad \widetilde{\Gamma}_w, \tag{2.7}$$

we can replace $\boldsymbol{u}^k \cdot \boldsymbol{n}$ in (2.6) by (2.7), assuming $\beta > 0$ and obtain

$$\boldsymbol{n} \cdot \nabla p^k = \frac{\rho}{\Delta t}\left(\tilde{\boldsymbol{u}}^k \cdot \boldsymbol{n} - \beta^{-1}\left(p^k - \boldsymbol{n} \cdot \mu \nabla \boldsymbol{u}^k \cdot \boldsymbol{n}\right)\right) \quad \text{on} \quad \widetilde{\Gamma}_w.$$

As is usual in fractional step methods applied to blood flows [FGG07; BCF13], we neglect the viscous term. This results in the final form in Equation (2.3d). A similar discretization scheme was presented in Caiazzo et al. [Cai+10] in the context of immersed porous interfaces.

Note that the implicit treatment of the velocity in the slip/transpiration condition in the tentative velocity step avoids the need of a (in practice very restrictive) stability criterion on the time step. This is particularly reasonable in the context of the Chorin-Temam method, where additionally very small time steps can cause spurious pressure oscillations if equal order.

2.2.2 The Parameter Estimation Problem

Formulation and solution method

Let us introduce the following short-hand notation for the discretized numerical model,

$$X_k = \mathscr{A}_k(X_{k-1}, \theta),$$

where $\mathscr{A}_k$ is the model operator. In the case of the fractional step algorithm 1 given in section 2.2.1, the state corresponds to the discrete tentative velocity, $X_k := \tilde{\boldsymbol{u}}_h^k \in \mathbb{R}^n$ and $\mathscr{A}_k : \mathbb{R}^n \times \mathbb{R}^p \mapsto \mathbb{R}^n$ represents one time iteration of the discrete fractional step scheme. The physical parameters related to the boundary conditions are summarized in $\theta \in \mathbb{R}^p$, $p \geq 1$ denoting the number of parameters.

The aim of this work is to estimate θ from a sequence of N partial velocity measurements $Z_k \in \mathbb{R}^m$, $k = 1, \dots, N$ by means of PDE-constrained inverse problem. Here we assume that the measurements are related to the (true) state variable $X_k^t \in \mathbb{R}^n$ of the fluid model by means of a measurement operator $\mathscr{H} : \mathbb{R}^n \mapsto \mathbb{R}^m$, such that

$$Z_k = \mathscr{H} X_k^t + \zeta,$$

where $\zeta \in \mathbb{R}^m$ represents uncertainty due to measurement errors. The superscript t in X_k^t indicates the ground truth, whereas X_k refers to the state computed by the numerical model.

For the inverse strategy, we adopt a Bayesian estimation approach, where the a priori probability distribution of the parameters is corrected by using the measurements and the model. Assuming that both the probability distribution of the noise and the a priori parameters is Gaussian, the solution of the inverse problem reads: find

$$\begin{aligned} \hat{\theta} &= \arg\min_{\theta} J(\theta), \\ J(\theta) &= \frac{1}{2}\|\theta - \theta_0\|^2_{P_0^{-1}} + \sum_{k=1}^{N} \frac{1}{2}\|Z_k - \mathscr{H} X_k(\theta)\|^2_{W^{-1}}. \end{aligned} \tag{2.8}$$

θ_0 is an initial guess for the parameters and P_0 the associated covariance matrix. W is the covariance matrix associated to the measurement noise.

In this work we solve problem (2.8) approximately with the Reduced-order Unscented Kalman Filter (ROUKF), described in Moireau and Chapelle [MC11] and Bertoglio [Ber12]. It has the advantage of being derivative-free, hence well adapted to complex solvers, including multi-physical problems. It allows also to be flexibly adapted to different discretization strategies. Moreover, as an inherent property of the Kalman filter approach, the parameters are estimated recursively over time and therefore there is no need to store the full dynamic solution as in adjoint-based methods. The number of forward solutions grows linearly with the number of parameters to be estimated, but the forward solves can be parallelized since they are independent of each other. The ROUKF has become very popular in cardiovascular modeling in general and in particular in computational hemodynamics, see e.g. Bertoglio et al. [BMG12], Moireau et al. [Moi+13], Bertoglio et al. [Ber+14], Caiazzo et al. [Cai+17], and Müller et al. [MCB18].

The estimation procedure consists in the following steps: given a sequence of measurements and an approximation of the vessel geometry,

1. estimate the boundary coefficients with the ROUKF,
2. solve the forward problem with the optimized parameters,
3. post-process the optimized velocity and pressure solution of the forward problem.

Parameters

The inlet velocity (to be set via a Dirichlet boundary condition) is a priori unknown. In this work we assume a pulsating plug flow,

$$\boldsymbol{g}_d(\boldsymbol{x}, t) = -\bar{U}\boldsymbol{n}f(t),$$

where $\bar{U}$ is the velocity amplitude and $\boldsymbol{n}$ is the outward normal vector at the boundary. $f(t)$ is the waveform of the temporal oscillation, for instance

$$f(t) = \sum_{k=1}^{M} a_k \sin(\omega_k t), \qquad a_1 = 1.$$

The amplitude $\bar{U}$ is an unknown constant and needs to be recovered by the parameter estimation procedure. The waveform can easily be estimated prior to solving the inverse problem by postprocessing the measurements. Different parameterizations than the one given are possible. It is assumed here that $f(t)$ is known beforehand. In practice, a simple approach to obtain the waveform is computing the spatial mean of the velocity data given at the inlet boundary (assuming there are measurements at the inlet) for every measurement time and fitting the time profile. Otherwise, for some chosen small value of M, a_k and ω_k can be included in the parameter estimation.

If the slip/transpiration wall-model is used, the corresponding coefficients β and γ need to be estimated and are included in the parameter vector.

Summarizing, the parameter vector θ consists of the following boundary parameters:

- inflow condition, plug flow parameter $\bar{U}$
- slip parameter γ (if slip/transpiration BC, per boundary patch),
- transpiration parameter β (if slip/transpiration BC, per boundary patch).

2.3 Setup of the numerical experiments

Numerical experiments are conducted with the goal of comparing the slip/transpiration approach with standard no-slip boundary conditions in cases where geometric errors are present in the vessel wall. Three realistic synthetic test cases are analyzed, representing arteries with different degrees of stenoses. The setup of the test cases and the numeric solvers used for the forward and the inverse problems are explained in this section.

2.3.1 Geometries

Three geometries with different obstruction ratios of the stenosis of 40 %, 50 % and 60 % are considered. The latter case is illustrated in Figure 2.2. The study is conducted under the assumption $\widetilde{\Omega} \subset \Omega$, where the slip/transpiration boundary conditions have a sound physical justification. For each stenosis, three computational domains are generated: a reference domain with radius $R = 10\,\text{mm}$ in the unconstricted parts, which is considered the true domain, and two domains with the outer vessel walls shifted inward by $\Delta = 1\,\text{mm}$ and $\Delta = 2\,\text{mm}$. These offsets are considered segmentation errors with respect to the reference, due to uncertainty—e.g., limited resolution (of the order of Δ) and noise—in the medical images. In addition to the reference domain, Figure 2.2 shows the *approximate* domain for $\Delta = 2\,\text{mm}$. In this case, the difference in the radius is 20 % in the unconstricted sections, whereas in the throat of the stenosis with 60 % obstruction ratio, the radius is halved due to the errors in the geometry.

The true domain, Ω, is used to compute a reference solution for comparison with the estimation framework and to generate synthetic measurements. We pretend that for the pressure drop estimation, this true domain is unknown, but that one of the *approximate* domains is available ($\widetilde{\Omega}$).

2.3.2 Reference solution

Configuration

The reference solution is obtained by solving the fractional step system in the true domain Ω, with no-slip boundary conditions imposed on the lateral walls Γ_w. At the distal boundary, Γ_o, intersecting the flow, a homogeneous Neumann boundary condition is used, i.e., $g_n = 0$ in Eq. (2.3c) and (2.5c). On the proximal boundary, Γ_i, a pulsating plug flow profile is set via a Dirichlet boundary condition,

$$\boldsymbol{g}_d(\boldsymbol{x}, t) = -\bar{U}\boldsymbol{n}\sin(\omega t).$$

Note that $\boldsymbol{u} = \boldsymbol{0}$ on $\Gamma_i \cap \Gamma_w$ due to the no-slip boundary conditions. As above, $\boldsymbol{n}$ denotes the outward normal vector on the boundary. To mimic physiologically relevant conditions, we set $\omega = 2.5\pi\,\text{s}^{-1}$ and consider the time interval $t \in [0\,\text{s}, 0.4\,\text{s}]$, approximating the first half of a cardiac cycle, with the peak systole at $t = 0.2\,\text{s}$. The viscosity of blood (treated as a Newtonian fluid) is $\mu = 0.035\,\text{g/(cm s)}$ and the density $\rho = 1\,\text{g/cm}^3$. The amplitude of the pulsating inflow velocity is set to $\bar{U} = 43.75\,\text{cm/s}$, resulting in a peak Reynolds number based on the inlet of $Re = \frac{\rho 2\bar{U}R}{\mu} = 2500$. The Reynolds numbers based on the throat of the stenoses, Re_s, at the time of peak systole is (obtained from the solution presented below) are listed in Table 2.1.

Table 2.1: Reynolds numbers at peak systole based on the maximum velocity.

obstruction ratio	40 %	50 %	60 %
Re_s	4063	4863	6055

Discretization and numerical solution

The partial differential equations that constitute the fractional step scheme (2.3a)–(2.5e) are discretized in space with the finite element method, using $\mathbb{P}_1/\mathbb{P}_1$ basis functions for the velocity and the pressure on an unstructured tetrahedral mesh. Furthermore, streamline-diffusion stabilization is used with the formula for the stabilization parameter given in Bazilevs et al. [Baz+07]. Since backflow is likely to occur at the outflow boundary, velocity-penalizing backflow stabilization [Ber+17] is added on Γ_o. Note that also transpiration boundary conditions allow for inflow to occur, and therefore instabilities could potentially arise. In our numerical examples, however, we did not observe such problems, probably since the values of the transpiration parameter are high enough to control that advective energy. However, in case they appear, additional backflow stabilization terms could be added [Ber+17]. In particular, the tangential regularization method presented in Bertoglio and Caiazzo [BC14] would be the most suitable since it has shown to be the least intrusive for the pressure field [Ber+17].

The meshes use a reference cell size of $h = 0.25\,\text{mm}$ and consist of 3 086 306 to 3 606 417 tetrahedrons and 561 761 to 655 858 vertices, depending on the geometry. The constant time step size is $\Delta t = 1\,\text{ms}$.

The solver is implemented using the finite elements library FEniCS [Aln+15]. Preconditioned Krylov methods are used to solve the linear systems, provided by the PETSc package [Bal+18]. We make use of the fact that in the case of no-slip boundary conditions the velocity components are completely decoupled in the discretized versions of Eqs. (2.4) and (2.5a), and solve three smaller problems for each component separately with the same system matrix, instead of one large system for the complete velocity vector. For solving the tentative velocity equation we use BICGSTAB preconditioned with diagonal scaling. The pressure Poisson equation is solved with the CG method in the no-slip case and GMRES if slip/transpiration boundary conditions are used, in both cases with an algebraic multigrid preconditioner. The velocity correction system is solved using CG with a diagonal scaling preconditioner (cf. Saad [Saa03]).

2.3.3 Inverse solutions

Measurements

Synthetic partial measurements are generated from the reference solutions in such a way that the measurements are representative for typical 2D PC-MRI images. This means that 2D planes, intersecting with the 3D domain, are chosen on which the velocity is measured in one specified direction $\boldsymbol{d}$. I.e., the measurement is a scalar projection

$$c = \boldsymbol{u} \cdot \boldsymbol{d}, \quad |\boldsymbol{d}| = 1.$$

Since the inflow velocity is unknown and needs to be estimated, one plane will be placed at the inlet (Figure 2.4(a)). We consider here the x velocity component, orthogonal to the plane. A second plane intersects the domain lengthwise with an inclination of $\approx 10^\circ$ with respect to the

xz-plane. It connects points at the inlet, in the throat of the stenosis and at the outlet, as shown in Figure 2.4(b). The velocity component is chosen tangential to the plane in the streamwise direction (i.e., parallel to the longer edge).

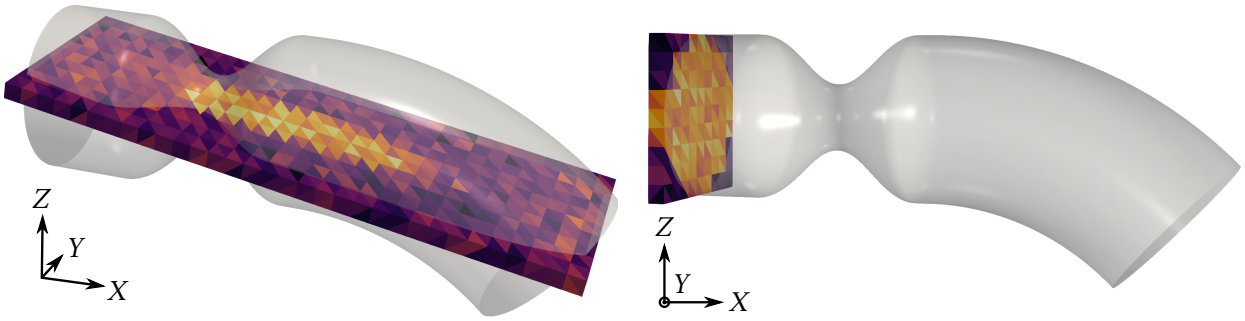

(a) Interior slice (b) Inlet slice

Figure 2.4: Measurement slices with reference geometry (60 %) at the peak time $t = 0.2$ s, with resolution $H = 2$ mm.

These slices have a finite thickness and consist in one layer of 3D voxels. The measurement data is represented on a mesh of uniform, equally sized tetrahedra. The thickness of the slices equals the element edge length on the plane, H. The element length is chosen to match typical voxel sizes for PC-MRI, namely $H = 1$ mm and 2 mm. We limit this study to the cases where the geometry error Δ is equal to the voxel size of the measurements, supposing that the same hypothetical image resolution was used to obtain the 3D vessel geometry and the PC-MRI velocity images. We refer to the case $\Delta = H = 1$ mm as 'Δ_1' and $\Delta = H = 2$ mm as 'Δ_2'.

The measurements are obtained by interpolating the selected component of the reference velocity to the barycenters of the tetrahedra of the slice meshes. The measurement data is considered constant within each tetrahedron, as can be seen in Figure 2.4 for noisy example data. The temporal sampling of the measurements is $\Delta T = 20$ ms, representing a typical value for 2D-PCMRI.

The noise intensity in the velocity data in PC-MRI is proportional to the *VENC* parameter of the scan, which encodes the intensity of the velocity encoding magnetic gradients [Car+18; LPP95]. Therefore, in practice the *VENC* is chosen as small as possible to reduce the noise in the velocity image. However, this parameter has to be set for each measurement sequence to a value higher than the expected maximum velocity in order to avoid velocity aliasing [Car+18; LPP95]. Since the *VENC* is fixed for the entire duration of a MRI scan, the noise level in all voxels is proportional to the global maximum velocity in space and time in the measurement region, regardless of the measured instantaneous local velocities. It is therefore realistic to assume that in practice, in order to improve the velocity-to-noise ratio, different values of the *VENC* parameter would be used for the different slices, according to the anticipated flow conditions. In the clinical practice it can be expected that high-quality acquisitions contain a velocity noise of 10 % of the peak velocity [Dyv+15].

Therefore, in the numerical experiments presented here, Gaussian white noise is added to each of the slices independently with a standard deviation of 15 % of the maximum velocity of the reference solution in the measurement region. Table 2.2 lists the values of the maximum velocities of the reference configurations (the complete results are presented in section 2.4.1) and the corresponding measurement noise intensities in terms of the standard deviation for the inlet slice and the interior slice with different coarctation ratios of the stenosis.

Table 2.2: Maximum velocities and standard deviation of Gaussian noise at the inlet and in the interior image slices, for different obstruction ratios of the stenosis.

	inlet slice	interior slice		
	all stenosis	40 % stenosis	50 % stenosis	60 % stenosis
max U	43.75 cm/s	140 cm/s	200 cm/s	320 cm/s
σ_{noise}	6.56 cm/s	21 cm/s	30 cm/s	48 cm/s

Forward solution

The optimization procedure requires evaluations of the forward model, i.e., the fractional step algorithm. The configuration of the forward model and solvers is identical to the reference simulations, with the following exceptions:

- the 'approximate' computational domains $\widetilde{\Omega}$ with geometric errors are used,
- no-slip or slip/transpiration boundary conditions on $\widetilde{\Gamma}_w$,
- boundary parameters are unknown and estimated (see the next paragraph).

Note that using slip/transpiration boundary conditions in implicit form, the velocity components in the momentum equation (2.5a) are coupled and cannot be solved for separately. This results in an increase in CPU time compared to the no-slip case. In the case of slip/transpiration boundary conditions, the momentum equation is solved with GMRES, preconditioned with algebraic multigrid. With no-slip boundary conditions the same solvers are used as for the reference solution, see section 2.3.2.

Physical model parameters

We compare two wall models:

1. standard no-slip boundary conditions and
2. slip/transpiration boundary conditions.

The only parameter of the no-slip model is the plug flow parameter at the inlet. It seems therefore reasonable to estimate the plug flow parameter only from measurements given at the inlet. Regarding the geometric errors, it will be examined if the results can be improved by providing additional measurements in the interior of the domain, i.e., by using both measurement slices discussed above. In the case of slip/transpiration boundary conditions, measurements at the inlet and in the interior will be used in order to estimate the plug flow parameter and the boundary coefficients β and γ.

Summarizing, the parameters to be estimated are:

- **no-slip**
$$\theta = \bar{U},$$
- **slip/transpiration**
$$\theta = \left(\bar{U},\ \beta,\ \gamma\right).$$

Kalman filter parameters

The physical parameters to be estimated (see paragraph above) are reparameterized as $\theta' = \log_2(\theta)$. By optimizing θ', it is ensured that the physical parameters θ, which enter the fluid model, stay positive. This is required to guarantee the positivity of the variational formulation of the forward problem and in agreement with basic physical intuition, since, for instance, with a negative slip parameter the wall-tangential flow would be accelerated by the traction, instead of slowed.

Initial guesses for the parameters and the associated uncertainties have to be provided for the ROUKF algorithm. We choose

$$\boldsymbol{\theta}_0 = \begin{Bmatrix} 40 \\ 0.001 \\ 5000 \end{Bmatrix} \quad \begin{matrix} \text{plug flow,} \\ \text{slip parameter,} \\ \text{transpiration parameter.} \end{matrix}$$

The initial variances of the reparameterized parameters θ' are set to $\sigma_0^2 = 1$. The weights W in (2.8), representing the uncertainty in the measurements, is set to the known noise intensity in each of the slices, i.e., $W = \mathrm{diag}(\sigma)$, with $\sigma \in \mathbb{R}^m$ the vector of the noise standard deviations in all m measurement data points. In practice, σ is the estimated noise level proportional to the VENC value used for each measurement.

2.3.4 Summary

The cases included in this study are summarized in Table 2.3. In total, 540 optimization problems

Table 2.3: Summary of numerical experiments using no-slip or slip/transpiration boundary conditions

model	obstruction ratio	measurement slices	Δ, H	parameters	random samples
no-slip	{40 %, 50 %, 60 %}	inlet only	$\{\Delta_1, \Delta_2\}$	$\bar{U}$	30
no-slip	{40 %, 50 %, 60 %}	inlet + interior	$\{\Delta_1, \Delta_2\}$	$\bar{U}$	30
slip/transp.	{40 %, 50 %, 60 %}	inlet + interior	$\{\Delta_1, \Delta_2\}$	$\bar{U}, \beta, \gamma$	30

with subsequent forward simulations with each optimized set of parameters are solved. Each simulation is computed on 16 Intel Xeon 2.5 GHz cores on the Peregrine HPC cluster of the University of Groningen.

2.4 Numerical results

The results obtained with no-slip and with slip/transpiration boundary conditions are mainly analyzed in terms of the pressure drop and the velocity error. The pressure drop is defined as the difference in the pressure averages at two cross-sections, upstream and downstream of the

stenosis,

$$\delta p^k = \frac{1}{|\Gamma_i|}\int_{\Gamma_i} p^k - \frac{1}{|\Gamma_o|}\int_{\Gamma_o} p^k, \tag{2.9}$$

with $|\Gamma_\star|$ denoting the area of a boundary patch and the superscript k the kth time step. Note that the pressure drop is determined by the pressure gradient alone and does not depend on fixing the pressure constant. The velocity error is considered in the L^2-norm over the whole approximate domain, scaled by the global maximum velocity, and defined as

$$\mathscr{E}^k := \frac{\|\hat{\boldsymbol{u}}^k - \mathcal{I}\boldsymbol{u}^k\|_{L^2(\widetilde{\Omega})}}{\max_k \|\mathcal{I}\boldsymbol{u}^k\|_{L^2(\widetilde{\Omega})}}. \tag{2.10}$$

Here $\mathcal{I}$ is the operator which interpolates the reference velocity $\boldsymbol{u}^k$ to the space of the optimized velocity $\hat{\boldsymbol{u}}^k$, i.e., from the reference geometry Ω to the approximate geometry, $\widetilde{\Omega}$.

We proceed by first presenting the numerical solutions of the reference setups, followed by a discussion of the results of the inverse problems using no-slip boundary conditions on the walls. Lastly, we present the results of the slip/transpiration model and compare them to the no-slip results.

2.4.1 Reference solution and measurements

We briefly discuss the numerical solutions of the reference cases. These form the basis of the subsequent analysis of the results of the optimization problems, because they serve as the ground truth which the solutions of the inverse problems are compared to. In addition, the measurements are generated from the velocity solution of the reference, as was explained above.

Streamlines of the velocity field are shown in Figs. 2.5–2.7, for peak systole, $t = 0.2\,\mathrm{s}$. The domain is cut along the XZ plane and only one half is shown, since the flow is approximately symmetrical with respect to that plane. The figures furthermore include the interior measurement plane with a resolution of $H = 2\,\mathrm{mm}$.

Since the flow is of pulsating character, dynamic effects are very pronounced. We restrict the discussion here to the flow situation at peak systole, $t = 0.2\,\mathrm{s}$, where the maximum velocities and pressure drops can be expected. Round jets are formed due to the constrictions, surrounded by annular recirculation zones. The jets impinge on the curved wall and are mainly deflected towards the outlet. Secondary circulations form in particular below the jets and are fed by azimuthal wall-bound flow produced by the impingement. In the example with 40 % obstruction ratio, this effect is most pronounced. The recirculation velocities are considerable compared to the velocities of the jet, and the strong recirculation bubble acts back on the jet flow by pushing it upward. Such an interaction between recirculation zones and jets does not appear in the cases of more severe stenosis, 50 % and 60 %, where the jets remain unperturbed. The magnitude of the secondary flow patterns seems negligible in comparison to the very high jet velocities. The snapshot of the measurement of the 40 % case, Figure 2.5(a), shows that the recirculation is captured to some degree in the measurements. There is a 'dead region' of low in-plane velocities in the center, near the outlet, surrounded by higher magnitude wall-bound flow. Such features are not recognizable in the 50 % and 60 % cases due to the high noise intensity. Weak backflow is present at the outflow boundary in all examples, confirming the need for backflow stabilization.

Isosurfaces of the corresponding pressure fields are shown in Figure 2.8. The pressure is close

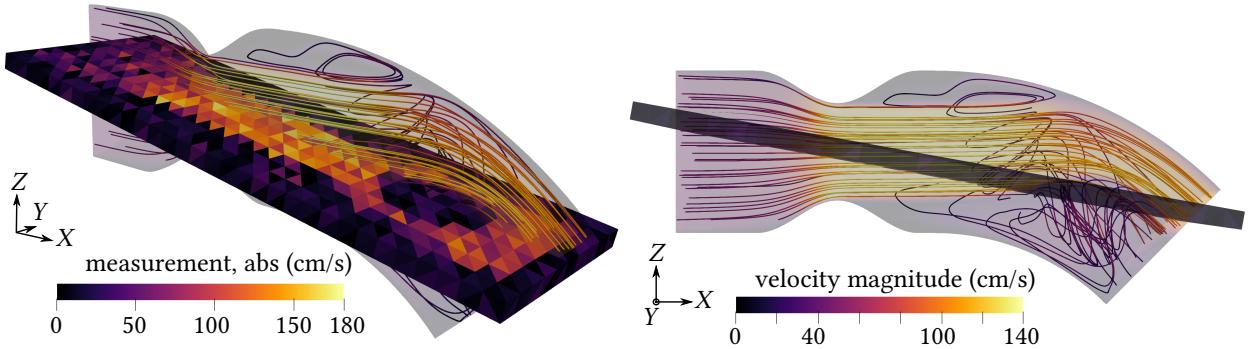

(a) 3D view (b) XZ view

Figure 2.5: Streamlines of the reference flow and sample noisy velocity measurement (in-plane component, Δ_2) at peak systole for 40 % obstruction ratio.

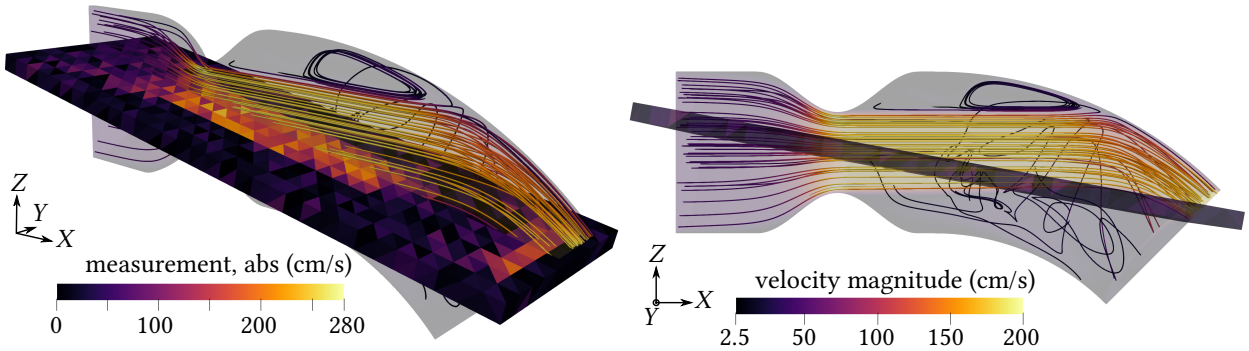

(a) 3D view (b) XZ view

Figure 2.6: Streamlines of the reference flow and sample noisy velocity measurement (in-plane component, Δ_2) at peak systole for 50 % obstruction ratio.

to zero along the outflow boundaries, due to the homogeneous Neumann boundary condition. As the flow accelerates in the stenosis, strong very localized pressure minima appear at the wall in the narrowest section, and propagated downstream. The jet impingement creates a region of relatively high pressure in the region of the impact. The maximum pressure is naturally located upstream of the stenosis, and distributed rather uniformly. The maximum pressure is highest for the stenosis with 60 % obstruction ratio.

2.4.2 Estimation results for the no-slip model

Consider first the scenario where measurements are given only at the inlet. The PDE-constrained optimization problem is solved with no-slip boundary conditions, estimating the plug flow parameter.

Statistics of the plug flow parameters estimated from measurements at the inlet with different resolutions and geometry errors in the computational domain $\Delta = H = 1\,\text{mm}$ and $2\,\text{mm}$ are listed in Table 2.4 Since the ROUKF algorithm optimizes the $\log_2$-reparameterized parameter and assumes θ to be normally distributed, a lognormal distribution can be considered for the physical parameters, 2^θ. The table shows the mean and the square root of the variance of the physical non-

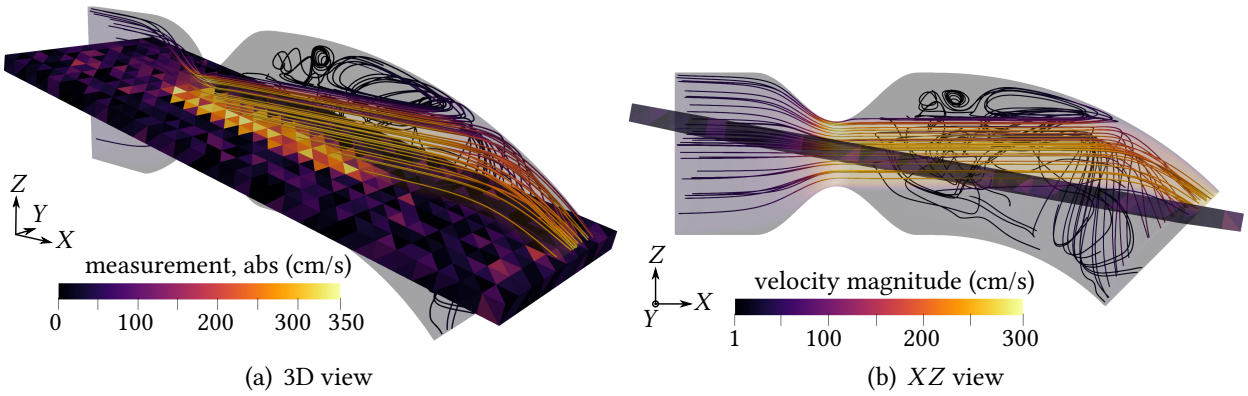

(a) 3D view (b) XZ view

Figure 2.7: Streamlines of the reference flow and sample noisy velocity measurement (in-plane component, Δ_2) at peak systole for 60 % obstruction ratio.

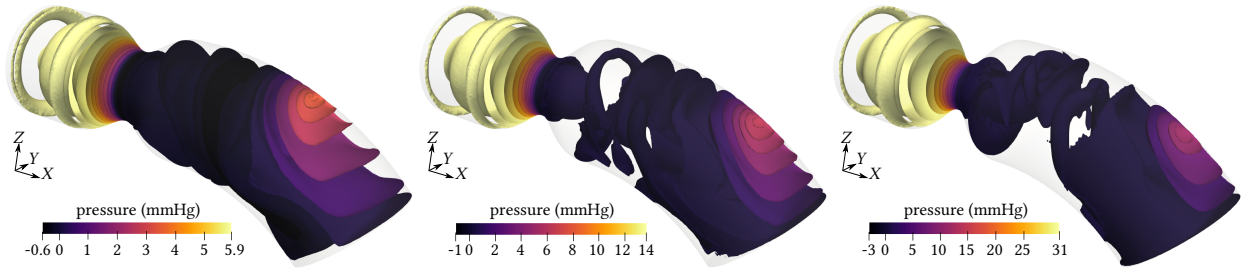

(a) 40 % stenosis (b) 50 % stenosis (c) 60 % stenosis

Figure 2.8: Pressure isosurfaces of reference problems with different coarctation ratios at the peak time $t = 0.2$ s.

logarithmized parameter assuming a lognormal distribution over 30 identical repetitions of the experiment for independent random realizations of measurement noise. The plug flow parameter

Table 2.4: Mean and square root of the variance of the estimated plug flow parameter, using no-slip BCs and measurements only at the inlet. Statistics from 30 independent realizations of noisy measurements. Ground truth: 43.75 cm/s.

	40 % stenosis		50 % stenosis		60 % stenosis	
Δ (mm)	mean	$\sqrt{\text{Var}}$	mean	$\sqrt{\text{Var}}$	mean	$\sqrt{\text{Var}}$
1	43.98	0.06	43.98	0.06	43.93	0.05
2	43.67	0.15	43.61	0.20	43.71	0.13

is recovered with a very good accuracy, with errors of less than 0.5 % compared to the ground truth. The variability of the parameter is generally very small, being largest for $\Delta = 2$ mm in all investigated obstruction ratios, possibly due to the lower resolution of the measurements and thus less data being available.

The mean pressure drop, obtained by forward-solving the Navier-Stokes equations with the optimized parameters, is visualized in Figure 2.9 over time for the three investigated obstruction ratios and for both geometry errors/measurement resolutions, $\Delta_1 = 1$ mm and $\Delta_2 = 2$ mm. The

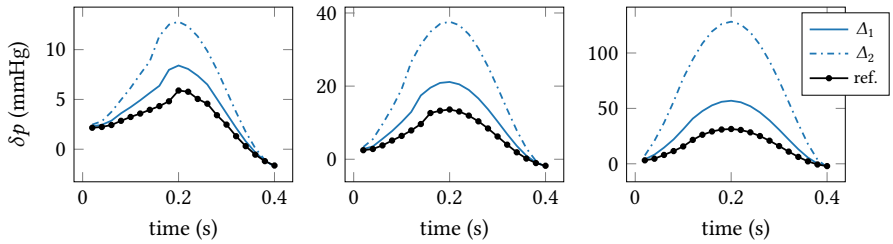

(a) 40 % (b) 50 % (c) 60 %

Figure 2.9: Mean pressure drop with no-slip BCs for 30 realizations of noise. The peak standard deviation is of the order of 0.1 % of the mean. Measurements were given at the inlet with resolution $H = \Delta$, Δ denoting the error in the geometry (cf. legend); $\Delta_1 = 1$ mm and $\Delta_2 = 2$ mm.

standard deviation over 30 experiments is below 0.5 % of the mean value at peak systole, similarly to the plug flow parameter. This indicates that the procedure is very robust to noise and with respect to small changes in the parameter.

On the other hand, it is immediately evident from the figures that the accuracy of the pressure gradient reconstruction is very poor, especially for large obstruction ratios, when errors in the geometry are present. In the best scenario, the mildest stenosis with 40 % obstruction and for Δ_1 (i.e., for the smaller geometry error and measurement resolution $\Delta = H = 1$ mm), the error in the pressure drop at the peak is about 50 %. With Δ_2 ($\Delta = H = 2$ mm), the error exceeds 100 %. For the more severe 50 % and 60 % stenoses, the peak error is of the order of 100 % for Δ_1, and for Δ_2 rises up to 300 % to 400 %.

The pressure drop estimates are improved by taking into account additional measurements in the interior. Figure 2.10 shows the pressure drops obtained for the case where two measurement slices were used (label 'II' in the figure), at the inlet and the lengthwise intersecting slice, in comparison to measurements only at the inlet (label 'I', same curves as in Figure 2.9). The discrepancy between the model and reference pressure gradient solutions is reduced by a large factor in the case of $\Delta = 2$ mm, and to a lesser degree for $\Delta = 1$ mm.

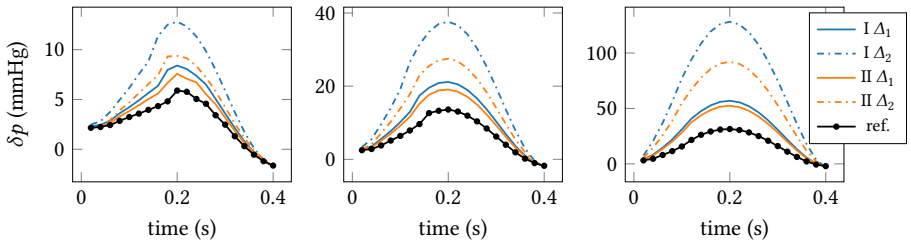

(a) 40 % (b) 50 % (c) 60 %

Figure 2.10: Mean pressure drop with no-slip BCs for 30 realizations of noise; standard deviation of the order of 0.1 % of the mean. Measurements given on two slices (labeled 'II') vs. measurements only at the inlet ('I'). $\Delta_1 = 1$ mm and $\Delta_2 = 2$ mm (cf. Figure 2.9).

Table 2.5 compares the corresponding estimated plug flow parameters for the cases with measurements at the inlet (rows labeled 'I') and measurements at the inlet and in the interior slice ('II'). By considering measurements in the interior, the estimated plug flow parameter deviates

Table 2.5: Mean and square root of the variance of the estimated plug flow parameter, using no-slip BCs and measurements only at the inlet. Statistics from 30 independent realizations of noisy measurements. Ground truth: 43.75 cm/s.

		40 % stenosis		50 % stenosis		60 % stenosis	
Δ (mm)	# slices	mean	$\sqrt{\text{Var}}$	mean	$\sqrt{\text{Var}}$	mean	$\sqrt{\text{Var}}$
1	I	43.98	0.06	43.98	0.06	43.93	0.05
	II	41.48	0.05	41.58	0.05	41.82	0.06
2	I	43.67	0.15	43.61	0.20	43.71	0.13
	II	37.40	0.11	36.46	0.19	35.06	0.14

significantly from the ground truth, compared to inlet-only measurements, the error is largest for the 60 % stenosis with $\Delta = 2$ mm with 20 % underestimation of the ground truth, compared to 0.1 % using only measurements at the inlet. Hence, the improved pressure drop estimation comes at the cost of large errors in the inflow profile.

Figure 2.11 shows the velocity error, defined by Equation (2.10), over time. The velocity error globally increases slightly with augmenting obstruction ratios of the stenoses, but to a much lesser degree than the error in the pressure drop. Computations with a bigger geometry error, i.e., Δ_2 instead of Δ_1, lead to increased errors in the velocity by roughly 50 % in all three cases. By taking into account interior measurements (lines labeled 'II' in Figure 2.11), the errors are slightly reduced, especially for Δ_2. Again, the results are very robust to noise with relative standard deviations of the velocity error of the order of 0.1 % at peak systole.

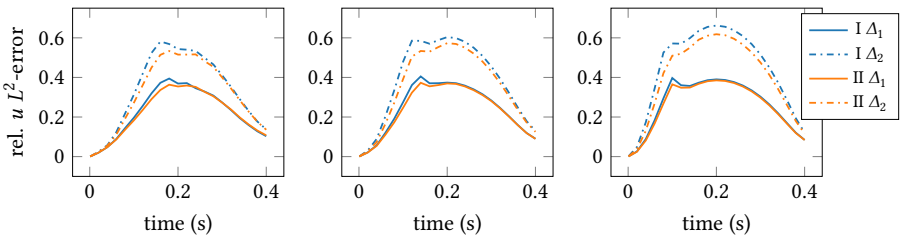

(a) 40 % (b) 50 % (c) 60 %

Figure 2.11: Mean velocity error with no-slip BCs for 30 realizations of noise; peak systole standard deviation of the order of 0.1 % of the mean. Measurements given on two slices ('II') vs. measurements only at the inlet ('I'). $\Delta_1 = 1$ mm and $\Delta_2 = 2$ mm.

The observed poor pressure drop estimates and large errors in the inflow velocity render the described procedure using no-slip boundary conditions inadequate for the application discussed here. The decreased radius in the stenosis gives rise to a much higher pressure drop if the inflow velocity is similar to the reference case. In order to fit interior measurements (for instance the jet velocities), if given, the inflow velocity has to be strongly decreased.

This reasoning motivates investigating slip/transpiration boundary conditions. The results of the numerical experiments using slip/transpiration boundary conditions are presented in the following section.

2.4.3 Estimation results for the slip/transpiration model

Consider the case where measurements are given at the inlet and on the interior slice. The pressure drop obtained with the slip/transpiration boundary conditions is displayed in Figure 2.12 in comparison to the no-slip results, also considering both measurement slices. The accuracy of the

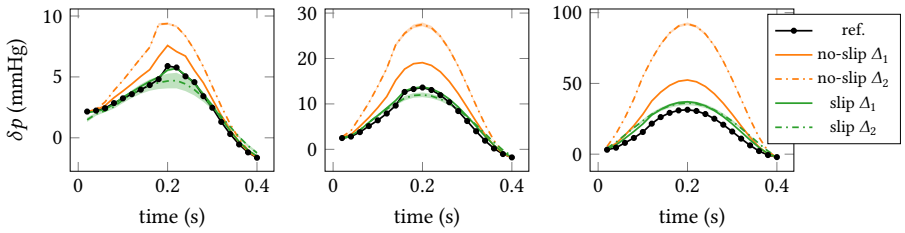

(a) 40 % (b) 50 % (c) 60 %

Figure 2.12: Pressure drop comparison, slip/transpiration ('slip') vs. no-slip. Mean values with $\pm 2\sigma$ bands over 30 samples of measurements, given at the inlet and in the interior plane, with resolution/geometry error $\Delta_1 = 1$ mm and $\Delta_2 = 2$ mm.

pressure drop estimation is greatly improved in all cases. Especially with $\Delta = 1$ mm, for the 40 % and 50 % cases, the estimated pressure drop now coincides almost perfectly with the ground truth. In the most severe 60 % stenosis, the pressure drop is overestimated by 15 % for both Δ_1 and Δ_2. Using the Δ_2 geometry and measurements leads to a slight underestimation of the pressure drop in the 50 % example, and to a more pronounced underestimation for the 40 % case.

The figure also shows the variability of the pressure drop by means of $\pm 2\sigma$ bands computed for 30 realizations of noise. The spread seems negligible for all cases except in the setting of the 40 % stenosis, using the slip/transpiration model and Δ_2 measurements, where a larger variability is present in the pressure drop than in the other experiments. Increasing the sample size to 50 for this example did not significantly reduce the variance observed in the pressure drop. Albeit the larger spread with the slip/transpiration model in this particular case, the estimated pressure drop was still observed to be closer to the ground truth in all simulated cases. This is shown in Figure 2.13, where the error in the pressure drop at peak systole is plotted for the 30 investigated realizations of noisy measurements. The slip/transpiration model underestimates the ground truth by approximately 10 % to 25 % whereas the error with the no-slip model is around 60 %.

The corresponding relative L_2 velocity errors are shown in Figure 2.14. In all cases, the error is smaller with the slip/transpiration model, the relative improvement being the most pronounced for 40 %. Some variability in the error can be observed after the peak time $t = 0.2$ s in the 40 % case for both values of Δ, using the slip/transpiration model.

Statistics of the estimated plug flow parameter are compared for both models in Table 2.6. With slip/transpiration boundary conditions, the ground truth is recovered with very good accuracy for both Δ_1 and Δ_2. In all settings the errors are significantly smaller compared to those obtained with no-slip boundary conditions. The variability is generally small with the square root of the variance below 1 % of the mean. In the case of 40 % obstruction ratio with Δ_2 the square root of the variance is somewhat increased for slip/transpiration conditions, to 2 % of the mean. This coincides with the observation of an increased variability in the pressure drop for the 40 % case with Δ_2.

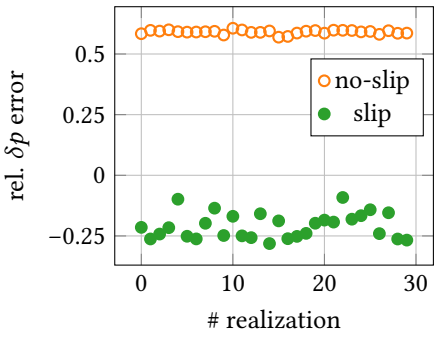

Figure 2.13: Relative, signed pressure drop error at peak systole compared for no-slip and slip/transpiration boundary conditions, for 40 % obstruction ratio and Δ_2. Each point corresponds to the result obtained for one realization of noisy measurements.

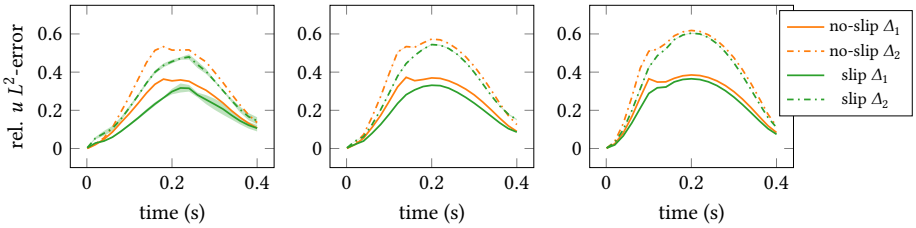

(a) 40 % (b) 50 % (c) 60 %

Figure 2.14: Velocity error comparison, slip/transpiration (labeled 'slip') vs. no-slip. Mean values with $\pm 2\sigma$ bands over 30 samples of measurements, given at the inlet and in the interior plane, with resolution/geometry error $\Delta_1 = 1$ mm and $\Delta_2 = 2$ mm.

Table 2.6: Mean and square root of variance of the estimated plug flow parameter $\theta_{\bar{U}}$, using slip/transpiration and no-slip BCs, for 30 independent realizations of noisy measurements at the inlet and in the interior. Ground truth: 43.75 cm/s.

		40 % stenosis		50 % stenosis		60 % stenosis	
Δ (mm)	model	mean	$\sqrt{\text{Var}}$	mean	$\sqrt{\text{Var}}$	mean	$\sqrt{\text{Var}}$
1	noslip	41.48	0.05	41.58	0.05	41.82	0.06
	slip	43.19	0.13	44.46	0.07	44.21	0.08
2	noslip	37.40	0.11	36.46	0.19	35.06	0.14
	slip	44.01	1.03	44.80	0.16	45.40	0.13

For the transpiration and slip parameters no ground truth values are available. The transpiration parameter β, summarized by Table 2.7, increases with the obstruction ratio. The stronger the stenosis and jet, the higher is therefore the resistance to flow across the boundary in the normal direction. The parameter is smaller for Δ_2 than for Δ_1, since in the former case the boundaries are located deeper inside the true flow domain and more transpiration has to be permitted. For the 40 % case the variance-to-mean ratio is larger than for the 50 % and 60 % geometries.

The slip parameter exhibits a more complex behavior. Its statistics are summarized in Table 2.8. While under Δ_1 the mean of the slip parameter is of the same order of magnitude for 40 %, 50 % and 60 % stenoses, the mean values vary strongly with Δ_2. Using the 50 % and 60 % geometries in

Table 2.7: Transpiration parameter β. Mean and square root of variance for 30 samples of noisy measurements (inlet & interior slices).

	40 % stenosis		50 % stenosis		60 % stenosis	
Δ (mm)	mean	$\sqrt{\text{Var}}$	mean	$\sqrt{\text{Var}}$	mean	$\sqrt{\text{Var}}$
1	6684.48	257.45	8654.17	150.88	20 425.33	475.04
2	2075.99	394.95	3573.48	147.31	8413.68	318.07

Table 2.8: Slip parameter γ. Mean and square root of variance for 30 samples of noisy measurements (inlet & interior slices).

	40 % stenosis		50 % stenosis		60 % stenosis	
Δ (mm)	mean	$\sqrt{\text{Var}}$	mean	$\sqrt{\text{Var}}$	mean	$\sqrt{\text{Var}}$
1	0.41	0.36	0.43	0.04	0.24	0.43
2	0.59	0.97	6.23×10^{-8}	4.09×10^{-7}	2.75×10^{-5}	1.08×10^{-5}

the Δ_2 setting the slip parameter is smaller by orders of magnitude than the corresponding values observed with Δ_1, and tends towards free-slip conditions. A high variability in the slip parameter is observed for 40 %, in accordance with the behavior of the pressure drop and the velocity error. For 50 % obstruction ratio, the square root of the variance is much smaller for Δ_1, only about 10 % of the mean value, and high for Δ_2. In the 60 % case the variance in the parameter is elevated for both Δ_1 and Δ_2. In these scenarios the variability in the pressure drop and the velocity error was seen to be negligible.

The increased variability obtained with the slip/transpiration model in the case of 40 % obstruction ratio, compared to the more severe stenoses with 50 % and 60 %, can most likely be attributed to the more complex recirculating flow patterns in the former case. The wall-bound, mainly azimuthally circulating flow of the 40 % stenosis is very sensitive to the wall parameters. The interior measurement slice, however, contains little information about these flow features, as can be seen in Figure 2.5(a). The optimized slip and transpiration parameters must accommodate principally to the flow in the stenosis, the impingement region of the jet and also the recirculating flow caused by the impingement. In the 50 % and 60 % cases the secondary flow patterns seem to be of negligible importance. The wall parameters only have to account mainly for the correct behavior in the stenosis and in the impingement region of the jet.

2.5 Conclusions

We presented a framework for estimating quantities derived from the hemodynamic pressure and/or velocity, using 2D-PCMRI velocity measurements, a reconstruction of the blood vessel geometry of interest, and a suitable fluid model. The focus of the analysis was on the effect of errors in the wall position, e.g., due to imperfect image segmentation, on the estimated pressure drop in the case of arterial stenosis. Our results are consistent with other studies of the issue of geometric uncertainties. In Moore et al. [MSE97] and Moore et al. [Moo+99] the importance of geometric errors on MRI-based hemodynamics was studied for the first time. In Sankaran et al. [SGT15a] and Sankaran et al. [SGT15b; San+16], uncertainty quantification of CT-based blood flow simulations showed an important impact of geometric uncertainties on the hemodynamic

pressure in stenotic coronary arteries and a strong sensitivity of the wall shear stress with respect to geometry errors in a synthetic carotid artery bifurcation aneurysm [SM11]. Also very recently in Minakowski and Richter [MR19], the problem of geometric uncertainty was studied theoretically, providing error bounds and finding a large impact of small boundary variations on the numerical solution. However, to the best of the authors' knowledge, this is the first time that a methodology for coping for geometric uncertainties is proposed. In order to reduce the errors induced in the pressure drop by using no-slip boundary conditions on inaccurate vessel walls, we employed slip/transpiration boundary conditions, the coefficients of which were included in the parameter estimation procedure.

Both wall models were compared for synthetic test cases of stenosis with different severities. It was observed that no-slip conditions imposed on inaccurate walls (i.e., shifted with respect to a ground truth) indeed induce huge errors in the estimated pressure drop. Optimized slip/transpiration boundary conditions allowed the temporal evolution of the pressure drop to be estimated with very good precision, and additionally delivered accurate estimates of the inlet velocity. The method proved capable of handling 2D-PCMRI-type measurements, i.e., a scalar velocity component in a defined direction, on selected pseudo-2D planes, with realistic, coarse image resolutions and suffering from strong random noise, especially in the regions of low velocities.

In the presented study, the parameters of the slip/transpiration boundary conditions were considered constant over the whole boundary and in time. Allowing for some variation in space and time is likely to further improve the results, especially with regard to more complex realistic geometries and real data.

A limitation of the study was the assumption that the approximate domain was a subset of the true domain. This is the regime where an improved accuracy with slip/transpiration boundary conditions can be reasonably expected. However, the model is also applicable to the case where the assumption does not hold, but a significant reduction of the errors obtained with no-slip boundary conditions should not be expected. In such a scenario the slip/transpiration model seems to tend towards no-penetration/free slip behavior and yields marginally reduced errors in the pressure drop, compared to the no-slip case.

The methodology is limited to large vessels, where 2D-PCMRI scans are feasible and the assumption of blood as a Newtonian fluid is reasonable. Elastic deformation of the vessel walls was neglected and combining the slip/transpiration model with fluid–structure interaction remains a question for future work. Furthermore, the flow conditions are likely to be in the regime of transition to turbulence. It seems worthwhile, especially with regard to real data, exploring the discussed phenomena using turbulence models, i.e., large eddy simulation.

Appendix

2.A Slip boundary condition for the Poiseuille flow

In settings where an analytical solution of the incompressible Navier-Stokes equations is known, the coefficients of the slip/transpiration boundary conditions can be determined exactly. For instance, consider the simple Poiseuille flow example of steady state flow through a straight tube with constant circular cross-section. In this situation, the Navier-Stokes equations simplify to

$$\frac{1}{r}\left(r\frac{\mathrm{d}u}{\mathrm{d}r}\right) = -\frac{G}{\mu}, \tag{2.11}$$

in cylinder coordinates, where u is the axial velocity component. The radial and the angular components are zero. G is a constant pressure gradient acting on the fluid in the axial direction. Equation (2.11) can be solved by assuming a symmetry boundary condition $\frac{\mathrm{d}u}{\mathrm{d}r} = 0$ at $r = 0$, and a no-slip boundary condition $u(r = R) = 0$, where R is the radius of the tube. The resulting velocity profile along the radial coordinate r is given by

$$u(r) = \frac{G}{4\mu}(R^2 - r^2). \tag{2.12}$$

Consider now the situation where the (virtual) boundary of the domain is moved away from the wall to $r = R'$ in the interior of the tube. Let us pretend that the velocity distribution is unknown, but that we know R, R', and the fact that $u(R) = 0$. A boundary condition at this virtual boundary $r = R'$ can be defined in terms of a Robin condition:

$$\mu \left.\frac{\mathrm{d}u}{\mathrm{d}r}\right|_{r=R'} + \gamma u(R') = 0. \tag{2.13}$$

The solution of Equation (2.11) with boundary conditions $\frac{\mathrm{d}u}{\mathrm{d}r} = 0$ at $r = 0$ and the Robin condition (2.13) is given by Equation (2.12) if the proportionality factor γ is chosen such that

$$\gamma = 2\mu\frac{R'}{R^2 - R'^2}.$$

Here, γ depends only on the geometry.

Chapter 3

Validation of 4D-flow-based pressure difference estimators

The work presented in this chapter was submitted for publication and is, at the time of this writing, under review: D. Nolte, J. Urbina, J. Sotelo, C. Montalba, L. Sok, A. Osses, C. Bertoglio, and S. Uribe. "Validation of 4D-Flow-Based Pressure Map Estimators". In: *Journal of Magnetic Resonance Imaging* (submitted 2019)

3.1 Introduction

In this chapter, the relative pressure Stokes estimator (STE) [Švi+16] is applied for the first time to real 3D PC-MRI data. Using data acquired in aortic flow phantoms with coarctation of the aorta (CoA) of different severities and in two CoA patients, the STE method is compared to the classical PPE method, reviewed in Section 1.4. Pressure differences measured by means of catheterization are used as a reference. The PPE and STE methods are analyzed in terms of accuracy with respect to catheterization data and regarding the sensitivity with respect to the image resolution and the lumen segmentation. Furthermore, the effects of the CoA severity and cardiac output are investigated.

3.2 Theory

Maps of relative pressure can be computed directly from the velocity measurements by evaluating the linear momentum conservation equation of the incompressible Navier–Stokes model, i.e.

$$-\nabla p = \rho \frac{\partial \boldsymbol{u}}{\partial t} + \rho(\boldsymbol{u} \cdot \nabla)\boldsymbol{u} - \mu \Delta \boldsymbol{u} \tag{3.1}$$

where ρ is the density of the fluid and μ its dynamic viscosity, $\boldsymbol{u} : \Omega \longrightarrow \mathbb{R}^3$ denotes the velocity vector field and $p : \Omega \longrightarrow \mathbb{R}$ is the pressure field. Ω represents the computational domain obtained from segmenting the 4D flow images. By inserting the 4D flow velocity data into $\boldsymbol{u}$, the pressure gradient can be recovered by applying numerical methods. In this work we use the Poisson Pressure Equation (PPE) approach [Ebb+02; EF09; Kri+12] and the Stokes Estimator (STE) [Švi+16; CN86], which will be described in this section.

Discretizing Equation (3.1) in time, here with the first order backward difference formula, gives the following expression for the pressure gradient:

$$-\nabla p^k = \rho \frac{\boldsymbol{u}^k - \boldsymbol{u}^{k-1}}{\Delta t} + \rho(\boldsymbol{u}^k \cdot \nabla)\boldsymbol{u}^k - \mu \Delta \boldsymbol{u}^k. \tag{3.2}$$

The indices $1 \leq k \leq N$ denote the time snapshot of the measurements and Δt the temporal offset between two consecutive measurements or cardiac phases, with time stamps $t_k = k\Delta t$. For the first step, $k = 1$, a forward difference has to be used instead since no previous measurements are available. Evaluating the right hand side of Equation (3.2) for spatially undersampled and noisy velocity measurements $\boldsymbol{u}_m$,

$$R^k := \rho \frac{\boldsymbol{u}_m^k - \boldsymbol{u}_m^{k-1}}{\Delta t} + \rho(\boldsymbol{u}_m^k \cdot \nabla)\boldsymbol{u}_m^k - \mu \Delta \boldsymbol{u}_m^k. \tag{3.3}$$

yields a pressure gradient estimate $\nabla \hat{p}^k \approx \nabla p^k$, given by

$$-\nabla \hat{p}^k = R^k. \tag{3.4}$$

Higher order time schemes, while more accurate in theory for small time steps, are not beneficial in the present context due to the coarse time sampling of the measured velocities. Note that in previous works a second-order mid-point scheme was used, see for instance Bertoglio et al. [Ber+18b] and Marlevi et al. [Mar+19]. However, this leads to stronger underestimations of the pressure differences. This can be explained from the nature of time under-sampling in MRI, namely that u_m^k is reconstructed by assuming the flow velocity being constant within the interval $[t^k - \Delta t/2, t^k + \Delta t/2]$ rather than being an instantaneous measurement at t^k [Mar+12].

It is important to remark that in direct methods derived from the Navier-Stokes equations, e.g., Bernoulli-based, PPE, STE, at any instant of time, the pressure is uniquely defined up to a constant (with respect to the spatial coordinates). Therefore, only instantaneous pressure differences between different locations can be compared at different times. Catheterization or sphygmomanometer pressure measurements are taken relative to the atmospheric pressure. Hence, the pressures are calibrated with respect to a global reference and pressure values can be compared at different times. A common measure in the clinical practice are the so-called peak-to-peak pressure differences, which compares the largest pressure difference registered between two locations at any time during the cardiac cycle, thus taking into account time shifts due to the vessel elasticity. Peak-to-peak pressure differences can only be determined by means of catheterization or with the models described above when calibrated with catheterization data, which however invalidates the non-invasiveness of the estimation methods. For this reason, the present work focuses on instantaneous pressure differences instead of peak-to-peak values.

Based on Equation (3.4), the pressure Poisson equation (PPE) and the Stokes estimator (STE) method will be described next.

3.2.1 Poisson pressure equation (PPE)

Assuming sufficient regularity (i.e., assuming that all required derivatives exist), a Poisson equation for the pressure estimation can be obtained by taking the divergence of the time-discrete Navier–Stokes equation (3.2),

$$-\Delta \hat{p}^k = \nabla \cdot R^k. \tag{3.5}$$

Solving Equation (3.5) requires boundary conditions (BCs) on the boundary $\partial\Omega$ of the computational domain. A priori, no physical BCs for the pressure are known. An artificial Neumann BC can be obtained by projection of Equation (3.4), restricted to $\partial\Omega$, to the outward unit normal vector on the wall, $\boldsymbol{n}$,

$$\boldsymbol{n} \cdot \nabla \hat{p}^k = \boldsymbol{n} \cdot R^k. \tag{3.6}$$

Equation (3.5) with BCs (3.6) can be discretized in space and solved with the finite element, finite volume or finite difference methods. Independently on the spatial discretization, in order to ensure that the resulting algebraic problem is uniquely solvable, an option is to fix $\hat{p}^k = 0$ at one point via a Dirichlet boundary condition. This, indeed, does not change the pressure differences between two points in space.

3.2.2 Stokes estimator (STE)

The Stokes estimator introduces a divergence-free auxiliary function $\boldsymbol{w}$ with $\boldsymbol{w} = \boldsymbol{0}$ on $\partial\Omega$. The Laplacian of $\boldsymbol{w}$ is subtracted from Equation (3.4) as a regularization term (with unitary viscosity here for simplicity) and we obtain

$$\begin{aligned} -\Delta \boldsymbol{w} - \nabla \hat{p}^k &= R^k \quad \text{in } \Omega \\ \nabla \cdot \boldsymbol{w} &= 0 \quad \text{in } \Omega \\ \boldsymbol{w} &= \boldsymbol{0} \quad \text{on } \partial\Omega. \end{aligned} \tag{3.7}$$

The auxiliary function $\boldsymbol{w}$ holds no physical interest, and it is expected to be negligible compared to the pressure term as long as the right-hand-side R^k is the gradient of a scalar (irrotational). The advantages with respect to the PPE method are (1) that no artificial BCs for the pressure are necessary and (2) lower regularity requirements, since no additional derivatives are applied on the measurements R^k. In fact, in contrast to the PPE method, the STE method searches the pressure in the natural energy space of the pressure in the original Navier-Stokes equations. As for the PPE method, the pressure constant has to be fixed for ensuring solvability of the algebraic problem.

A variation of the STE method was presented in Bertoglio et al. [Ber+18b], where the convective term was written in 'energy-conserving' form, $(\boldsymbol{u}\cdot\nabla)\boldsymbol{u} + \frac{1}{2}(\nabla\cdot\boldsymbol{u})\boldsymbol{u}$, and improved results were obtained compared to the standard method. A third way of formulating the convection term is the divergence form $\nabla\cdot(\boldsymbol{u}\otimes\boldsymbol{u})$. In a preliminary study, the standard method, Eq. (3.3) (results not shown here), consistently delivered more accurate results than the other variants. Hence only results obtained using the standard STE formulation will be reported here.

3.3 Methods

3.3.1 Aortic Phantom Study

Phantom setup

The aortic phantom is fully described in Urbina et al. [Urb+16] and Montalba et al. [Mon+18]. It consists in a closed circuit which represents the thoracic aortic circulation, integrated by a MR compatible unit pump with a control unit (CardioFlow 5000 MR, Shelley Medical Imaging Technologies, London, Canada) and a realistic aortic model built with flexible silicone (T-S-N 005,

Elastrat, Geneva, Switzerland). Three nonreturn valves were installed to avoid negative pressures. Additionally, shutoff valves were added to regulate the flow distribution between the different vessels. Also a compliance chamber was installed after the descending aorta in order to simulate arterial compliance, to obtain physiologic diastolic pressures and physiologic pressure waveforms. The pump system is operated at 75 bpm to mimic rest conditions and at 136 bpm for stress conditions.

Different degrees of aortic coarctation were placed in the descending aorta just after the left subclavian artery. Aortic coarctations were built with Technyl with effective orifices of 9 mm, 11 mm and 13 mm and a length of 10 mm, leading to coarctation indices of 0.6, 0.5 and 0.4 respectively. The coarctation index was defined as the ratio between the CoA diameter and the diameter of the native DAo distal to the CoA. The liquid used in the system consisted of a blood mimicking fluid homemade with 60 % distilled water and 40 % glycerol (Orica Chemicals, Watkins, CO), with a density of 1.119 g/cm^3, viscosity of 4.83×10^{-3} Pa s, and a T1 value of 900 ms, which are representative values for human blood.

Catheterization

The phantom was equipped with a catheterization unit to measure invasively and simultaneously the pressure gradient across the coarctation. For this purpose, two catheters (5 French, Soft-Vu, AngioDynamics, Latham, NY) with transducers (AngioDynamics) were placed in the AAo and 2 cm after the CoA and were connected to a patient monitor (Contec Medical Systems, Hebei, China). The pressure catheters were zeroed at the same height of the phantom.

Pressure information from the two catheters was recorded simultaneously during 1 minute in the CoA phantoms (9 mm, 11 mm, 13 mm) at rest (75 bpm) and at stress conditions (136 bpm), using the commercial software Central Monitor System V3.0 (Contec Medical System). The pressure difference is obtained by subtracting both time series and averaging over the cardiac cycles.

4D flow data acquisition

Phantom data were acquired in a 1.5 T MRI system (Achieva, Philips, The Netherlands) using a 4-channel body coil and retrospective cardiac gating. The control unit of the pulsatile pump generated a trigger signal to synchronize the MR data acquisition. In order to provide static tissue for phase correction algorithms used in PC-MRI, 6 liters of 1 % agar were placed around the aortic phantom at least 6 hours before scanning.

4D flow images were acquired with an isotropic voxel size of 0.9 mm for all phantoms (CoA with 9 mm, 11 mm and 13 mm orifice diameter) under rest and stress conditions. The acquisition parameters are summarized in Table 3.3.1 (see column *in vitro*).

In order to study the effect of image resolution of the pressure gradient estimation procedure, different synthetic low resolution data (1.4 mm and 2.0 mm isotropic voxel) were generated from the original image (0.9 mm isotropic voxel) using linear interpolation.

3.3.2 Patient study: 4D-Flow MRI and catheterization

In addition to the phantom study, we include two subjects with aortic coarctation (*Subject 1*: 12 years, weight 47 kg, height 151 cm; *Subject 2*: 35 years, weight 63 kg, height 205 cm), who underwent combined MRI (4D Flow MRI) and cardiac catheterization investigations, in a 1.5T Achieva MR scanner and a BT Pulsera cardiac radiography unit (Philips, Best, Netherlands). The data was

Table 3.3.1: MR acquisition parameters

experiment	**in vitro**	**in vivo**
FOV (mm)	200 × 200 × 114	270 × 270 × 125
Matrix size	224 × 224 × 127	144 × 144 × 50
Recon. voxel (mm)	0.9 × 0.9 × 0.9	1.9 × 1.9 × 2.5
TFE factor	rest: 2, stress: 1	rest: 2
Cardiac phases	25	28
Time resolution (ms)	CoA: rest: 32, stress: 18 Normal: rest: 35, stress: 19	rest: 26
VENC (cm/s)	CoA: rest: 160–400, stress: 250–500 Normal: rest: 150, stress: 150	rest: 300
TE/TR (ms)	3.7/6.4	2.4/3.8
Flip angle (deg)	6.5	5
Scan time (min)	18–22	19

acquired at St. Thomas' Hospital, London, UK. The local research ethics committee approved this retrospective study and informed consent was obtained from all patients. Subject 1 presented a native aortic coarctation and mild aortic valve stenosis, mild left ventricular hypertrophy and systemic hypertension at rest. Subject 2 presented a repaired CoA using a subclavian flap, situs solitus, there was a very mild narrowing at the level of the transverse arch, close to the isthmus and a mild dilatation in the proximal descending aorta and also presented a gothic aortic arch. The acquisition parameters for the *in vivo* study are summarized in Table 3.3.1 (see column *in vivo*).

3.3.3 Segmentation and mesh generation

The 4D Flow MRI data sets were processed using an in-house MATLAB library (The MathWorks, Natick, MA), similarly to previous studies [Sot+16; Sot+18]. This process is illustrated in Figure 3.3.1 and consisted of the segmentation of the thoracic aorta using the anatomical image (Figure 3.3.1(a)) for the phantom data or the angiographic image proposed in Bock et al. [Boc+10] for patients. The value of the threshold is around 20 % of the maximum intensity of the image. After applying the threshold, we manually clean the vessel of interest, using labeling and manual delimitation tools of MATLAB. From the final segmented image, we generated a structured tetrahedral mesh (Figure 3.3.1(b)) such that its vertices matched the centers of the image voxels. Once the mesh was constructed, each velocity vector was transferred from the 4D flow MRI data to each node of the mesh (Figure 3.3.1(c)). The last step in the toolchain consists in the pressure map reconstruction (Figure 3.3.1(d)), described in the next section.

In order to study the effect of different segmentations on the pressure difference estimates, additional segmentations were created for the phantom velocity images at 0.9 mm voxel size. A reference segmentation was modified by adding or subtracting one voxel at the boundary, thus extending or decreasing the lumen cross-section.

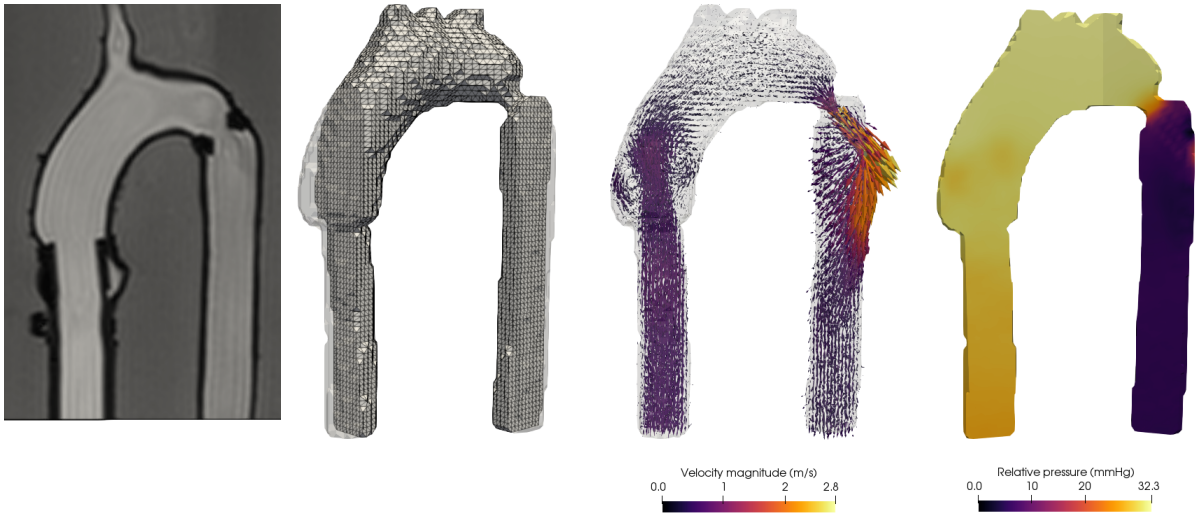

(a) Anatomical image (b) Mesh (c) Velocity vectors (d) Pressure

Figure 3.3.1: Pressure recovery toolchain. (a) 2D section from the anatomic image of 4D Flow MRI, (b) structured tetrahedral mesh from segmentation of the anatomical image, (c) representation of 4D flow velocity vectors on mesh, (d) pressure maps from velocity data (cuts though centers of AAo and DAo). Example data of the 9 mm CoA phantom at rest, at time of peak systole.

A preliminary study compared our structured meshing approach to generic tetrahedral meshes and found a significantly improved accuracy of the pressure estimation methods at similar mesh sizes. Here, only the results obtained with structured meshes are considered.

3.3.4 Pressure maps computation

Pressure maps are computed from all 4D flow data sets with the PPE and STE methods. The pressure differences, to be compared with the corresponding catheter values, are defined as differences of the pressure averages over two spheres with a radius of 4 mm at locations proximally and distally to the CoA (e.g., the blue and red spheres in Figure 3.4.1).

The corresponding partial differential equations of the PPE and STE methods are discretized with the finite element method (FEM). Velocity measurements are assumed to be piece-wise linear ($\mathbb{P}^1$) finite element functions on the tetrahedral meshes described in the previous section. Linear $\mathbb{P}^1$ elements are also used to discretize the PPE and the STE systems, Equations (3.5) and (3.7). In the latter case, standard pressure stabilization (Brezzi-Pitkaranta) is employed to ensure the solvability of the saddlepoint problem, avoiding the need of higher order elements. The resulting linear systems are solved efficiently with direct solvers. Example data is shown in Figure 3.3.1(d), as result of the last step of the pressure recovery toolchain, described in the previous section and illustrated in Figure 3.3.1. With the highest resolution of 0.9 mm, iterative solvers have to be used for the STE method due to memory requirements (on a 32 GB RAM workstation). We employ the GMRES method [Saa03] with a Schur complement based block preconditioner, using algebraic multigrid on the 'velocity' block and the diagonal of a pressure mass matrix for the Schur complement. The code was implemented using the python/C++ FEM library FEniCS [Aln+15] and iterative solvers from the scientific computation library PETSc [Bal+18]. The STE method requires longer computation times due to the larger number of unknowns and the more complex structure

of the discretization matrix.

The computation times of the PPE and the STE methods are compared in Table 3.3.2 for the 13 mm phantom using 25 cardiac phases at different resolutions using 1 or 4 cores of an Intel Xeon E5-1620 CPU. The iterative solvers employed for the STE method applied to the phantom data with a resolution of 0.9 mm result in a longer computation time.

Table 3.3.2: Computation times and numbers of unknowns of the 13 mm phantom at different resolutions with the PPE and the STE methods.

		PPE		STE	
# CPUs	resolution	# unknowns	time	# unknowns	time
1	2 mm	19597	5.2 s	78388	29.1 s
4	0.9 mm	240519	13.7 s	962076	702.0 s

3.4 Results

3.4.1 Phantom study

The streamlines of the 4D flow velocity field and the pressures measured by catheterization in the indicated locations are illustrated in Figure 3.4.1 for the 9 mm CoA phantom at peak systole. In addition, the instantaneous pressure difference resulting from subtracting both signals is plotted.

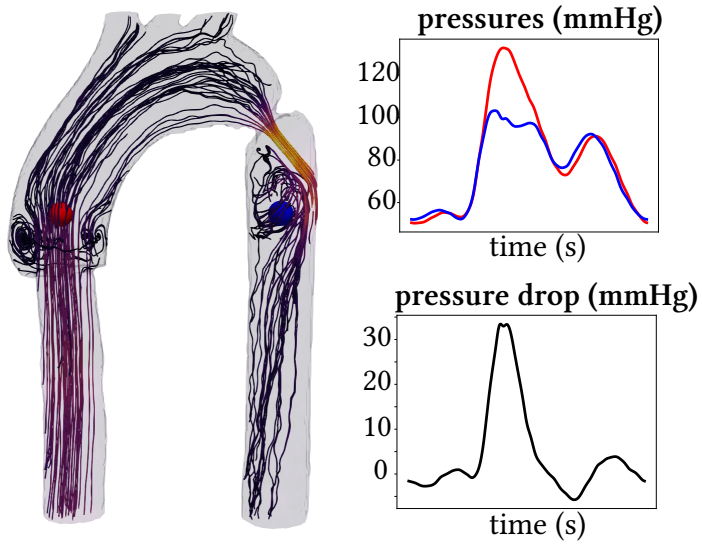

Figure 3.4.1: 9 mm phantom at rest. Velocity streamlines at peak systole, catheterization pressure signals, measured at blue and red dots, and resulting pressure differences.

Figure 3.4.2 compares the instantaneous peak pressure differences obtained with the PPE and the STE methods from 4D flow with catheterization data for all investigated phantoms. The figure shows the data obtained with the three image resolutions, 0.9 mm (panels (a) and (b)), 1.4 mm (panels (c) and (d)) and 2 mm (panels (e) and (f)) and using the three segmentations, denoted V+0

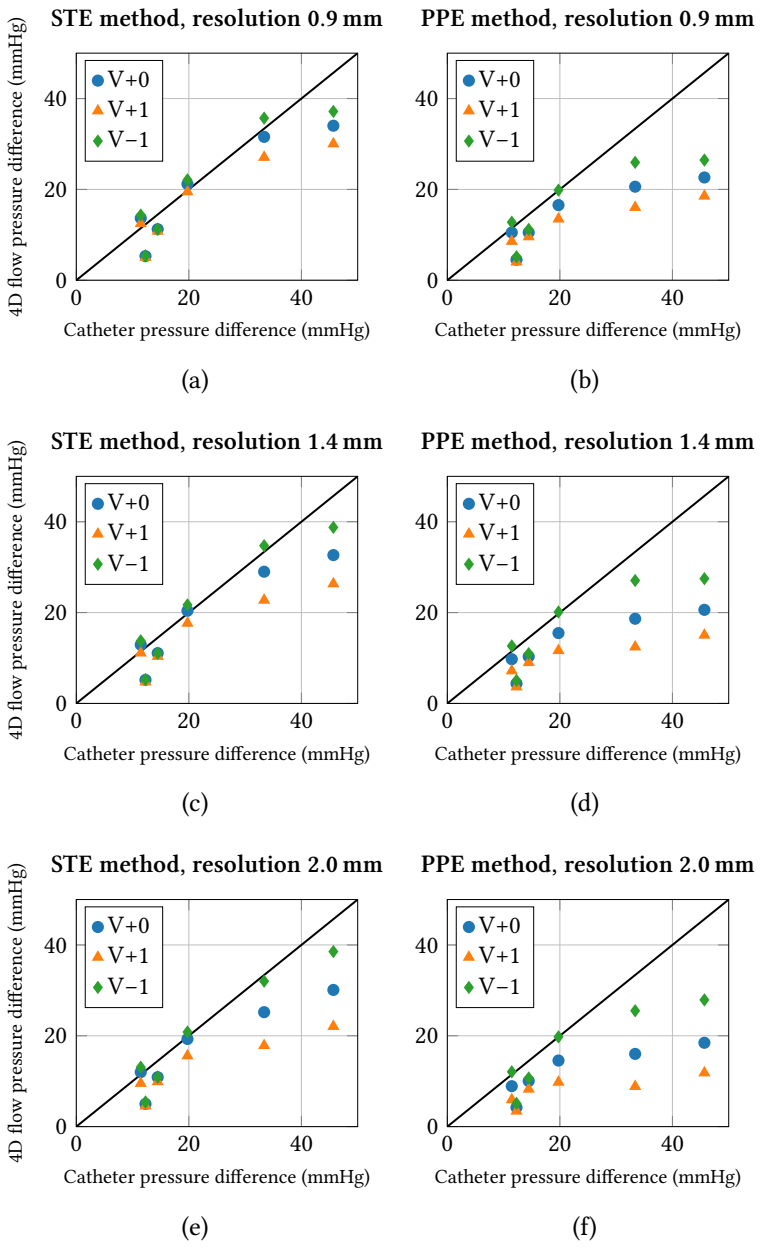

Figure 3.4.2: Comparison of 4D flow peak pressure differences obtained with the STE (left column) and the PPE (right column) methods with catheterization, using different image resolutions (0.9 mm, 1.4 mm and 2 mm) and segmentations (V+0: reference, V−1: outermost layer of voxels eliminated, V+1: 1 layer of voxels added at boundary; cf. text)

(neutral), V−1 (outermost layer of voxels eliminated along the boundary) and V+1 (1 layer of voxels added at the boundary).

Consider first the results obtained on the V+0 segmentation. The results show an overall good agreement between the STE peak pressure differences and the catheterization data. The STE underestimates the highest measured pressure difference (catheter pressure difference of 46 mmHg with the 9 mm CoA phantom under stress conditions). Another underestimation is visible at 12 mmHg in all plots, which was obtained for the 13 mm phantom at rest. The results appear to be robust to the image resolution. A strong dependence on the segmentation exists particularly for pressure differences above 30 mmHg and is more pronounced for large voxel sizes. The PPE method, in comparison, leads to a stronger underestimation than the STE method for pressure differences ≥20 mmHg. The PPE results are more sensitive to the image resolution.

In the presence of large pressure differences, both the PPE method and the STE method generally benefit from the narrowed segmentation (denoted V−1 in the figure). In the range of moderate pressure differences (e.g., 10–20 mmHg), the most accurate results with the STE method were obtained on the reference segmentation, while the V−1 segmentation led to a slight overestimation. The accuracy of the PPE method however was improved throughout the entire range of pressure differences. This is likely because of an increased sensitivity to boundary issues such as partial volume effects and low VNR (velocity-to-noise ratio) due to the artificial pressure boundary conditions. Choosing the segmentation too large resulted in underestimating the pressure differences (V+1 values in Figure 3.4.2).

The mean signed difference, as a measure of the bias, and the spread (two standard deviations) of the PPE and the STE methods with respect to catheterization data are compared for the three segmentations in Table 3.4.1. The data is shown for the acquired 4D flow images with a resolution of 0.9 mm. The bias and variability are smallest on the reduced segmentation V−1 and largest on

Table 3.4.1: Mean signed difference (bias) and spread (two standard deviations σ) for the PPE and the STE methods with respect to catheterization data, for the standard (V+0), the reduced lumen diameter segmentation (V−1), and the widened lumen diameter segmentation (V+1). 4D flow resolution: 0.9 mm

method	V+0 bias±2σ	V−1 bias±2σ	V+1 bias±2σ
PPE	−8.62 ± 14.97 mmHg	−5.94 ± 13.56 mmHg	−11.13 ± 17.01 mmHg
STE	−3.34 ± 9.61 mmHg	−1.85 ± 9.29 mmHg	−5.35 ± 10.94 mmHg

the extended segmentation V+1, with the reference segmentation V+0 ranking in between. The PPE method appears to be more sensitive to the segmentation. The STE method gives a smaller bias and variability than the PPE method on all three segmentations. In particular, the STE result on the standard segmentation appears to be more accurate than the PPE result obtained on the modified segmentation.

Time profiles of the pressure differences obtained with the V−1 segmentations of the phantom data with CoA are shown in Figures 3.4.3–3.4.5. Each figure contains the results of the PPE and the STE methods for 4D flow image resolutions of 0.9 mm (acquired) and 1.4 mm, 2.0 mm (subsampled from 0.9 mm) under rest and stress conditions and the pressure difference from catheter

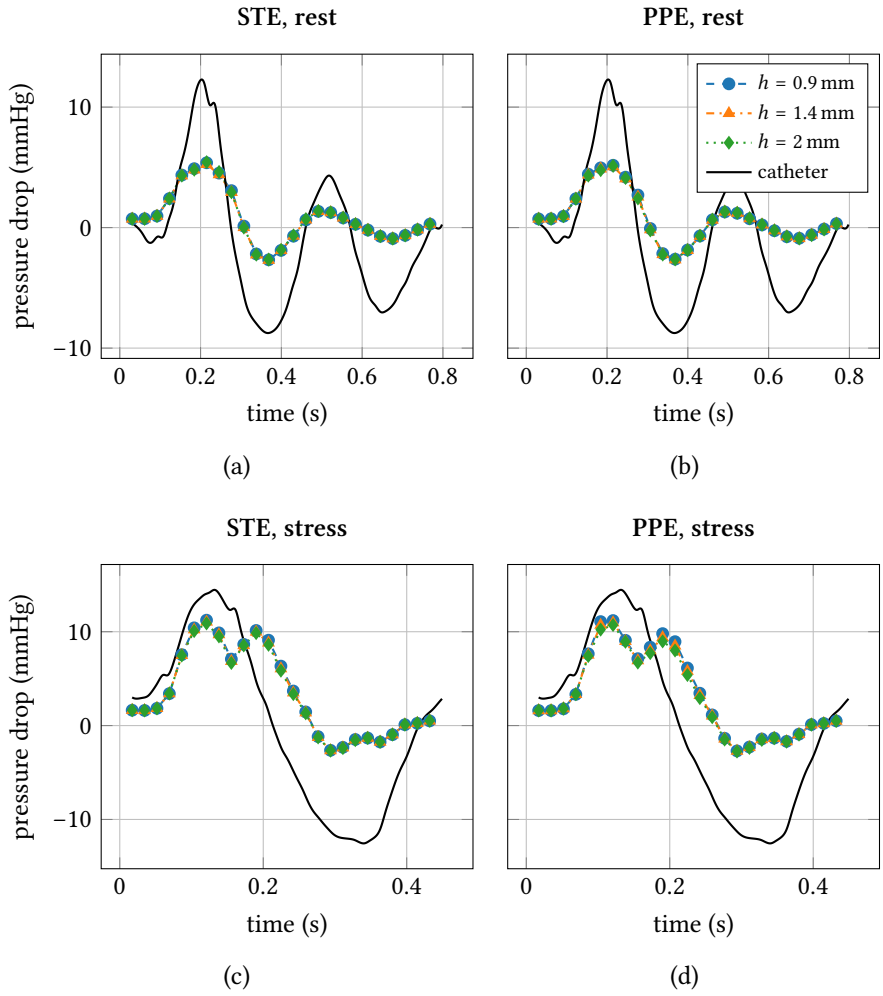

Figure 3.4.3: 13 mm CoA phantom pressure differences obtained with STE (left column) and PPE (right column) under rest (first row) and stress conditions (second row) using voxel sizes of 0.9 mm, 1.4 mm, 2.0 mm compared to ground truth catheter data.

measurements. For postprocessing reasons, the catheter curves were shifted in time such that the location of the peaks matched the 4D flow data.

The results of the 13 mm CoA phantom study are displayed in Figure 3.4.3. While showing qualitatively a correct behavior, the amplitude of the oscillation is generally underestimated by 3 to 7 mmHg with both methods under rest conditions. The effect of the image resolution is hardly noticeable (although slightly larger with the PPE method). Under stress conditions, the peak pressure difference is recovered with a good accuracy. There is a negative pressure difference peak that was not correctly recovered by any of both methods. It has to be noted that in the particular case of the 13 mm CoA phantom, artifacts appeared in the velocity measurements, most likely connected to issues with the experimental setup, like bubbles. The 13 mm CoA phantom configuration was repeatedly scanned at different resolutions (results not reported) and the corresponding estimated pressure differences showed similar characteristics in all cases.

In the case of the 11 mm CoA phantom, the PPE method exhibits a very good quantitative agreement with the catheter results under rest conditions during the complete heart cycle (Figure 3.4.4(b)). In comparison, the STE method overestimates the peak pressure difference. The

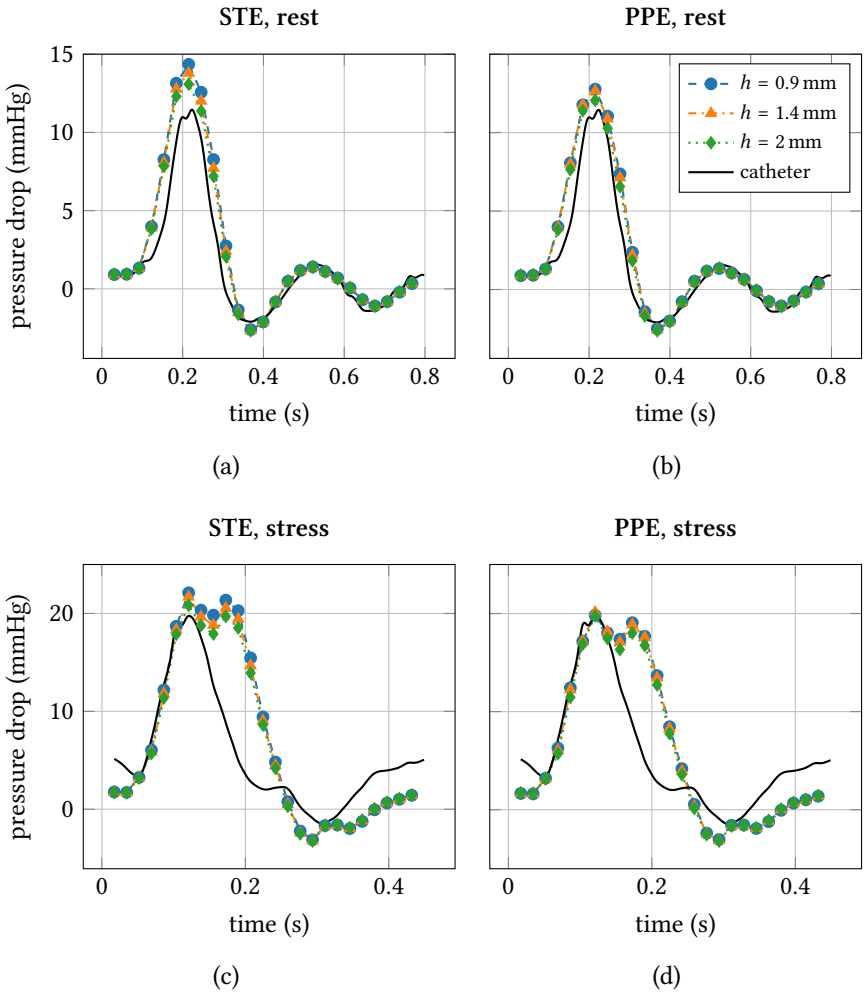

Figure 3.4.4: 11 mm CoA phantom pressure differences obtained with STE (left column) and PPE (right column) under rest (first row) and stress conditions (second row) using voxel sizes of 0.9 mm, 1.4 mm, 2.0 mm compared to ground truth catheter data.

STE result is improved by using the standard segmentation instead of the narrowed segmentation. Under stress conditions, the width of the pressure differences maxima was overestimated with both the STE and the PPE methods.

Results from the 9 mm CoA phantom under rest conditions showed an excellent agreement between the catheter data and the pressure difference computed with the STE method (Figure 3.4.5, panel (a)). The PPE method strongly underestimates the pressure difference under equal conditions (panel (b)). The discrepancy between the pressure difference reconstruction and catheter measurements increases for stress conditions, the STE method still showing more accurate results than the PPE method. Both methods are very robust with respect to the image resolution. Using the narrowed segmentation, the results of the stress case are slightly improved by the lower resolutions. With low resolution data, effectively more boundary data is discarded by deleting the outermost voxel layer. This indicates that the errors introduced by considering boundary data predominate the effect of image resolution in this scenario. In contrast, in Figure 3.4.2 the V+0 pressure differences at 46 mmHg decrease with lower image resolutions.

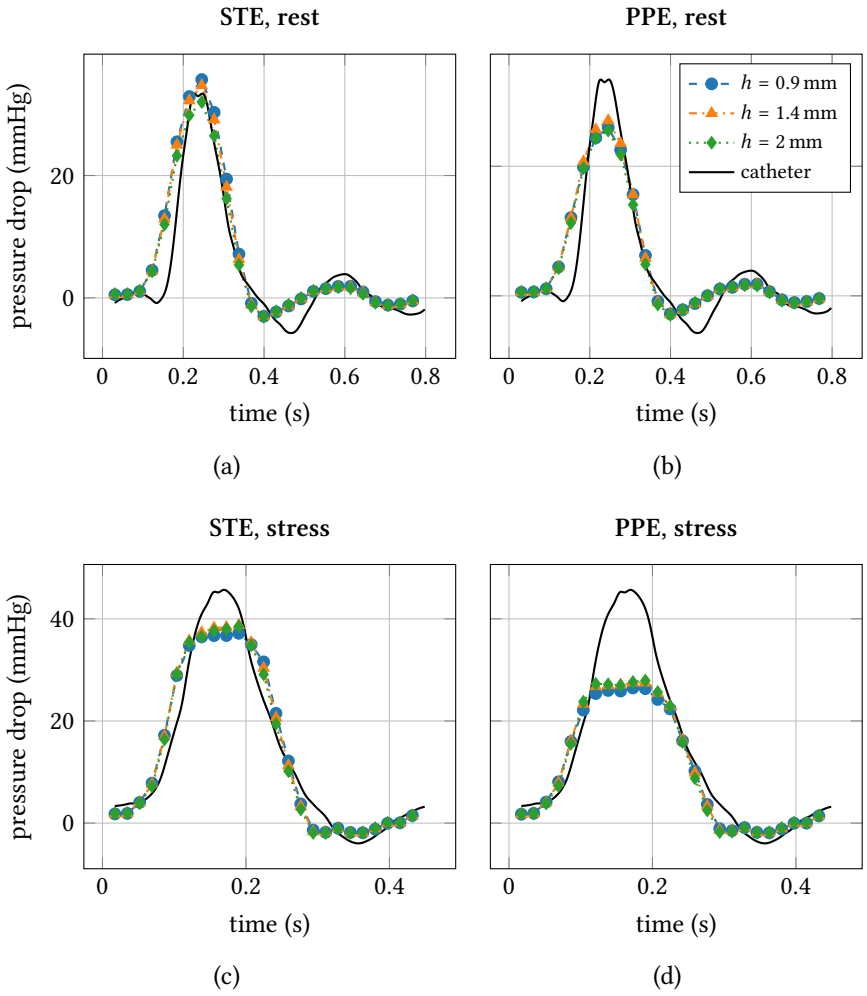

Figure 3.4.5: 9 mm CoA phantom pressure differences obtained with STE (left column) and PPE (right column) under rest (first row) and stress conditions (second row) using voxel sizes of 0.9 mm, 1.4 mm, 2.0 mm compared to ground truth catheter data.

3.4.2 Patient data

Pressure differences obtained by catheterization and from 4D flow are shown in Figure 3.4.6 for both patients. The pressure difference computed with the STE method for subject 1 shows excellent agreement with the catheter data during systole, underestimating the local extrema after $t = 0.4$ s. While similar qualitative agreement was found with the PPE method, it significantly underestimates the pressure difference during systole. Subject 2 exhibits excellent qualitative and quantitative agreement between catheter data and numerical pressure difference reconstruction. However, the pressure difference peak observed by catheterization is too steep to be captured by the time resolution of the 4D flow protocol. The resulting maximum value lies below the catheter value, possibly because no velocity image was recorded coinciding exactly with the maximum pressure difference.

Note that the lengths of the cardiac cycles differ significantly between catheterization and MRI scans of both patients. This indicates a change in the heart rate and hence, the hemodynamics in the cardiovascular system, and can explain the differences between 4D flow and catheter pressure

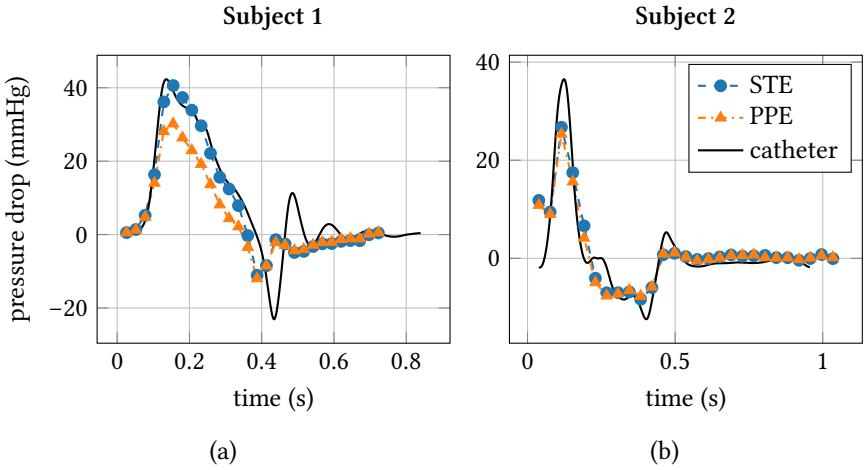

Figure 3.4.6: Patient data results, comparison of STE and PPE pressure differences with catheter data

differences.

Reducing the diameter of the segmentation by one voxel was not possible in one of the patients due to the large voxel size with respect to the diameter. The original segmentations were thus not modified.

3.5 Discussion

This study compared two relative pressure reconstruction methods, STE and PPE, in terms of accuracy and sensitivity with respect to image resolution and to segmentation. The main finding of this study is that the STE method applied to real data is more accurate than the classical PPE method at large pressure differences (>20 mmHg). The difference between the methods is less pronounced for small to moderate pressure gradients. The PPE method showed overall a higher sensitivity to data perturbations, i.e., to image resolution and segmentation. Both the STE and the PPE methods proved most sensitive to the image resolution and the segmentation in the most severe cases of 9 mm and 11 mm CoA during systole. Especially the PPE results were greatly improved by eliminating the outermost layer of voxels from the segmentation, leading to a more accurate match with the catheter data than STE in the 11 mm CoA phantom. However, the STE method gave excellent results in this case using the standard segmentation. A reduction of the segmentation was used before in Goubergrits et al. [Gou+19] and also led to an improved accuracy of the PPE method. The accuracy improvement can be explained by the reduction of partial volume effects and eliminating low VNR data near the boundaries. The PPE method is likely to be more sensitive to the boundary data than the STE method due to the artificial pressure boundary conditions used in the PPE. The issues of boundary data, possible remedies and the effect of somewhat arbitrarily reducing the diameter of the vessel geometry deserve a more in-depth analysis in future studies.

Our results on the standard segmentation (V+0) are coherent with Goubergrits et al. [Gou+19] and Nasiraei-Moghaddam et al. [Nas+04], who also demonstrated that the pressure profile is degraded when the spatial resolution is decreased. In [Gou+19], minimal resolution requirements were determined for the PPE, namely 5 voxels/diameter. In our study, when the narrowed seg-

mentation was used (V−1, between 2 and 12 voxels/diameter for the CoA phantoms), the results were almost insensitive to the image resolution. It is possible that the benefit of removing problematic boundary data at low resolutions, apparently increasing under low resolutions, balances with the detriment of a decreased image resolution in the interior.

An advantage of the STE method is that it avoids unphysical boundary conditions. However, using standard discretization methods, parts of the term R^k in Equation (3.7) can contribute to the auxiliary function—not always negligible in practice—instead of the pressure gradient. This occurs principally where large gradients are present in the velocity field, for instance in the coarctation near the arterial walls, and can result in stronger underestimations of the relative pressure. We hypothesize that, by choosing a more narrow segmentation with the arterial wall located inside the flow, the homogeneous Dirichlet boundary condition for the auxiliary velocity in the STE on the smaller domain results in a smaller auxiliary velocity everywhere and therefore in increased pressure gradient estimates with respect to the full geometry for severe CoA. Pressure-robust FEM could counteract this issue [LM16] and generally improve the accuracy of the STE method.

Dilated segmentations (V+1) add no-flow voxels with very small VNR, hence introducing spurious information into the estimation problem. The pressure gradient computed with any method is required to accommodate to the unphysical conditions.

For severe conditions of CoA, i.e., in the presence of high velocity jets and high Reynolds numbers, the STE method was clearly superior to the PPE method. In such severe cases of CoA, turbulence can develop [Ku97; Dyv+06] and involves dynamics at scales smaller than the spatial and/or temporal image resolution. Such effects are not accounted for by the models studied here, and are likely to reduce the precision especially in the 9 mm phantom under stress conditions. Furthermore, higher velocities require higher VENC values (500 cm/s for the 9 mm phantom at stress) resulting in lower VNR, possibly affecting the estimation. Our study did not include sensitivity to noise. However, we can consider the results present here as a "worst case scenario" in terms of noise due to the small voxel size of 0.9 mm, hence involving a much worse VNR than what can be expected for typical voxel size in patients (i.e., around 2 mm). This issue could be alleviated by using the dual-VENC techniques [Net+12; Ha+16a; Cal+16; Car+18], allowing for lower VENC-values (hence lower noise), but at increased scan times.

The STE and the PPE pressure reconstruction methods were also applied to real patient data. For one of the patients, the STE method showed a great improvement over the PPE method. Both methods showed satisfactory results for the second patient. From the findings in the phantom experiments, the differences between PPE and STE in patient one is most likely due to strong convective effects.

One limitation of the study was the lack of availability of real low resolution MRI data for all scenarios, hence requiring synthetic subsampling of the high resolution data. In addition, the comparison of catheter data with MRI scans is limited by the following observations. The locations where the catheter recorded the pressure during catheterization are only known approximately. Fluctuations in the flow can also perturb the catheter position. A mismatch of the catheter positions with the locations selected for evaluating the computed pressure gradient can introduce additional errors. Finally, representing an invasive technique, it is possible that the presence of the catheter in the vessel disturbs and alters the aortic flow during catheterization, while the 4D flow data was acquired without the catheters. In the patient study it was seen that the heart rate changed significantly between catheterization and the MRI scan, hence possibly also affecting the outcome of this comparison.

In conclusion, in our phantom study, the STE method delivered results that were more accurate

and robust with respect to resolution and segmentation than the PPE method, in particular in severe cases of CoA. For cases of mild CoA or no CoA, the advantage of the STE method was negligible. By eliminating the outermost layer of voxels of the segmentation, the PPE method could be significantly improved to match the accuracy of the STE method, except for very large pressure gradients.

Chapter 4

Multiscale Modeling of Vascular Trees

The present chapter is a short adaption of the article C. Bertoglio, C. Conca, D. Nolte, G. Panasenko, and K. Pileckas. "Junction of Models of Different Dimension for Flows in Tube Structures by Womersley-Type Interface Conditions". In: *SIAM Journal on Applied Mathematics* 79.3 (Jan. 2019), pp. 959–985. DOI: 10.1137/18M1229572.

4.1 Introduction

The vasculature is a complex tree-like network of vessels. Computing the blood flow in such networks requires a lot of computational resources. Different approaches exist for reducing the complexity of vascular flow computations [FQV09b; PV09]. In general, one seeks to avoid solving the 3D Navier–Stokes equations (which in addition might be coupled with the solid mechanics of the vessel walls, tracer transport, turbulence) in parts of the domain, where simplifying assumptions can be made for the flow profile and/or the geometry. The full flow model is resolved where a detailed analysis of the flow field is of interest or cannot be neglected or simplified. This would be typically the case in large vessels with curvature or obstructions, junctions and other situations of circulating or separating flow. Reduced models can be derived in many different ways. For instance, by assuming a simplified symmetric shape of the vessels such as thin cylinders, the flow equations can be integrated over the vessel cross section, resulting, e.g., in simplified PDEs and a reduced geometric dimension (e.g., one-dimensional (1D)). 1D models can also be obtained by means of asymptotic analysis invoking the assumption that the radius is much smaller than the length of the vessel [Bar+66]. Considering thin, compliant vessels, 1D models can also be derived from conservation principles, using different assumptions on the geometry and the physics [HL73; PV09; BFU07; Bla+09]. Often, the vasculature is modeled by a '0D' lumped parameter network, where the flow through the vessels (and even organs) is described as electric networks in terms of resistances, capacities and inductances [PV09; BCF13; Vig+10]. 0D models can be derived either by averaging 1D or 3D models or from conversation laws [PV09].

Geometric multiscale modeling is concerned with coupling models of different dimensions. Multiscale models can couple a 3D Navier–Stokes system in a part of a large vessel where the flow is expected to exhibit strong 3D features with a 1D model describing the flow in smaller peripheral vessels, or with a 0D model providing boundary conditions for the truncated part of the vasculature, or both [FQV09b; BFU07; Urq+06]. Usually, the domain is first decomposed, then the model is reduced within the separate subdomains, finally the resulting models of different orders are coupled. Such multiscale models result in coupled systems which can be difficult to

solve numerically. Often, the compartments with different models are separated and solved for with an iteration scheme. Questions of well-posedness and stability arise.

In this work, to simplify its complex structure, the vascular network is modeled as thin tube structures. Tube structures are domains which are tree-like sets of thin cylinders (or thin rectangles in the two-dimensional setting). The ratio of the diameters of cylinders to their heights (or ratio of the sides of rectangles) is a small parameter ε. The method of asymptotic partial decomposition of a domain (MAPDD) allows to reduce essentially the computer resources needed for the numerical solution of such problems [Ber+19]. This new method combines the full-dimensional description in some neighborhoods of bifurcations and a reduced-dimensional description of the connecting tubes, prescribing some special junction conditions at the interfaces between these 3D and 1D submodels (see Blanc et al. [Bla+99], Panasenko [Pan98a], Panasenko [Pan98c], and Panasenko and Pileckas [PP15]). With the approach presented here, the reduced-order compartments enter directly the full-dimensional model. In contrast to the 'reduce first, then couple' approach outlined above, here the subdomains remain fully coupled and are reduced in order subsequently ('couple first, then reduce'). As a consequence, the complete multiscale model can be solved efficiently at once, nested iteration schemes and difficult to solve, coupled systems of different order ODEs/DAEs can be avoided. Furthermore, well-posedness and error estimates are covered by the theory. On the other hand, the approach is so far limited to rigid tubes.

Junction conditions for the steady-state Stokes equations and generalizations to the unsteady Navier–Stokes equations were constructed in Bertoglio et al. [Ber+19]. In the present chapter the theoretical results are summarized, the numerical implementation is discussed and a validation study for a 2D test case is presented.

First, in Section 4.2, the full dimensional flow problems will be introduced, followed by a description of the MAPDD model and a summary of the theoretical results in Section 4.3. The focus of this chapter is the confirmation of the theoretical error estimates by means of numerical examples in Section 4.4.

4.2 The full dimensional fluid flow problem in a tube structure

In this section we will introduce the full dimensional fluid flow problem in a tube structure. Further its solution will be approximated using partial dimension reduction.

4.2.1 Thin tube structure domain

Let us remind the definition of a thin tube structure [Pan98b; Pan05; PP15], and graphically exemplified in Figure 4.2.1.

Let $O_1, O_2, \dots, O_N$ be N different points in $\mathbb{R}^n$, $n = 2, 3$, and $e_1, e_2, \dots, e_M$ be M closed segments each connecting two of these points (i.e. each $e_j = \overline{O_{i_j} O_{k_j}}$, where $i_j, k_j \in \{1, \dots, N\}$, $i_j \neq k_j$). All points O_i are supposed to be the ends of some segments e_j. The segments e_j are called edges of the graph. The points O_i are called nodes. Any two edges e_j and e_i, $i \neq j$, can intersect only at the common node. A node is called vertex if it is an end point of only one edge. Assume that the set of vertices is $O_{N_1+1}, O_{N_1+2}, \dots, O_N$, where $N_1 < N$. Denote $\mathscr{B} = \bigcup_{j=1}^{M} e_j$ the union of edges, and assume that $\mathscr{B}$ is a connected set. The graph $\mathscr{G}$ is defined as the collection of nodes and edges. Let e be some edge, $e = \overline{O_i O_j}$. Consider two Cartesian coordinate systems in $\mathbb{R}^n$. The first one

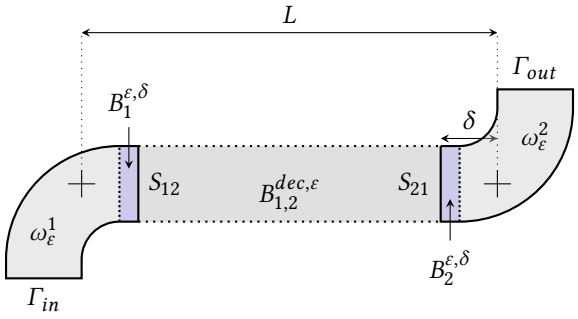

Figure 4.2.1: Illustration of the computational domain for $N = 2$ and $M = 1$.

has the origin in O_i and the axis $O_i x_1^{(e)}$ has the direction of the ray $[O_i O_j)$; the second one has the origin in O_j and the opposite direction, i.e., $O_j \tilde{x}_1^{(e)}$ is directed over the ray $[O_j O_i)$. With every edge e_j we associate a bounded domain $\sigma_j \subset \mathbb{R}^{n-1}$ having a C^2-smooth boundary $\partial\sigma^j$, $j = 1, \dots, M$. For every edge $e_j = e$ and associated $\sigma_j = \sigma^{(e)}$ we denote by $B_\varepsilon^{(e)}$ the cylinder

$$B_\varepsilon^{(e)} = \{x^{(e)} \in \mathbb{R}^n \,:\, x_1^{(e)} \in (0,\, |e|),\ \frac{x^{(e)\prime}}{\varepsilon} \in \sigma^{(e)}\},$$

where $x^{(e)\prime} = (x_2^{(e)}, \dots, x_n^{(e)})$, $|e|$ is the length of the edge e and $\varepsilon > 0$ is a small parameter. Notice that the edges e_j and Cartesian coordinates of nodes and vertices O_j, as well as the domains σ_j, do not depend on ε. Denoting $\sigma_\varepsilon^{(e)} = \{x^{(e)\prime} \in \mathbb{R}^{n-1} \,:\, \frac{x^{(e)\prime}}{\varepsilon} \in \sigma^{(e)}\}$ we can write $B_\varepsilon^{(e)} = (0, |e|) \times \sigma_\varepsilon^{(e)}$. Let $\omega^1, \dots, \omega^N$ be bounded independent of ε domains in $\mathbb{R}^n$ with Lipschitz boundaries $\partial\omega^j$; introduce the nodal domains $\omega_\varepsilon^j = \{x \in \mathbb{R}^n \,:\, \frac{x - O_j}{\varepsilon} \in \omega^j\}$. Denote $d = \max_{1 \le j \le N} \operatorname{diam} \omega^j$. By a tube structure we call the following domain

$$B_\varepsilon = \Big(\bigcup_{j=1}^{M} B_\varepsilon^{(e_j)} \Big) \bigcup \Big(\bigcup_{j=1}^{N} \omega_\varepsilon^j \Big).$$

So, the tube structure B_ε is a union of all thin cylinders having edges as the heights plus small smoothing domains ω_ε^j in the neighborhoods of the nodes. Their role is to avoid artificial corners in the boundary of intersecting cylinders, and we will assume that B_ε is a bounded domain (connected open set) with a C^2-smooth boundary. However for the numerical tests we consider a domain with corners.

4.2.2 The full dimension fluid flow problem

Let us consider the stationary Stokes or the non-stationary Navier–Stokes equations in B_ε with the no-slip conditions at the boundary ∂B_ε except for some parts γ_ε^j of the boundary where the velocity field is given as known inflows and outflows (for alternative boundary conditions on the inlet and outlet boundaries of the domain, the reader is referred to Bègue et al. [Bèg+87] and Bertoglio et al. [Ber+18a]).

The inflow and outflow boundaries are denoted $\gamma_\varepsilon^j = \partial\omega_\varepsilon^j \cap \partial B_\varepsilon$, $\gamma^j = \partial\omega^j \cap \partial B_1^j$ where $B_1^j = \{y \,:\, y\varepsilon + O_j \in B_\varepsilon\}$ and $\gamma_\varepsilon = \cup_{j=N_1+1}^{N} \gamma_\varepsilon^j$.

Unsteady Navier–Stokes Problem

The initial boundary value problem for the non-stationary Navier–Stokes equations reads

$$\begin{aligned} \boldsymbol{u}_{\varepsilon,t} + (\boldsymbol{u}_\varepsilon \cdot \nabla)\boldsymbol{u}_\varepsilon - \nu\Delta\boldsymbol{u}_\varepsilon + \nabla p_\varepsilon &= 0, \\ \nabla \cdot \boldsymbol{u}_\varepsilon &= 0, \\ \boldsymbol{u}_\varepsilon\big|_{\partial B_\varepsilon} &= \boldsymbol{g}_\varepsilon, \\ \boldsymbol{u}_\varepsilon(x,0) &= 0, \end{aligned} \tag{4.1}$$

where $\boldsymbol{u}_\varepsilon$ is the unknown velocity vector, p_ε is the unknown pressure, $\boldsymbol{g}_\varepsilon$ is a given vector-valued function with $\boldsymbol{g}_\varepsilon(x,t) = \boldsymbol{g}_j(\frac{x - O_j}{\varepsilon}, t)$ if $x \in \gamma_\varepsilon^j$, $j = N_1 + 1, \dots, N$ and equal to zero for the remaining part of the boundary $\partial B_\varepsilon \backslash \gamma_\varepsilon$ and satisfying the additional conditions given in Bertoglio et al. [Ber+19].

Introduce the space $\boldsymbol{H}^1_{div0(\partial B_\varepsilon\backslash\gamma_\varepsilon)}(B_\varepsilon)$ as the subspace of vector valued functions from $\boldsymbol{H}^1(B_\varepsilon)$ satisfying the conditions $\nabla \cdot \boldsymbol{v} = 0$, $\boldsymbol{v}|_{\partial B_\varepsilon \backslash \gamma_\varepsilon} = 0$, i.e.,

$$\boldsymbol{H}^1_{div0(\partial B_\varepsilon\backslash\gamma_\varepsilon)}(B_\varepsilon) = \left\{ \boldsymbol{v} \in \boldsymbol{H}^1(B_\varepsilon) |\ \nabla \cdot \boldsymbol{v} = 0;\ \boldsymbol{v}|_{\partial B_\varepsilon\backslash\gamma_\varepsilon} = 0 \right\}.$$

We consider as well the smaller subspace $\boldsymbol{H}^1_{div0}(B_\varepsilon) = \boldsymbol{H}^1_{div0(\partial B_\varepsilon\backslash\gamma_\varepsilon)}(B_\varepsilon) \cap \boldsymbol{H}^1_0(B_\varepsilon)$ of divergence free vector-valued functions vanishing at the whole boundary.

A weak formulation corresponding to the Navier–Stokes problem (4.1) is given by the following definition.

Definition 1. *By a weak solution we understand the couple of the vector-field $\boldsymbol{u}_\varepsilon$ and a scalar function p_ε such that $\boldsymbol{u}_\varepsilon(x,0) = 0$, $\boldsymbol{u}_\varepsilon \in L^2(0,T;\boldsymbol{H}^1_{div0(\partial B_\varepsilon\backslash\gamma_\varepsilon)}(B_\varepsilon))$, $\boldsymbol{u}_{\varepsilon,t} \in L^2(0,T;\boldsymbol{L}^2(B_\varepsilon))$, $p_\varepsilon \in L^2(0,T;L^2(B_\varepsilon))$, $\boldsymbol{u}_\varepsilon = \boldsymbol{g}_\varepsilon$ on γ_ε and $(\boldsymbol{u}_\varepsilon, p_\varepsilon)$ satisfy the integral identity for every vector-field $\boldsymbol{\phi} \in \boldsymbol{H}^1_0(B_\varepsilon)$ for all $t \in (0,T)$,*

$$\int_{B_\varepsilon} \left(\boldsymbol{u}_{\varepsilon,t} \cdot \boldsymbol{\phi} + \nu \nabla \boldsymbol{u}_\varepsilon \,:\, \nabla\boldsymbol{\phi} + ((\boldsymbol{u}_\varepsilon, \nabla)\boldsymbol{u}_\varepsilon) \cdot \boldsymbol{\phi}) \right) = \int_{B_\varepsilon} p_\varepsilon \nabla \cdot \boldsymbol{\phi}.$$

Stokes problem

Consider the Dirichlet's boundary value problem for the stationary Stokes equation:

$$\begin{aligned} -\nu\Delta\boldsymbol{u}_\varepsilon + \nabla p_\varepsilon &= 0,\ x \in B_\varepsilon, \\ \nabla \cdot \boldsymbol{u}_\varepsilon &= 0,\ x \in B_\varepsilon, \\ \boldsymbol{u}_\varepsilon &= \boldsymbol{g}_\varepsilon,\ x \in \partial(B_\varepsilon), \end{aligned} \tag{4.2}$$

where ν is a positive constant, $\boldsymbol{g}_\varepsilon$ is a given vector-valued function $\boldsymbol{g}_\varepsilon(x) = \boldsymbol{g}_j(\frac{x - O_j}{\varepsilon})$ if $x \in \gamma_\varepsilon^j$, $j = N_1 + 1, \dots, N$, equal to zero for the remaining part of the boundary $\partial B_\varepsilon \backslash \gamma_\varepsilon$ and satisfying the additional conditions in Bertoglio et al. [Ber+19].

A weak formulation of the Stokes problem (4.2) is given by the following definition:

Definition 2. *By a weak solution we understand the couple of the vector-field* $\boldsymbol{u}_\varepsilon$ *and a scalar function* p_ε *such that* $\boldsymbol{u}_\varepsilon \in \boldsymbol{H}^1_{div0(\partial B_\varepsilon \setminus \gamma_\varepsilon)}(B_\varepsilon)$, $p_\varepsilon \in L^2(B_\varepsilon)$, $\boldsymbol{u}_\varepsilon = \boldsymbol{g}_\varepsilon$ *on* γ_ε *and* $(\boldsymbol{u}_\varepsilon, p_\varepsilon)$ *satisfy the integral identity: for any test function* $\boldsymbol{v} \in \boldsymbol{H}^1_0(B_\varepsilon)$

$$\nu \int_{B_\varepsilon} \nabla \boldsymbol{u}_\varepsilon(x) \,:\, \nabla \boldsymbol{v}(x) = \int_{B_\varepsilon} p_\varepsilon \nabla \cdot \boldsymbol{\phi}.$$

It is well known that there exists a unique solution to this problem (see [Lad69]).

4.3 MAPDD: the new junction conditions

The classical MAPDD method was previously described in Panasenko and Pileckas [PP15]. We propose a new, more general, formulation of the method involving new junction conditions, which assumes that the flow through the cylinders $B^{(e)}_\varepsilon$ has the shape of a Womersley flow. The advantages are twofold: (1) it removes a restriction on the velocity boundary condition (see Bertoglio et al. [Ber+19]), therefore being applicable for arbitrary transient regimes, and (2) it considerably simplifies the numerical implementation in the context of finite elements since only additional, easy-to-build integral terms need to be added to a standard weak form.

4.3.1 Formulation

Let δ be a small positive number much greater than ε but much smaller than 1. For any edge $e = \overline{O_i O_j}$ of the graph introduce two hyperplanes orthogonal to this edge and crossing it at the distance δ from its ends, see Figure 4.2.1.

Denote the cross-sections of the cylinder $B^{(e)}_\varepsilon$ by these two hyperplanes respectively, by S_{ij} (the cross-section at the distance δ from O_i), and S_{ji} (the cross-section at the distance δ from O_j), and denote the part of the cylinder between these two cross-sections by $B^{dec,\varepsilon}_{ij}$. Denote $B^{\varepsilon,\delta}_i$ the connected truncated by the cross sections S_{ij}, part of B_ε containing the vertex or the node O_i.

The MAPDD model invokes the assumption of Womersley-type flow conditions within each of the truncated cylinders $B^{dec,\varepsilon}_{ij}$, namely

- the velocity is parallel to the edge e, i.e., the perpendicular (tangential to S_{ij}) components are zero,
- the longitudinal derivative (normal to S_{ij}) of the velocity is zero (i.e., identical velocity profiles at every cross-section of the cylinders $B^{dec,\varepsilon}_{ij}$),
- implying a constant longitudinal pressure derivative.

In particular, if the local variables $x^{(e)}$ for the edge e coincide with the global ones, x, then the Womersley flow profile takes the form $\boldsymbol{W}^{(e)}_P(x) = (v_1(x'/\varepsilon), 0, \dots, 0)^T$, $v_1 \in H^1_0(\sigma^{(e)})$. If e has the direction cosines $k_{e1}, \dots, k_{en}$ and the local variables $x^{(e)}$ are related to the global ones by equation $x^{(e)} = x^{(e)}(x)$ then the Womersley flow is given by

$$\boldsymbol{W}^{(e)}_P(x) = \text{const} \left(k_{e1} v_1 \left(\left(x^{(e)}(x) \right)' / \varepsilon \right), \dots, k_{en} v_1 \left(\left(x^{(e)}(x) \right)' / \varepsilon \right) \right)^T, \; x' = (x_2, \dots, x_n).$$

Consider the Navier–Stokes problem, and furthermore the special case of geometries with $N = M + 1$, which leads to the following formulation:

find the vector-field $\boldsymbol{u}_{\varepsilon,\delta}$ and the pressure $p_{\varepsilon,\delta}$ such that $\boldsymbol{u}_{\varepsilon,\delta}(x,0) = 0$, $\boldsymbol{u}_{\varepsilon,\delta} \in L^\infty(0,T;\boldsymbol{H}^1(B_i^{\varepsilon,\delta}))$, for all $i = 1,\dots,N$, $\boldsymbol{u}_{\varepsilon,\delta,t} \in L^2(0,T;\boldsymbol{L}^2(B_i^{\varepsilon,\delta}))$, $\boldsymbol{u}_{\varepsilon,\delta} = \boldsymbol{g}_\varepsilon$ at γ_ε, $\boldsymbol{u}_{\varepsilon,\delta} = \boldsymbol{0}$ at $(\partial B_i^{\varepsilon,\delta} \cap \partial B_\varepsilon)\backslash\gamma_\varepsilon$, $p_{\varepsilon,\delta} \in L^2(0,T;L^2(B_i^{\varepsilon,\delta}))$ for all $i = 1,\dots,N$, $\boldsymbol{u}_{\varepsilon,\delta}\cdot\boldsymbol{t} = 0$ on $S_{ij}\cup S_{ji}$, $\boldsymbol{u}_{\varepsilon,\delta}\cdot\boldsymbol{n}\big|_{S_{ij}} + \boldsymbol{u}_{\varepsilon,\delta}\cdot\boldsymbol{n}\big|_{S_{ji}} = 0$, where $\boldsymbol{t}$ is the unit tangent vector and $\boldsymbol{n}$ the unit outward normal vector, and the couple $(\boldsymbol{u}_{\varepsilon,\delta}, p_{\varepsilon,\delta})$ satisfies for all $t \in (0,T)$ the integral identity for every vector-field $\boldsymbol{\phi} \in \boldsymbol{H}^1(B_i^{\varepsilon,\delta})$, $q \in L^2(B_i^{\varepsilon,\delta})$, for all $i = 1,\dots,N$, such that $\boldsymbol{\phi} = 0$ at $\partial B_i^{\varepsilon,\delta} \cap \partial B_\varepsilon$, and for all edges O_iO_j, $\boldsymbol{\phi}\cdot\boldsymbol{t} = 0$ at $S_{ij}\cup S_{ji}$ and $\boldsymbol{\phi}\cdot\boldsymbol{n}|_{S_{ij}} + \boldsymbol{\phi}\cdot\boldsymbol{n}|_{S_{ji}} = 0$:

$$\begin{aligned}\sum_{i=1}^{N}\int_{B_i^{\varepsilon,\delta}} \boldsymbol{u}_{\varepsilon,\delta,t}\cdot\boldsymbol{\phi} + \nu\nabla\boldsymbol{u}_{\varepsilon,\delta} \,:\, \nabla\boldsymbol{\phi} + (\boldsymbol{u}_{\varepsilon,\delta},\nabla\boldsymbol{u}_{\varepsilon,\delta})\cdot\boldsymbol{\phi} - p_{\varepsilon,\delta}\nabla\cdot\boldsymbol{\phi} + q\nabla\cdot\boldsymbol{u}_{\varepsilon,\delta} \\ + \sum_{l=1}^{M} d_l\int_{\sigma_\varepsilon^{(e_l)}} \boldsymbol{u}_{\varepsilon,\delta,t}\cdot\boldsymbol{\phi} + \nu\nabla_{x^{(e_l),'}}\boldsymbol{u}_{\varepsilon,\delta} \,:\, \nabla_{x^{(e_l),'}}\boldsymbol{\phi} = 0.\end{aligned} \tag{4.3}$$

For $e_l = \overline{O_iO_j}$, d_l is the distance between the cross sections S_{ij} and S_{ji}.

The last sum of integrals in Eq. (4.3) is the contribution of the truncated tubes to the full-dimensional model describing the junctions. They enter the equation by substitution of the boundary integrals arising from integrating by parts the diffusion term. See Bertoglio et al. [Ber+19, Appendix A.3] for a complete derivation.

Finally, note that the last two terms in (4.3) are analogous to the ones obtained in the context the so called *Stokes-consistent* methods for backflow stabilization at open boundaries [BC16].

4.3.2 Error estimate for the unsteady Navier–Stokes problem

The following estimate for the error of the MAPDD solution of the Navier–Stokes problem with respect to the exact solution can be obtained (see Bertoglio et al. [Ber+19]):

Theorem 1. *Let $\boldsymbol{g}_j \in C^{[\frac{J+4}{2}]+1}([0,T];W^{3/2,2}(\partial\omega_j))$. Given natural number J there exists a constant C (independent of ε and J) such that if $\delta = CJ\varepsilon|\ln\varepsilon|$, then*

$$\sup_{t\in(0,T)} \|\boldsymbol{u}_{\varepsilon,\delta} - \boldsymbol{u}_\varepsilon\|_{\boldsymbol{L}^2(B_\varepsilon)} + \|\nabla(\boldsymbol{u}_{\varepsilon,\delta} - \boldsymbol{u}_\varepsilon)\|_{L^2((0,T);\boldsymbol{L}^2(B_\varepsilon))} = O(\varepsilon^J) \ . \tag{4.4}$$

4.3.3 Error estimate for the stationary Stokes problem

Applying the MAPDD method in a similar manner to the Stokes problem, the following error estimate can be proved with asymptotic analysis for the difference between the exact solution, $\boldsymbol{u}_\varepsilon$, and the MAPDD solution, $\boldsymbol{u}_{\varepsilon,\delta}$:

Theorem 2. *Given natural number J there exists a constant C (independent of ε and J) such that if $\delta = CJ\varepsilon|\ln\varepsilon|$, then*

$$\|\boldsymbol{u}_\varepsilon - \boldsymbol{u}_{\varepsilon,\delta}\|_{\boldsymbol{H}^1(B_\varepsilon)} = O(\varepsilon^J). \tag{4.5}$$

See Bertoglio et al. [Ber+19] for the full derivation and proofs.

4.4 Numerical examples

In this section, the previous analysis is complemented by numerical experiments for the new MAPDD formulation applied to the stationary Stokes problem and the transient Navier–Stokes problem, for a sequence of values of ε. In the tests we used more natural Neumann's condition for the outflow. The errors of the MAPDD solutions obtained in the truncated domain with respect to reference solutions computed in the full domain are evaluated in the norms given by Eqs. (4.4) and (4.5).

4.4.1 Problem setup

Consider the two-dimensional geometry illustrated in Fig. 4.2.1. Two junctions are connected by a straight tube. This straight tube (labeled $B_{1,2}^{dec,\varepsilon}$) is included in the full reference model, or truncated when the reduced MAPDD model is used.

The radius of the tube is proportional to ε (we set $R = \varepsilon$). For each value of ε, the junction domains are contracted homothetically by a factor of ε with respect to the center points marked with plus signs in Fig. 4.2.1. The distance between these points, L, remains the same for all values of ε. Straight tube extensions (blue areas, $B_{1;2}^{\varepsilon,\delta}$) are added to the junction domains. Theorem 2 requires the associated distance, δ, from the centers of the junction domains to the interfaces, to be

$$\delta = C\varepsilon|\ln(\varepsilon)|. \tag{4.6}$$

C is a user parameter. Pairs of full and reduced domains are created for a sequence of values $\varepsilon = 2^{-k}$, $k = 1, \dots, 6$. In the particular examples of the investigated geometry and our selection of ε, $1/\ln(2) < C < 6/\ln(2)$ is necessary for $B_{1;2}^{\varepsilon,\delta} \neq \emptyset$ and for $B_{1,2}^{dec,\varepsilon} \neq \emptyset$, respectively. In what follows, we choose the values $C = K/\ln(2)$, $K = 2, 3$ and 4. The factor $1/\ln(2)$ is added for convenience, to cancel with the $\ln(\varepsilon)$ terms and leave rational numbers as the interface coordinates.

4.4.2 Stationary Stokes test case

Since one of our main motivations is the numerical simulation of blood flows, we choose for the viscosity and the density values that represent physiologically relevant conditions, assuming the fluid is incompressible and Newtonian. Typical parameters of blood are a dynamic viscosity of $\mu = 0.035\,\mathrm{cm}^2/\mathrm{s}$ and a density of $\rho = 1\,\mathrm{g/cm}^3$. Remind the relation between the dynamic viscosity μ and the kinematic viscosity ν: $\nu = \mu/\rho$. At the inlet Γ_{in} of the upstream junction domain a Dirichlet boundary condition for the velocity is defined as $\mathbf{g}_\varepsilon = \left(0,\ 1.5U_0(1 - (x_1 - c_0)^2/\varepsilon^2)\right)^T$, where c_0 is the x_1 coordinate of the center of the boundary and U_0 is chosen such that $Re = 2\rho\varepsilon U_0/\mu = 1$. A homogeneous Neumann boundary condition for the normal stress is applied on the outlet Γ_{out} of the downstream junction domain.

4.4.3 Transient Navier–Stokes test case

In the transient Navier–Stokes test case, the physical constants are set to the same values as for the Stokes problem, i.e., $\mu = 0.035\,\mathrm{cm}^2/\mathrm{s}$ and $\rho = 1\,\mathrm{g/cm}^3$. A pulsating inflow velocity is defined on Γ_{in} via Dirichlet boundary conditions as $\mathbf{g}_\varepsilon = \left(0,\ 1.5U_0(1 - (x_1 - c_0)^2/\varepsilon^2)\sin(\pi t/T)\right)^T$, where t is the actual time and $T = 0.8\,\mathrm{s}$ is the duration of a cycle. U_0 is computed from the Reynolds

number, $Re = 2\rho\varepsilon U_0/\mu$. As for the Stokes problem, a homogeneous Neumann boundary condition defines the outflow on Γ_{out}. For the convergence study, Reynolds numbers $Re = 1$, 25, 50, 80 and 100 are considered. In addition, we analyze the MAPDD model for a high Reynolds number of $Re = 2500$.

4.4.4 Numerical discretization

A mixed finite element method is adopted for discretizing the Stokes and Navier–Stokes equations. We use monolithic velocity–pressure coupling with inf-sup stable second order Taylor-Hood elements on unstructured, uniform triangle meshes. The transient Navier–Stokes problem is discretized in time with the implicit Euler method. The convection term, written in skew-symmetric form, is treated semi-implicitly. The time step size is $\Delta t = 0.01$ s. The time interval of the simulations is a half cycle, i.e., $0 \le t \le T/2$. The numerical meshes of the domains are created such that the number of elements along the tube diameter is approximately 20 for each value of ε. The average grid size at the boundaries is therefore $h = \varepsilon/10$. This results in 170592 elements in the full domain for the smallest value of $\varepsilon = 2^{-6}$ and $C = 2/\ln(2)$, which corresponds to 784037 degrees of freedom in the Navier–Stokes system. The triangulation of the corresponding reduced domain consists of 15366 elements and the solution space contains 70741 degrees of freedoms. The problem is implemented and solved using the FEniCS finite element library [Aln+15]. The numerical meshes are generated with Gmsh [GR09].

4.4.5 Results

Stationary Stokes test case

The velocity and pressure field of the stationary Stokes problem, computed with the full model and with the MAPDD method, are illustrated in Fig. 4.4.1 for the largest value of $\varepsilon = 0.5$. No visible differences exist between the full and the MAPDD results.

The velocity error of the MAPDD model with respect to the full reference solution is analyzed quantitatively in Fig. 4.4.2 for the full range of values of ε. The error is computed in the $\boldsymbol{H}^1(B_\varepsilon)$ norm, cf. (4.5) in Theorem 2. Note that the error estimate depends on the solutions in the full domain, B_ε. The mesh nodes of the MAPDD and the full domains match for the junctions. In the truncated tube, the MAPDD solution was interpolated from one of the interfaces, S_{12}, to the mesh nodes of the full mesh. The rate of convergence can be estimated from the numerical results as

$$J_k = \frac{\log e_k/e_{k-1}}{\log \varepsilon_k/\varepsilon_{k-1}}$$

where $e_k = \|\boldsymbol{u}_{\varepsilon_k} - \boldsymbol{u}_{\varepsilon_k,\delta}\|_{\boldsymbol{H}^1(B_{\varepsilon_k})}$, $\varepsilon_k = 2^{-k}$, $k = 2, \dots, 6$. While not constant, for $C = 2/\ln(2)$, J_k is in the range $3 \lesssim J_k \lesssim$. The error drops at least with cubic convergence (in the investigated cases). For $C = 3/\ln(2)$ the convergence rate is greatly improved, and even more so using $C = 4/\ln(2)$, namely we obtain $J \approx 8$ and $J \approx 11$, respectively, discarding the points where the error stagnates. The stagnation of both cases for $\varepsilon < 2^{-4}$ or 2^{-3} is due to the precision of the numerical method being reached. Rounding errors gain importance for very small values of ε.

Transient Navier–Stokes test case

The asymptotic behavior of the error of the MAPDD method with respect to the full model is shown for different Reynolds numbers in Fig. 4.4.3(a), for $C = 2/\ln(2)$. The error is evaluated

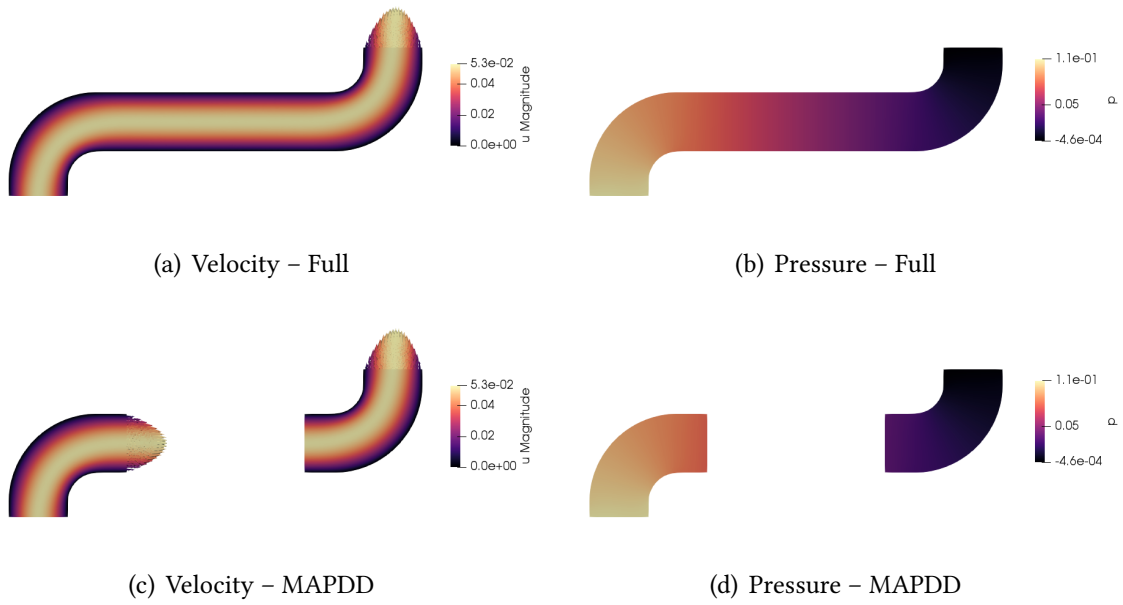

(a) Velocity – Full

(b) Pressure – Full

(c) Velocity – MAPDD

(d) Pressure – MAPDD

Figure 4.4.1: Pressure fields and velocity magnitude and vectors at the outflow boundaries obtained for the stationary Stokes problem using $\varepsilon = 0.5$ with the full model (top row) and with the MAPDD model (bottom row).

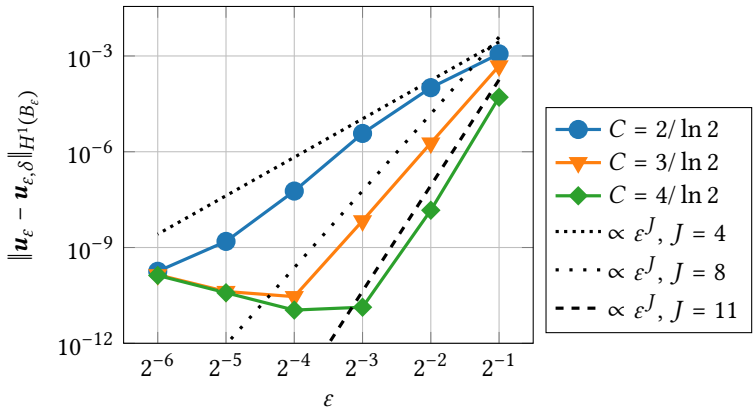

Figure 4.4.2: Stationary Stokes test case: convergence of the error with respect to ε for different values of C (see legend).

in the norm (4.4). For the lowest investigated Reynolds number $Re = 1$, the rate of convergence J was computed (omitting the two largest values of ε). The line ε^J is included in the figure for comparison. With increasing Reynolds numbers the rate of convergence decreases. Exponential increase of the error was observed for $Re = 100$. Using $C = 3/\ln(2)$ (see Fig. 4.4.3(b)), the rate of convergence obtained for Reynolds numbers $Re > 1$ is improved. In particular, for $Re = 100$ the error now decreases with ε, at least for small values of ε. The errors of the case $Re = 100$ obtained for $C = K/\ln(2)$, $K = 2, 3, 4$, are shown in Fig. 4.4.4. Indeed, for higher K, the errors are lower and convergence is improved for $\varepsilon \lesssim 2^{-4}$. While the error estimate assumes a low Reynolds number, the MAPDD method can still be applied to these cases. Figures 4.4.5 and 4.4.6 show velocity streamlines and the pressure field obtained with the full reference model and the

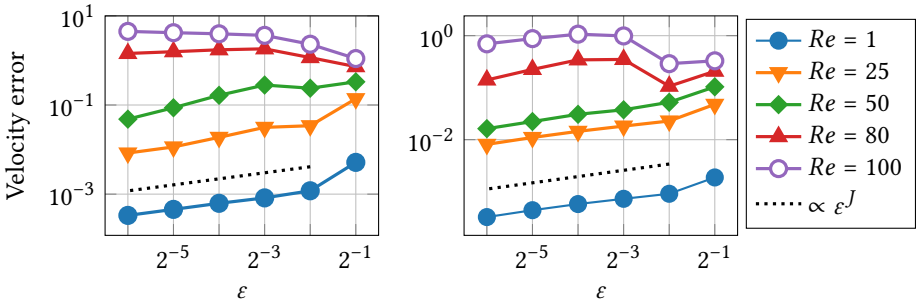

(a) $C = 2/\ln(2)$, $J = 0.45$ (b) $C = 3/\ln(2)$, $J = 0.4$

Figure 4.4.3: Errors (Eq. (4.4)) of the Navier–Stokes MAPDD model w.r.t. to the full solution for different Reynolds numbers for different values of C.

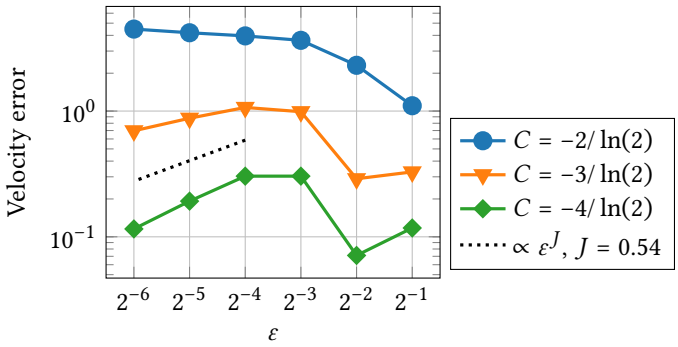

Figure 4.4.4: Comparison of the Navier–Stokes error with different values of C for $Re = 100$.

MAPDD method applied to the case $\varepsilon = 1/4$ and for a Reynolds number of $Re = 2500$, as an example. The boundary mesh size was set to $h = \varepsilon/20$, furthermore $C = 2/\ln(2)$. The results match very well visually. The MAPDD model is able to recover the recirculation zones in both junctions accurately (Fig. 4.4.5(a) and (b)). For a more detailed comparison, the axial velocity profiles at the interfaces for the MAPDD solution and for the full solution in the corresponding location are shown in Figs. 4.4.7. At the left interface, the velocity interface conditions produce a pressure overshoot near the upper corner, since the Womersley hypothesis is in disagreement with the high Reynolds number flow conditions. This can be seen more clearly in Fig. 4.4.8(a), where the pressure profile at the interface is shown for both the MAPDD and the full solution. However, analyzing the pressure distribution along the cross-section the tube in a slightly more upstream position (shifted upstream by 2ε), the MAPDD recovers the behavior observed for the full solution with an error of $< 8\,\%$ (Fig. 4.4.9). The pressure on the right interface does not suffer any nonphysical oscillations, as can be seen in Fig. 4.4.8(b), and the discrepancy between both models is within $2\,\%$.

4.5 Conclusion

The MAPDD was shown to be an efficient and accurate method for the steady Stokes problem and for the low Reynolds number Navier–Stokes problem. In these cases, the error of the MAPDD method was in agreement with theoretical error estimates, (4.5) and (4.4), respectively. For slightly

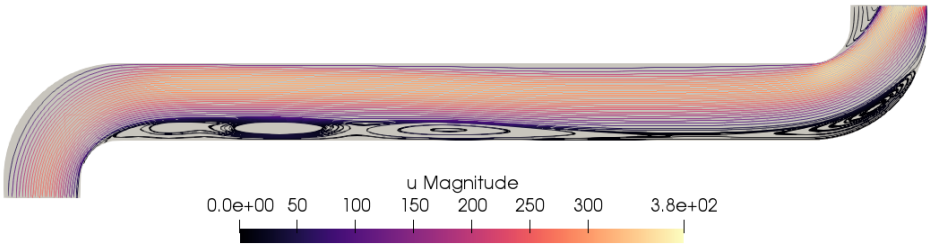

(a) Velocity – Full order solution

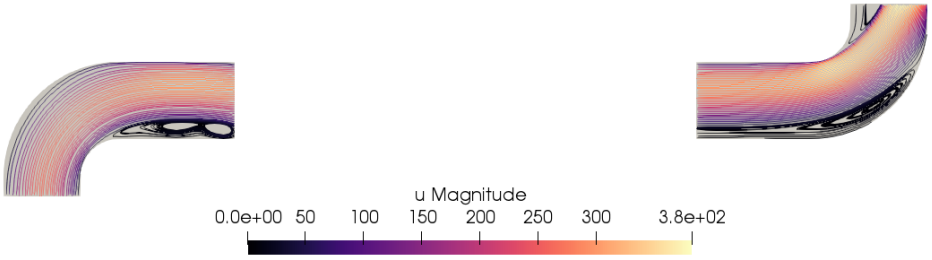

(b) Velocity – MAPDD solution

Figure 4.4.5: Velocity stream lines of the transient Navier–Stokes test case at peak time $t = 0.2$ s, for $Re = 2500$, $\varepsilon = 0.25$. Full model (a) versus MAPDD model (b).

larger Reynolds numbers, the convergence can be improved by modifying the computational domain and adjusting the constant in Eq. (4.6). Although the theory is only valid for small Reynolds numbers, the method yields very good results also for high Reynolds numbers. For the (arbitrary) example of $Re = 2500$, $\varepsilon = 1/4$, the MAPDD velocity and pressure solutions were in good agreement with the full solution, except for pressure oscillations that occur near the upstream interface.

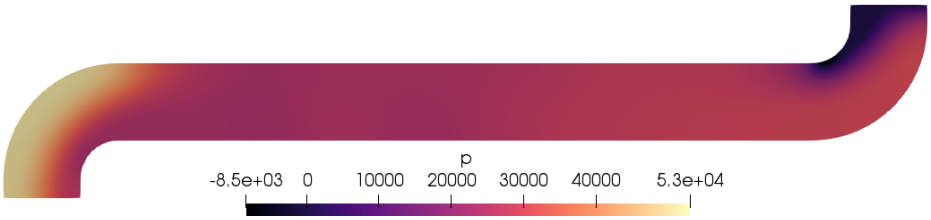

(a) Pressure – Full

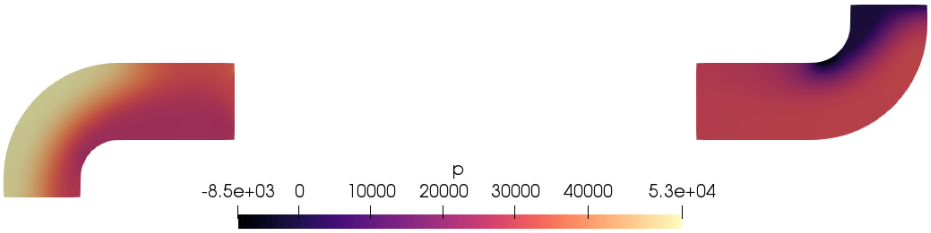

(b) Pressure – MAPDD

Figure 4.4.6: Pressure fields of the transient Navier–Stokes test case at peak time $t = 0.2$ s, for $Re = 2500$, $\varepsilon = 0.25$. Full model (a) versus MAPDD model (b).

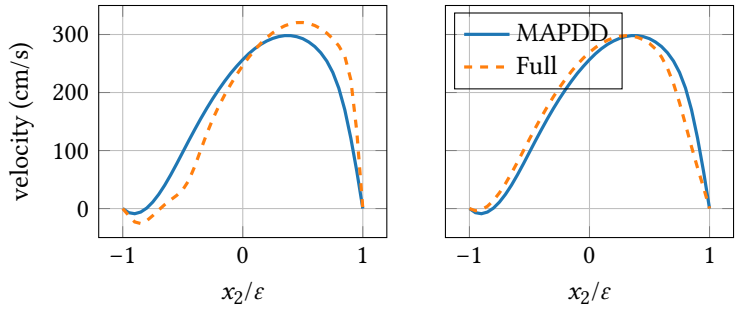

(a) left interface S_{12} (b) right interface S_{21}

Figure 4.4.7: Axial velocity component u_0 at the interfaces for the MAPDD and the full solutions computed for $Re = 2500$, $\varepsilon = 1/4$.

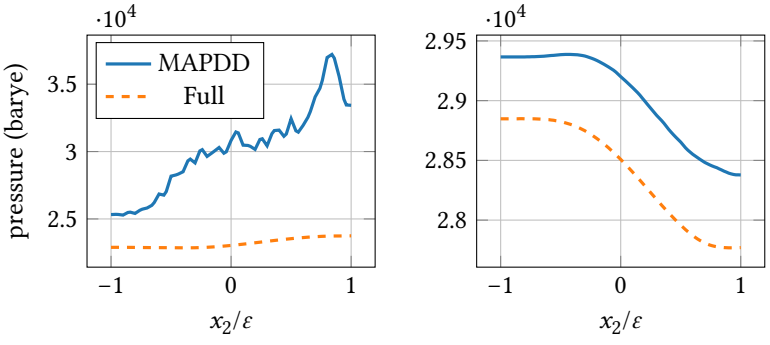

(a) left interface S_{12} (b) right interface S_{21}

Figure 4.4.8: Pressure along the interfaces for the MAPDD and the full solutions computed for $Re = 2500$, $\varepsilon = 1/4$.

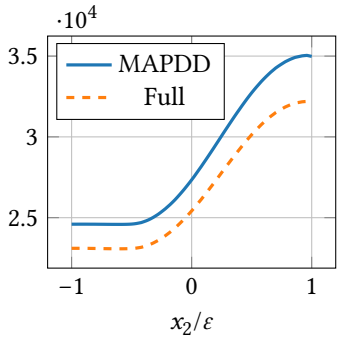

Figure 4.4.9: Pressure along the tube cross-section, at 2ε upstream of S_{12}, for the MAPDD and the full solutions computed for $Re = 2500$, $\varepsilon = 1/4$.

Chapter 5

Conclusion

5.1 Summary

For the diagnosis, treatment planning and post-surgical monitoring of cardiovascular disease (CVD), hemodynamic markers have proven to be of great utility. However, non-invasive assessment of the hemodynamics of a patient is still a challenge. Phase-contrast magnetic resonance imaging (PC-MRI) can measure the distribution of blood velocity along two-dimensional planes or in three-dimensional volumes and is limited in accuracy mainly by the image resolution and noise. The local variation in the blood pressure cannot be measured non-invasively, but is required in the clinical practice to evaluate CVD. Other hemodynamic quantities, such as the arterial wall stiffness or wall shear stress can also be relevant as diagnostic quantities and for understanding the onset of CVD, but are not observable with imaging techniques.

This thesis approaches the topic of patient-specific hemodynamics on three different paths.

In Chapter 2 of this thesis a method was presented to improve the accuracy of hemodynamic data recovery from partial 2D PC-MRI measurements by means of solving an inverse problem of the Navier–Stokes equations of fluid flow. Vessel geometries extracted from MRI or CT images are affected by errors due to noise, artifacts and limited image resolution. Small errors in the geometry propagate into the recovered data and lead to large errors in the solution when standard no-slip boundary conditions are used on inaccurately positioned walls. The core idea of this work was replacing no-slip boundary conditions at the arterial walls by slip/transpiration conditions with parameters which were estimated from velocity measurements. Numerical results of synthetic test cases showed an important improvement in accuracy of the estimated pressure differences and the reconstructed velocity fields.

In Chapter 3 a comparison study of different direct pressure gradient estimation techniques was presented. These methods compute relative pressure fields directly from 3D PC-MRI data. The new Stokes estimation method (STE) by Švihlová et al. [Švi+16] was applied for the first time to real phantom and patient data. In comparison to the classical Poisson pressure estimation method (PPE), the STE method proved more accurate and more robust to noise and the image segmentation in most cases.

Chapter 4 was dedicated to a numerical validation of the new MAPDD model [Ber+19] for a domain decomposition reduction of vascular networks. This approach considers the vessels as a network of thin pipes in which the flow has the shape of a Womersley flow, connected by arbitrary 3D junction domains where the flow is governed by the Navier–Stokes equations. In the MAPDD model, the thin pipes are replaced by coupling conditions on the junction domains. A strategy

to easily implement the MAPDD model with the finite element method was presented and the theoretical results of Bertoglio et al. [Ber+19] were reproduced with numerical simulations in a simple test case. The method was shown to deliver accurate results even for moderately large Reynolds numbers, far from the regime where the theory is valid.

5.2 Perspectives

As was shown in Chapter 3, the investigated direct pressure estimation methods are sensitive to the image segmentation and to the image resolution, especially for high Reynolds numbers. The methodology presented in Chapter 2 using slip/transpiration boundary conditions aims specifically at an improved robustness with respect to errors in the computational domain. Future work should therefore apply the discussed slip/transpiration data assimilation framework to the phantom data of Chapter 3. It is hypothesized that pressure estimates using the data assimilation method are more accurate and less sensitive with respect to the image segmentation and resolution than the PPE and the STE methods. The aortic phantom and realistic aorta geometries in general require handling multiple outlets. Outflow boundary conditions based on the MAPDD method discussed in Chapter 4 can be used to model the effect of the truncated parts of the vasculature. To that end, the MAPDD junction conditions have to be applied to the corresponding boundaries and the parameter describing the length of the truncated pipe, d_l in Eq. (4.3), has to be estimated with the parameter estimation formalism. The small bifurcating vessels in the aortic arch justify the assumption of a Womersley flow made by the MAPDD model. Such a boundary condition is a simpler alternative to Windkessel boundary conditions in terms of modelling complexity, implementation and computational effort when solving the system. Only one parameter per boundary is required and the model is entirely local. The MAPDD junction conditions are guaranteed to be stable with respect to backflow. The accuracy of the model needs to be studied carefully for the proposed application. In addition to 3D PC-MRI data, the data assimilation method can also be applied to 2D measurements. Minimum data requirements should be identified for the data assimilation method.

Turbulence was seen to deteriorate the accuracy of direct pressure estimators in Chapter 3. The Navier–Stokes solver used in the data assimilation framework can be extended in straight forward manner to include turbulence models, such as large eddy simulation [Pop00]. It is expected that the precision of the data assimilation framework applied to real data of cases of CoA, in particular to the 9 mm and 11 mm CoA phantoms under stress conditions, can be improved by considering turbulence. Future work should examine this hypothesis for clinically relevant cases and determine if the increased demand in computational resources is justified.

One of the limitations of the study presented in Chapter 2 was that the coefficients of the slip/transpiration boundary conditions were assumed constant in space and time. It is expected that the accuracy of the method can be improved by considering a spatial and temporal distribution of the parameters. Future studies should analyze different approaches, such as spatially parameterizing the coefficients, e.g., with respect to the center line. Time-dependence could be implemented, for instance, by considering a sum of shape functions (e.g., sines) with coefficients to be estimated in the parameter estimation framework.

The elasticity of the arterial walls plays an important role in the arterial hemodynamics and should be taken into account in many cases for reliable hemodynamic simulations [NOV11]. A worthwhile path for future work could be exploring the estimation of mechanical wall properties from velocity measurements (instead of displacements [BMG12; Ber+14]) using data assimilation

and a fluid–structure interaction (FSI) model [FQV09a; SY16]. If the slip/transpiration model can be reasonably applied to FSI or should be viewed as an alternative approach is not clear at this stage. This question should be discussed in the future.

Bibliography

[Aln+15] M. Alnæs et al. “The FEniCS Project Version 1.5”. In: *Archive of Numerical Software* 3.100 (2015). DOI: 10.11588/ans.2015.100.20553.

[Bal+18] S. Balay et al. *PETSc Users Manual*. ANL-95/11 - Revision 3.10. Argonne National Laboratory, 2018.

[Bar+11] A. Baretta et al. “Virtual Surgeries in Patients with Congenital Heart Disease: A Multi-Scale Modelling Test Case”. In: *Philosophical Transactions of the Royal Society A: Mathematical, Physical and Engineering Sciences* (Nov. 13, 2011).

[Bar+66] A. C. L. Barnard et al. “A Theory of Fluid Flow in Compliant Tubes”. In: *Biophysical journal* 6.6 (1966), pp. 717–724.

[Bas07] O. K. Baskurt, ed. *Handbook of Hemorheology and Hemodynamics*. Biomedical and Health Research v. 69. OCLC: ocn183145995. Amsterdam ; Washington, DC: IOS Press, 2007. 455 pp.

[Bau+09] H. Baumgartner et al. “Echocardiographic Assessment of Valve Stenosis: EAE/ASE Recommendations for Clinical Practice”. In: *Journal of the American Society of Echocardiography* 22.1 (Jan. 2009), pp. 1–23. DOI: 10.1016/j.echo.2008.11.029.

[Bau+10] H. Baumgartner et al. “ESC Guidelines for the Management of Grown-up Congenital Heart Disease (New Version 2010) The Task Force on the Management of Grown-up Congenital Heart Disease of the European Society of Cardiology (ESC)”. In: *European heart journal* 31.23 (2010), pp. 2915–2957.

[Bau+99] H. Baumgartner et al. ““Overestimation” of Catheter Gradients by Doppler Ultrasound in Patients with Aortic Stenosis: A Predictable Manifestation of Pressure Recovery”. In: *Journal of the American College of Cardiology* 33.6 (1999), pp. 1655–1661.

[Baz+07] Y. Bazilevs et al. “Variational Multiscale Residual-Based Turbulence Modeling for Large Eddy Simulation of Incompressible Flows”. In: *Computer Methods in Applied Mechanics and Engineering* 197.1 (2007), pp. 173–201.

[BC14] C. Bertoglio and A. Caiazzo. “A Tangential Regularization Method for Backflow Stabilization in Hemodynamics”. In: *Journal of Computational Physics* 261 (2014), pp. 162–171.

[BC16] C. Bertoglio and A. Caiazzo. “A Stokes-Residual Backflow Stabilization Method Applied to Physiological Flows”. In: *Journal of Computational Physics* 313 (May 15, 2016), pp. 260–278. DOI: 10.1016/j.jcp.2016.02.045.

[BCF13] C. Bertoglio, A. Caiazzo, and M. A. Fernández. “Fractional-Step Schemes for the Coupling of Distributed and Lumped Models in Hemodynamics”. In: *SIAM Journal on Scientific Computing* 35.3 (2013), B551–B575.

[Bèg+87] C. Bègue et al. “Going Back to Stokes and Navier–Stokes Equations with Boundary-Conditions on the Pressure”. In: *C. R. Acad. Sci. Paris Ś er. I Math.* 304.1 (1987), pp. 23–28.

[Ber+13] C. Bertoglio et al. “State Observers of a Vascular Fluid–Structure Interaction Model through Measurements in the Solid”. In: *Computer Methods in Applied Mechanics and Engineering* 256 (2013), pp. 149–168.

[Ber+14] C. Bertoglio et al. “Identification of Artery Wall Stiffness: In Vitro Validation and in Vivo Results of a Data Assimilation Procedure Applied to a 3D Fluid–Structure Interaction Model”. In: *Journal of biomechanics* 47.5 (2014), pp. 1027–1034.

[Ber+17] C. Bertoglio et al. “Benchmark Problems for Numerical Treatment of Backflow at Open Boundaries”. In: *International Journal for Numerical Methods in Biomedical Engineering* 34.2 (July 25, 2017), e2918. DOI: 10.1002/cnm.2918.

[Ber+18a] C. Bertoglio et al. “Benchmark Problems for Numerical Treatment of Backflow at Open Boundaries”. In: *International journal for numerical methods in biomedical engineering* 34.2 (2018), e2918.

[Ber+18b] C. Bertoglio et al. “Relative Pressure Estimation from Velocity Measurements in Blood Flows: State-of-the-Art and New Approaches”. In: *International Journal for Numerical Methods in Biomedical Engineering* 34.2 (Feb. 2018), e2925. DOI: 10.1002/cnm.2925.

[Ber+19] C. Bertoglio et al. “Junction of Models of Different Dimension for Flows in Tube Structures by Womersley-Type Interface Conditions”. In: *SIAM Journal on Applied Mathematics* 79.3 (Jan. 2019), pp. 959–985. DOI: 10.1137/18M1229572.

[Ber12] C. Bertoglio. “Forward and Inverse Problems in Fluid-Structure Interaction. Application to Hemodynamics”. PhD thesis. Université Pierre et Marie Curie - Paris VI, Nov. 23, 2012.

[BFU07] P. Blanco, R. Feijóo, and S. Urquiza. “A Unified Variational Approach for Coupling 3D–1D Models and Its Blood Flow Applications”. In: *Computer Methods in Applied Mechanics and Engineering* 196.41-44 (Sept. 2007), pp. 4391–4410. DOI: 10.1016/j.cma.2007.05.008.

[Bir87] R. B. Bird, ed. *Dynamics of Polymeric Liquids*. 2nd ed. New York: Wiley, 1987. 2 pp.

[Bla+09] P. Blanco et al. “On the Potentialities of 3D–1D Coupled Models in Hemodynamics Simulations”. In: *Journal of Biomechanics* 42.7 (May 2009), pp. 919–930. DOI: 10.1016/j.jbiomech.2009.01.034.

[Bla+99] F. Blanc et al. “Asymptotic Analysis and Partial Asymptotic Decomposition of Domain for Stokes Equation in Tube Structure”. In: *Mathematical Models and Methods in Applied Sciences* 9.09 (1999), pp. 1351–1378.

[BM03] O. K. Baskurt and H. J. Meiselman. “Blood Rheology and Hemodynamics”. In: *Seminars in Thrombosis and Hemostasis* 29.5 (Oct. 2003), pp. 435–450. DOI: 10.1055/s-2003-44551.

[BMG12] C. Bertoglio, P. Moireau, and J.-F. Gerbeau. “Sequential Parameter Estimation for Fluid–Structure Problems: Application to Hemodynamics”. In: *International Journal for Numerical Methods in Biomedical Engineering* 28.4 (2012), pp. 434–455.

[Boc+10] J. Bock et al. "4D Phase Contrast MRI at 3 T: Effect of Standard and Blood-Pool Contrast Agents on SNR, PC-MRA, and Blood Flow Visualization". In: *Magnetic Resonance in Medicine: An Official Journal of the International Society for Magnetic Resonance in Medicine* 63.2 (2010), pp. 330–338.

[Boz+17] S. Bozzi et al. "Uncertainty Propagation of Phase Contrast-MRI Derived Inlet Boundary Conditions in Computational Hemodynamics Models of Thoracic Aorta". In: *Computer Methods in Biomechanics and Biomedical Engineering* 20.10 (July 27, 2017), pp. 1104–1112. DOI: 10.1080/10255842.2017.1334770.

[Bro+14] R. W. Brown et al. *Magnetic Resonance Imaging: Physical Principles and Sequence Design*. Second edition. Hoboken, New Jersey: John Wiley & Sons, Inc, 2014. 944 pp.

[Cai+10] A. Caiazzo et al. *Projection Schemes for Fluid Flows through a Porous Interface*. Research Report 7725. INRIA, 2010.

[Cai+17] A. Caiazzo et al. "Assessment of Reduced-Order Unscented Kalman Filter for Parameter Identification in 1-Dimensional Blood Flow Models Using Experimental Data". In: *International journal for numerical methods in biomedical engineering* 33.8 (2017), e2843.

[Cal+16] F. Callaghan et al. "Use of multi-velocity encoding 4D flow MRI to improve quantification of flow patterns in the aorta". In: *Journal of Magnetic Resonance Imaging* 43.2 (2016), pp. 352–363.

[Cam+12] I. C. Campbell et al. "Effect of Inlet Velocity Profiles on Patient-Specific Computational Fluid Dynamics Simulations of the Carotid Bifurcation". In: *Journal of biomechanical engineering* 134.5 (2012), p. 051001.

[Car+18] H. Carrillo et al. "Optimal Dual-VENC (ODV) Unwrapping in Phase-Contrast MRI". In: *IEEE transactions on medical imaging* (2018).

[Cas+16] B. Casas et al. "4D Flow MRI-Based Pressure Loss Estimation in Stenotic Flows: Evaluation Using Numerical Simulations". In: *Magnetic resonance in medicine* 75.4 (2016), pp. 1808–1821.

[Cio+11] G. Cioffi et al. "Prognostic Effect of Inappropriately High Left Ventricular Mass in Asymptomatic Severe Aortic Stenosis". In: *Heart* 97.4 (2011), pp. 301–307.

[CK91] Y. I. Cho and K. R. Kensey. "Effects of the Non-Newtonian Viscosity of Blood on Flows in a Diseased Arterial Vessel. Part 1: Steady Flows". In: *Biorheology* 28.3-4 (June 1, 1991), pp. 241–262. DOI: 10.3233/BIR-1991-283-415.

[CN86] M. E. Cayco and R. A. Nicolaides. "Finite Element Technique for Optimal Pressure Recovery from Stream Function Formulation of Viscous Flows". In: *Mathematics of computation* 46.174 (1986), pp. 371–377.

[DeV+08] K. DeVault et al. "Blood Flow in the Circle of Willis: Modeling and Calibration". In: *Multiscale Modeling & Simulation* 7.2 (2008), pp. 888–909.

[Don+15] F. Donati et al. "Non-Invasive Pressure Difference Estimation from PC-MRI Using the Work-Energy Equation". In: *Medical image analysis* 26.1 (2015), pp. 159–172.

[Don+17] F. Donati et al. "Beyond Bernoulli: Improving the Accuracy and Precision of Noninvasive Estimation of Peak Pressure Drops". In: *Circulation: Cardiovascular Imaging* 10.1 (Jan. 2017). DOI: 10.1161/CIRCIMAGING.116.005207.

[DPV12] M. D'Elia, M. Perego, and A. Veneziani. "A Variational Data Assimilation Procedure for the Incompressible Navier-Stokes Equations in Hemodynamics". In: *Journal of Scientific Computing* 52.2 (Aug. 2012), pp. 340–359. DOI: 10.1007/s10915-011-9547-6.

[Dyv+06] P. Dyverfeldt et al. "Quantification of Intravoxel Velocity Standard Deviation and Turbulence Intensity by Generalizing Phase-Contrast MRI". In: *Magnetic Resonance in Medicine* 56.4 (Oct. 1, 2006), pp. 850–858. DOI: 10.1002/mrm.21022.

[Dyv+13] P. Dyverfeldt et al. "Magnetic Resonance Measurement of Turbulent Kinetic Energy for the Estimation of Irreversible Pressure Loss in Aortic Stenosis". In: *JACC: Cardiovascular Imaging* 6.1 (2013), pp. 64–71.

[Dyv+15] P. Dyverfeldt et al. "4D Flow Cardiovascular Magnetic Resonance Consensus Statement". In: *Journal of Cardiovascular Magnetic Resonance* 17.1 (Dec. 2015). DOI: 10.1186/s12968-015-0174-5.

[Ebb+02] T. Ebbers et al. "Noninvasive Measurement of Time-Varying Three-Dimensional Relative Pressure Fields within the Human Heart". In: *Journal of biomechanical engineering* 124.3 (2002), pp. 288–293.

[EF09] T. Ebbers and G. Farnebäck. "Improving Computation of Cardiovascular Relative Pressure Fields from Velocity MRI". In: *Journal of Magnetic Resonance Imaging* 30.1 (2009), pp. 54–61.

[Erb+14] R. Erbel et al. "2014 ESC Guidelines on the Diagnosis and Treatment of Aortic Diseases: Document Covering Acute and Chronic Aortic Diseases of the Thoracic and Abdominal Aorta of the Adult. The Task Force for the Diagnosis and Treatment of Aortic Diseases of the European Society of Cardiology (ESC)". In: *European heart journal* 35.41 (2014), pp. 2873–2926.

[Eve09] G. Evensen. *Data Assimilation: The Ensemble Kalman Filter*. Springer Science & Business Media, Aug. 17, 2009. 314 pp.

[FGG07] M. A. Fernández, J.-F. Gerbeau, and C. Grandmont. "A Projection Semi-Implicit Scheme for the Coupling of an Elastic Structure with an Incompressible Fluid". In: *International Journal for Numerical Methods in Engineering* 69.4 (2007), pp. 794–821.

[Fig+06] C. A. Figueroa et al. "A Coupled Momentum Method for Modeling Blood Flow in Three-Dimensional Deformable Arteries". In: *Computer Methods in Applied Mechanics and Engineering* 195.41-43 (Aug. 2006), pp. 5685–5706. DOI: 10.1016/j.cma.2005.11.011.

[FL03] M. Á. Fernández and P. Le Tallec. "Linear Stability Analysis in Fluid–Structure Interaction with Transpiration. Part I: Formulation and Mathematical Analysis". In: *Computer Methods in Applied Mechanics and Engineering* 192.43 (Oct. 2003), pp. 4805–4835. DOI: 10.1016/j.cma.2003.07.001.

[For+02] L. Formaggia et al. "Numerical Treatment of Defective Boundary Conditions for the Navier–Stokes Equations". In: *SIAM Journal on Numerical Analysis* 40.1 (2002), pp. 376–401.

[For+06] L. Formaggia et al. "Numerical Modeling of 1D Arterial Networks Coupled with a Lumped Parameters Description of the Heart". In: *Computer methods in biomechanics and biomedical engineering* 9.5 (2006), pp. 273–288.

[FQV09a] L. Formaggia, A. Quarteroni, and A. Veneziani, eds. *Cardiovascular Mathematics*. Milano: Springer Milan, 2009. DOI: 10.1007/978-88-470-1152-6.

[FQV09b] L. Formaggia, A. Quarteroni, and A. Veneziani. "Multiscale Models of the Vascular System". In: *Cardiovascular Mathematics: Modeling and Simulation of the Circulatory System*. Ed. by L. Formaggia, A. Quarteroni, and A. Veneziani. MS&A. Milano: Springer Milan, 2009, pp. 395–446. DOI: 10.1007/978-88-470-1152-6_11.

[Fry+12] A. Frydrychowicz et al. "Interdependencies of Aortic Arch Secondary Flow Patterns, Geometry, and Age Analysed by 4-Dimensional Phase Contrast Magnetic Resonance Imaging at 3 Tesla". In: *European radiology* 22.5 (2012), pp. 1122–1130.

[Fun+08] K. Funamoto et al. "Numerical Experiment for Ultrasonic-Measurement-Integrated Simulation of Three-Dimensional Unsteady Blood Flow". In: *Annals of biomedical engineering* 36.8 (2008), p. 1383.

[Fun+19] S. W. Funke et al. "Variational Data Assimilation for Transient Blood Flow Simulations: Cerebral Aneurysms as an Illustrative Example". In: *International journal for numerical methods in biomedical engineering* 35.1 (2019), e3152.

[FVV08] L. Formaggia, A. Veneziani, and C. Vergara. "A New Approach to Numerical Solution of Defective Boundary Value Problems in Incompressible Fluid Dynamics". In: *SIAM Journal on Numerical Analysis* 46.6 (2008), pp. 2769–2794.

[Gal+12] D. Gallo et al. "On the Use of in Vivo Measured Flow Rates as Boundary Conditions for Image-Based Hemodynamic Models of the Human Aorta: Implications for Indicators of Abnormal Flow". In: *Annals of biomedical engineering* 40.3 (2012), pp. 729–741.

[Gam+08] A. M. Gambaruto et al. "Reconstruction of Shape and Its Effect on Flow in Arterial Conduits". In: *International Journal for Numerical Methods in Fluids* 57.5 (2008), pp. 495–517.

[Gam+11] A. M. Gambaruto et al. "Sensitivity of Hemodynamics in a Patient Specific Cerebral Aneurysm to Vascular Geometry and Blood Rheology." In: *Mathematical biosciences and engineering : MBE* 8.2 (Apr. 2011), pp. 409–423. DOI: 10.3934/mbe.2011.8.409.

[Gar+03] D. Garcia et al. "Discrepancies between Catheter and Doppler Estimates of Valve Effective Orifice Area Can Be Predicted from the Pressure Recovery Phenomenon: Practical Implications with Regard to Quantification of Aortic Stenosis Severity". In: *Journal of the American College of Cardiology* 41.3 (2003), pp. 435–442.

[GBD16] GBD 2015 Mortality and Causes of Death Collaborators. *Global, Regional, and National Life Expectancy, All-Cause Mortality, and Cause-Specific Mortality for 249 Causes of Death, 1980-2015: A Systematic Analysis for the Global Burden of Disease Study 2015*. Oct. 8, 2016, pp. 1459–1544.

[GK08] L. Grinberg and G. E. Karniadakis. "Outflow Boundary Conditions for Arterial Networks with Multiple Outlets". In: *Annals of biomedical engineering* 36.9 (2008), pp. 1496–1514.

[GMS06] J. Guermond, P. Minev, and J. Shen. "An Overview of Projection Methods for Incompressible Flows". In: *Computer Methods in Applied Mechanics and Engineering* 195.44-47 (Sept. 2006), pp. 6011–6045. DOI: 10.1016/j.cma.2005.10.010.

[Gou+13] L. Goubergrits et al. “The Impact of MRI-Based Inflow for the Hemodynamic Evaluation of Aortic Coarctation”. In: *Annals of Biomedical Engineering* 41.12 (Dec. 1, 2013), pp. 2575–2587. DOI: 10.1007/s10439-013-0879-2.

[Gou+19] L. Goubergrits et al. “Patient-Specific Requirements and Clinical Validation of MRI-Based Pressure Mapping: A Two-Center Study in Patients with Aortic Coarctation”. In: *Journal of Magnetic Resonance Imaging* 49.1 (2019), pp. 81–89. DOI: 10.1002/jmri.26230.

[GR09] C. Geuzaine and J.-F. Remacle. “Gmsh: A 3-D Finite Element Mesh Generator with Built-in Pre-and Post-Processing Facilities”. In: *International journal for numerical methods in engineering* 79.11 (2009), pp. 1309–1331.

[Gue+18] T. Guerra et al. “A Data Assimilation Approach for Non-Newtonian Blood Flow Simulations in 3D Geometries”. In: *Applied Mathematics and Computation* 321 (Mar. 2018), pp. 176–194. DOI: 10.1016/j.amc.2017.10.029.

[GvdVJ99] F. Gijsen, F. van de Vosse, and J. Janssen. “The Influence of the Non-Newtonian Properties of Blood on the Flow in Large Arteries: Steady Flow in a Carotid Bifurcation Model”. In: *Journal of Biomechanics* 32.6 (June 1999), pp. 601–608. DOI: 10.1016/S0021-9290(99)00015-9.

[Ha+16a] H. Ha et al. “Multi-VENC acquisition of four-dimensional phase-contrast MRI to improve precision of velocity field measurement”. In: *Magnetic resonance in medicine* 75.5 (2016), pp. 1909–1919.

[Ha+16b] H. Ha et al. “Turbulent Kinetic Energy Measurement Using Phase Contrast MRI for Estimating the Post-Stenotic Pressure Drop: In Vitro Validation and Clinical Application”. In: *PLOS ONE* 11.3 (Mar. 15, 2016), e0151540. DOI: 10.1371/journal.pone.0151540.

[Ha+19] H. Ha et al. “Validation of Pressure Drop Assessment Using 4D Flow MRI-based Turbulence Production in Various Shapes of Aortic Stenoses”. In: *Magnetic Resonance in Medicine* 81.2 (Feb. 2019), pp. 893–906. DOI: 10.1002/mrm.27437.

[Har+13] D. Hardman et al. “Comparison of Patient-Specific Inlet Boundary Conditions in the Numerical Modelling of Blood Flow in Abdominal Aortic Aneurysm Disease”. In: *International Journal for Numerical Methods in Biomedical Engineering* 29.2 (2013), pp. 165–178.

[HC89] K. C. Hall and E. F. Crawley. “Calculation of Unsteady Flows in Turbomachinery Using the linearizedEuler Equations”. In: *AIAA Journal* 27.6 (June 1989), pp. 777–787. DOI: 10.2514/3.10178.

[Hey+10] J. J. Heys et al. “Weighted Least-Squares Finite Elements Based on Particle Imaging Velocimetry Data”. In: *Journal of Computational Physics* 229.1 (2010), pp. 107–118.

[Hir+10] L. F. Hiratzka et al. “2010 ACCF/AHA/AATS/ACR/ASA/SCA/SCAI/SIR/ STS/SVM Guidelines for the Diagnosis and Management of Patients with Thoracic Aortic Disease”. In: *Journal of the American College of Cardiology* 55.14 (2010), e27–e129.

[HL73] T. J. Hughes and J. Lubliner. “On the One-Dimensional Theory of Blood Flow in the Larger Vessels”. In: *Mathematical Biosciences* 18.1-2 (1973), pp. 161–170.

[Hop+07] T. A. Hope et al. "Comparison of Flow Patterns in Ascending Aortic Aneurysms and Volunteers Using Four-Dimensional Magnetic Resonance Velocity Mapping". In: *Journal of Magnetic Resonance Imaging* 26.6 (2007), pp. 1471–1479.

[HOR08] J. J. Hom, K. Ordovas, and G. P. Reddy. "Velocity-Encoded Cine MR Imaging in Aortic Coarctation: Functional Assessment of Hemodynamic Events". In: *Radiographics* 28.2 (2008), pp. 407–416.

[IGW12] M. Ismail, M. W. Gee, and W. A. Wall. "CFD Challenge: Hemodynamic Simulation of a Patient-Specific Aortic Coarctation Model with Adjoint-Based Calibrated Windkessel Elements". In: *International Workshop on Statistical Atlases and Computational Models of the Heart*. Springer, 2012, pp. 44–52.

[IWG13] M. Ismail, W. A. Wall, and M. W. Gee. "Adjoint-Based Inverse Analysis of Windkessel Parameters for Patient-Specific Vascular Models". In: *Journal of Computational Physics* 244 (2013), pp. 113–130.

[JL06] V. John and A. Liakos. "Time-Dependent Flow across a Step: The Slip with Friction Boundary Condition". In: *International journal for numerical methods in fluids* 50.6 (2006), pp. 713–731.

[Joh+04] B. M. Johnston et al. "Non-Newtonian Blood Flow in Human Right Coronary Arteries: Steady State Simulations". In: *Journal of Biomechanics* 37.5 (May 2004), pp. 709–720. DOI: 10.1016/j.jbiomech.2003.09.016.

[Joh02] V. John. "Slip with Friction and Penetration with Resistance Boundary Conditions for the Navier–Stokes Equations—Numerical Tests and Aspects of the Implementation". In: *Journal of Computational and Applied Mathematics* 147.2 (2002), pp. 287–300. DOI: 10.1016/S0377-0427(02)00437-5.

[JU97] S. J. Julier and J. K. Uhlmann. "New Extension of the Kalman Filter to Nonlinear Systems". In: *Signal Processing, Sensor Fusion, and Target Recognition VI*. Vol. 3068. International Society for Optics and Photonics, 1997, pp. 182–194.

[JW99] N. P. Jenkins and C. Ward. "Coarctation of the Aorta: Natural History and Outcome after Surgical Treatment". In: *Qjm* 92.7 (1999), pp. 365–371.

[Kal03] E. Kalnay. *Atmospheric Modeling, Data Assimilation and Predictability*. Cambridge university press, 2003.

[KB18] T. S. Koltukluoğlu and P. J. Blanco. "Boundary Control in Computational Haemodynamics". In: *Journal of Fluid Mechanics* 847 (July 2018), pp. 329–364. DOI: 10.1017/jfm.2018.329.

[Kil+93] P. J. Kilner et al. "Helical and Retrograde Secondary Flow Patterns in the Aortic Arch Studied by Three-Directional Magnetic Resonance Velocity Mapping." In: *Circulation* 88.5 (1993), pp. 2235–2247.

[Kil11] P. J. Kilner. "Imaging Congenital Heart Disease in Adults". In: *The British Journal of Radiology* 84 (special_issue_3 Dec. 2011), S258–S268. DOI: 10.1259/bjr/74240815.

[Kim+10] H. J. Kim et al. "Patient-Specific Modeling of Blood Flow and Pressure in Human Coronary Arteries". In: *Annals of Biomedical Engineering* 38.10 (Oct. 1, 2010), pp. 3195–3209. DOI: 10.1007/s10439-010-0083-6.

[Kri+12] S. B. S. Krittian et al. "A Finite-Element Approach to the Direct Computation of Relative Cardiovascular Pressure from Time-Resolved MR Velocity Data". In: *Medical Image Analysis* 16.5 (July 2012), pp. 1029–1037. DOI: 10.1016/j.media.2012.04.003.

[Ku97] D. N. Ku. "Blood Flow in Arteries". In: *Annual review of fluid mechanics* 29.1 (1997), pp. 399–434.

[Kun+13] E. Kung et al. "Predictive Modeling of the Virtual Hemi-Fontan Operation for Second Stage Single Ventricle Palliation: Two Patient-Specific Cases". In: *Journal of Biomechanics*. Special Issue: Biofluid Mechanics 46.2 (Jan. 18, 2013), pp. 423–429. DOI: 10.1016/j.jbiomech.2012.10.023.

[Lad69] O. Ladijzenskaia. "The Mathematical Theory of Viscous Incompressible Fluid". In: *Gordon and Breach, New York* (1969).

[LM16] A. Linke and C. Merdon. "Pressure-Robustness and Discrete Helmholtz Projectors in Mixed Finite Element Methods for the Incompressible Navier–Stokes Equations". In: *Computer Methods in Applied Mechanics and Engineering* 311 (Nov. 1, 2016), pp. 304–326. DOI: 10.1016/j.cma.2016.08.018.

[LMN17] R. Lal, B. Mohammadi, and F. Nicoud. "Data Assimilation for Identification of Cardiovascular Network Characteristics". In: *International journal for numerical methods in biomedical engineering* 33.5 (2017), e2824.

[Lom14] D. Lombardi. "Inverse Problems in 1D Hemodynamics on Systemic Networks: A Sequential Approach". In: *International journal for numerical methods in biomedical engineering* 30.2 (2014), pp. 160–179.

[LPP95] A. Lee, B. Pike, and N. Pelc. "Three-Point Phase-Contrast Velocity Measurements with Increased Velocity-to-Noise Ratio". In: *Magnetic Resonance in Medicine* 33 (1995), pp. 122–128.

[Mar+12] M. Markl et al. "4D Flow MRI". In: *Journal of Magnetic Resonance Imaging* 36.5 (2012), pp. 1015–1036.

[Mar+19] D. Marlevi et al. "Estimation of Cardiovascular Relative Pressure Using Virtual Work-Energy". In: *Scientific Reports* 9.1 (Dec. 2019). DOI: 10.1038/s41598-018-37714-0.

[MC11] P. Moireau and D. Chapelle. "Reduced-Order Unscented Kalman Filtering with Application to Parameter Identification in Large-Dimensional Systems". In: *ESAIM: Control, Optimisation and Calculus of Variations* 17.2 (2011), pp. 380–405.

[MCB18] L. O. Müller, A. Caiazzo, and P. J. Blanco. "Reduced-Order Unscented Kalman Filter with Observations in the Frequency Domain: Application to Computational Hemodynamics". In: *IEEE Transactions on Biomedical Engineering* (2018).

[Mei+10] S. Meier et al. "Non-Invasive 4D Blood Flow and Pressure Quantification in Central Blood Vessels via PC-MRI". In: *Computing in Cardiology, 2010*. IEEE, 2010, pp. 903–906.

[MMG08] H. C. McGill, C. A. McMahan, and S. S. Gidding. "Preventing Heart Disease in the 21st Century: Implications of the Pathobiological Determinants of Atherosclerosis in Youth (PDAY) Study". In: *Circulation* 117.9 (Mar. 4, 2008), pp. 1216–1227. DOI: 10.1161/CIRCULATIONAHA.107.717033.

[Moi+13] P. Moireau et al. “Sequential Identification of Boundary Support Parameters in a Fluid-Structure Vascular Model Using Patient Image Data”. In: *Biomechanics and Modeling in Mechanobiology* 12.3 (June 2013), pp. 475–496. DOI: 10.1007/s10237-012-0418-3.

[Mon+18] C. Montalba et al. “Variability of 4D Flow Parameters When Subjected to Changes in MRI Acquisition Parameters Using a Realistic Thoracic Aortic Phantom”. In: *Magnetic resonance in medicine* 79.4 (2018), pp. 1882–1892.

[Moo+99] J. A. Moore et al. “Accuracy of Computational Hemodynamics in Complex Arterial Geometries Reconstructed from Magnetic Resonance Imaging”. In: *Annals of Biomedical Engineering* 27.1 (Jan. 1, 1999), pp. 32–41. DOI: 10.1114/1.163.

[Mor+10] U. Morbiducci et al. “Outflow Conditions for Image-Based Hemodynamic Models of the Carotid Bifurcation: Implications for Indicators of Abnormal Flow”. In: *Journal of Biomechanical Engineering* 132.9 (Aug. 17, 2010), pp. 091005-091005–11. DOI: 10.1115/1.4001886.

[Mor+13] U. Morbiducci et al. “Inflow Boundary Conditions for Image-Based Computational Hemodynamics: Impact of Idealized versus Measured Velocity Profiles in the Human Aorta”. In: *Journal of biomechanics* 46.1 (2013), pp. 102–109.

[Mor00] G. D. Mortchéléwicz. “Flutter Simulations”. In: *Aerospace Science and Technology* 4.1 (Jan. 2000), pp. 33–40. DOI: 10.1016/S1270-9638(00)00116-4.

[MR19] P. Minakowski and T. Richter. “Finite Element Error Estimates under Geometric Uncertainty”. In: *arXiv e-prints*, arXiv:1902.07532 (Feb. 2019), arXiv:1902.07532.

[MSE97] J. A. Moore, D. A. Steinman, and C. R. Ethier. “Computational Blood Flow Modelling: Errors Associated with Reconstructing Finite Element Models from Magnetic Resonance Images”. In: *Journal of Biomechanics* 31.2 (1997), pp. 179–184.

[Nas+04] A. Nasiraei-Moghaddam et al. “Factors Affecting the Accuracy of Pressure Measurements in Vascular Stenoses from Phase-Contrast MRI”. In: *Magnetic Resonance in Medicine: An Official Journal of the International Society for Magnetic Resonance in Medicine* 52.2 (2004), pp. 300–309.

[NB19] D. Nolte and C. Bertoglio. “Reducing the Impact of Geometric Errors in Flow Computations Using Velocity Measurements”. In: *International Journal for Numerical Methods in Biomedical Engineering* (2019), e3203. DOI: 10.1002/cnm.3203.

[Net+12] E. Nett et al. “Four-dimensional phase contrast MRI with accelerated dual velocity encoding”. In: *Journal of Magnetic Resonance Imaging* 35.6 (2012), pp. 1462–1471.

[Nol+19] D. Nolte et al. “Validation of 4D-Flow-Based Pressure Map Estimators”. In: *Journal of Magnetic Resonance Imaging* (submitted 2019).

[NOV11] W. Nichols, M. O’Rourke, and C. Vlachopoulos. *McDonald’s Blood Flow in Arteries: Theoretical, Experimental and Clinical Principles*. 6th ed. London: CRC Press, 2011.

[Omr+03] H. Omran et al. “Silent and Apparent Cerebral Embolism after Retrograde Catheterisation of the Aortic Valve in Valvular Stenosis: A Prospective, Randomised Study”. In: *The Lancet* 361.9365 (2003), pp. 1241–1246.

[Pan+14] S. Pant et al. "A Methodological Paradigm for Patient-Specific Multi-Scale CFD Simulations: From Clinical Measurements to Parameter Estimates for Individual Analysis: PATIENT-SPECIFIC PARAMETER ESTIMATION FOR MULTI-SCALE CFD SIMULATIONS". In: *International Journal for Numerical Methods in Biomedical Engineering* 30.12 (Dec. 2014), pp. 1614–1648. DOI: 10.1002/cnm.2692.

[Pan05] G. P. Panasenko. *Multi-Scale Modelling for Structures and Composites*. Vol. 615. Springer, Dodrecht, 2005.

[Pan98a] G. Panasenko. "Method of Asymptotic Partial Decomposition of Domain". In: *Mathematical Models and Methods in Applied Sciences* 8.01 (1998), pp. 139–156.

[Pan98b] G. P. Panasenko. "Asymptotic Expansion of the Solution of Navier–Stokes Equation in a Tube Structure". In: *Comptes Rendus de l'Académie des Sciences-Series IIB-Mechanics-Physics-Astronomy* 326.12 (1998), pp. 867–872.

[Pan98c] G. P. Panasenko. "Partial Asymptotic Decomposition of Domain: Navier–Stokes Equation in Tube Structure". In: *Comptes Rendus de l'Académie des Sciences-Series IIB-Mechanics-Physics-Astronomy* 326.12 (1998), pp. 893–898.

[Pir+17] S. Pirola et al. "On the Choice of Outlet Boundary Conditions for Patient-Specific Analysis of Aortic Flow Using Computational Fluid Dynamics". In: *Journal of Biomechanics* 60 (2017), pp. 15–21.

[Pop00] S. B. Pope. *Turbulent Flows*. Cambridge ; New York: Cambridge University Press, 2000. 771 pp.

[PP15] G. Panasenko and K. Pileckas. "Asymptotic Analysis of the Non-Steady Navier–Stokes Equations in a Tube Structure. I. The Case without Bound-Ary-Layer-in-Time". In: *Nonlinear Analysis: Theory, Methods & Applications* 122 (2015), pp. 125–168.

[PV09] J. Peiró and A. Veneziani. "Reduced Models of the Cardiovascular System". In: *Cardiovascular Mathematics: Modeling and Simulation of the Circulatory System*. Ed. by L. Formaggia, A. Quarteroni, and A. Veneziani. MS&A. Milano: Springer Milan, 2009, pp. 347–394. DOI: 10.1007/978-88-470-1152-6_10.

[RE06] Y. Richter and E. R. Edelman. "Cardiology Is Flow". In: *Circulation* 113.23 (June 13, 2006), pp. 2679–2682. DOI: 10.1161/CIRCULATIONAHA.106.632687.

[Ren+14] F. Rengier et al. "Noninvasive Pressure Difference Mapping Derived from 4D Flow MRI in Patients with Unrepaired and Repaired Aortic Coarctation". In: *Cardiovascular diagnosis and therapy* 4.2 (2014), p. 97.

[Ren+15] F. Rengier et al. "Noninvasive 4D Pressure Difference Mapping Derived from 4D Flow MRI in Patients with Repaired Aortic Coarctation: Comparison with Young Healthy Volunteers". In: *The international journal of cardiovascular imaging* 31.4 (2015), pp. 823–830.

[Rie+14] E. Riesenkampff et al. "Pressure Fields by Flow-Sensitive, 4D, Velocity-Encoded CMR in Patients with Aortic Coarctation". In: *JACC: Cardiovascular Imaging* 7.9 (2014), pp. 920–926.

[Saa03] Y. Saad. *Iterative Methods for Sparse Linear Systems*. 2nd ed. Philadelphia: SIAM, 2003. 528 pp.

[San+16] S. Sankaran et al. "Uncertainty Quantification in Coronary Blood Flow Simulations: Impact of Geometry, Boundary Conditions and Blood Viscosity". In: *Journal of biomechanics* 49.12 (2016), pp. 2540–2547.

[SGT15a] S. Sankaran, L. Grady, and C. A. Taylor. "Fast Computation of Hemodynamic Sensitivity to Lumen Segmentation Uncertainty". In: *IEEE Transactions on Medical Imaging* 34.12 (Dec. 2015), pp. 2562–2571. DOI: 10.1109/TMI.2015.2445777.

[SGT15b] S. Sankaran, L. Grady, and C. A. Taylor. "Impact of Geometric Uncertainty on Hemodynamic Simulations Using Machine Learning". In: *Computer Methods in Applied Mechanics and Engineering* 297 (2015), pp. 167–190.

[SM11] S. Sankaran and A. L. Marsden. "A Stochastic Collocation Method for Uncertainty Quantification and Propagation in Cardiovascular Simulations". In: *Journal of biomechanical engineering* 133.3 (2011), p. 031001.

[Son+94] S. M. Song et al. "Determining Cardiac Velocity Fields and Intraventricular Pressure Distribution from a Sequence of Ultrafast CT Cardiac Images". In: *IEEE transactions on medical imaging* 13.2 (1994), pp. 386–397.

[Sot+16] J. Sotelo et al. "3D Quantification of Wall Shear Stress and Oscillatory Shear Index Using a Finite-Element Method in 3D CINE PC-MRI Data of the Thoracic Aorta". In: *IEEE transactions on medical imaging* 35.6 (2016), pp. 1475–1487.

[Sot+18] J. Sotelo et al. "Three-Dimensional Quantification of Vorticity and Helicity from 3D Cine PC-MRI Using Finite-Element Interpolations". In: *Magnetic resonance in medicine* 79.1 (2018), pp. 541–553.

[Švi+16] H. Švihlová et al. "Determination of Pressure Data from Velocity Data with a View toward Its Application in Cardiovascular Mechanics. Part 1. Theoretical Considerations". In: *International Journal of Engineering Science* (2016). DOI: 10.1016/j.ijengsci.2015.11.002.

[SY16] M. Sugihara-Seki and H. Yamada. "Fundamentals of Vascular Bio-Fluid and Solid Mechanics". In: *Vascular Engineering*. Tokyo: Springer, 2016, pp. 13–45.

[Tal97] O. Talagrand. "Assimilation of Observations, an Introduction (Gtspecial Issueltdata Assimilation in Meteology and Oceanography: Theory and Practice)". In: *Journal of the Meteorological Society of Japan. Ser. II* 75 (1B 1997), pp. 191–209.

[Tan+12] F. P. P. Tan et al. "Comparison of Aortic Flow Patterns Before and After Transcatheter Aortic Valve Implantation". In: *Cardiovascular Engineering and Technology* 3.1 (Mar. 1, 2012), pp. 123–135. DOI: 10.1007/s13239-011-0073-3.

[TD04] C. A. Taylor and M. T. Draney. "Experimental and Computational Methods in Cardiovascular Fluid Mechanics". In: *Annual Review of Fluid Mechanics* 36.1 (Jan. 2004), pp. 197–231. DOI: 10.1146/annurev.fluid.36.050802.121944.

[TGS17] J. Tiago, T. Guerra, and A. Sequeira. "A Velocity Tracking Approach for the Data Assimilation Problem in Blood Flow Simulations". In: *International Journal for Numerical Methods in Biomedical Engineering* 33.10 (2017), e2856. DOI: 10.1002/cnm.2856.

[TS10] C. A. Taylor and D. A. Steinman. "Image-Based Modeling of Blood Flow and Vessel Wall Dynamics: Applications, Methods and Future Directions". In: *Annals of biomedical engineering* 38.3 (2010), pp. 1188–1203.

[TT16] S. Tada and J. M. Tarbell. "Hemodynamics in Physio- and Pathological Vessels". In: *Vascular Engineering*. Tokyo: Springer, 2016, pp. 69–98.

[Tys+00] J. M. Tyszka et al. "Three-Dimensional, Time-Resolved (4D) Relative Pressure Mapping Using Magnetic Resonance Imaging". In: *Journal of Magnetic Resonance Imaging: An Official Journal of the International Society for Magnetic Resonance in Medicine* 12.2 (2000), pp. 321–329.

[UP94] S. N. Urchuk and D. B. Plewes. "MR Measurement of Pulsatile Pressure Gradients". In: *Journal of magnetic resonance imaging* 4.6 (1994), pp. 829–836.

[Urb+16] J. Urbina et al. "Realistic Aortic Phantom to Study Hemodynamics Using MRI and Cardiac Catheterization in Normal and Aortic Coarctation Conditions". In: *Journal of Magnetic Resonance Imaging* 44.3 (2016), pp. 683–697.

[Urq+06] S. A. Urquiza et al. "Multidimensional Modelling for the Carotid Artery Blood Flow". In: *Computer Methods in Applied Mechanics and Engineering* 195.33-36 (2006), pp. 4002–4017.

[Vig+10] I. E. Vignon-Clementel et al. "Outflow Boundary Conditions for 3D Simulations of Non-Periodic Blood Flow and Pressure Fields in Deformable Arteries". In: *Computer methods in biomechanics and biomedical engineering* 13.5 (2010), pp. 625–640.

[Vit+98] R. Vitiello et al. "Complications Associated with Pediatric Cardiac Catheterization". In: *Journal of the American College of Cardiology* 32.5 (1998), pp. 1433–1440.

[VV05] A. Veneziani and C. Vergara. "Flow Rate Defective Boundary Conditions in Haemodynamics Simulations". In: *International Journal for Numerical Methods in Fluids* 47.8-9 (2005), pp. 803–816.

[Wak+09] A. K. Wake et al. "Choice of In Vivo Versus Idealized Velocity Boundary Conditions Influences Physiologically Relevant Flow Patterns in a Subject-Specific Simulation of Flow in the Human Carotid Bifurcation". In: *Journal of Biomechanical Engineering* 131.2 (2009), p. 021013. DOI: 10.1115/1.3005157.

[WHO18] WHO. *Global Heath Estimates 2016: Deaths by Cause, Age, Sex, by Country and by Region, 2000–2016*. Geneva: World Health Organization, 2018.

[Wil+17] E. Wilkins et al. "European Cardiovascular Disease Statistics 2017". In: (2017).

[WLW09] N. Westerhof, J.-W. Lankhaar, and B. E. Westerhof. "The Arterial Windkessel". In: *Medical & biological engineering & computing* 47.2 (2009), pp. 131–141.

[Wym+88] R. M. Wyman et al. "Current Complications of Diagnostic and Therapeutic Cardiac Catheterization". In: *Journal of the American College of Cardiology* 12.6 (1988), pp. 1400–1406.

[Yan+96] G.-Z. Yang et al. "Computation of Flow Pressure Fields from Magnetic Resonance Velocity Mapping". In: *Magnetic resonance in medicine* 36.4 (1996), pp. 520–526.